Unterschrift des Betreuers

TECHNISCHE UNIVERSITÄT WIEN
Vienna University of Technology

DIPLOMARBEIT

Development of a Dark Lock-in thermography (DLIT) system and its application for characterizing thin film and crystalline photovoltaic generators

ausgeführt am Institut für
Angewandte Physik
der Technischen Universität Wien

unter der Anleitung von
Ao. Univ.-Prof. Dr. Martin Gröschl

in Kooperation mit dem
Austrian Institute of Technology
Energy Department, Photovoltaic Systems

unter der Betreuung von
Dipl. Ing. Bernhard Kubicek

durch

Martin HALWACHS BSc.
Soldanellenweg 55/11/2, 1220 Wien

December 12, 2014

Unterschrift (Student)

Danksagung

Zunächst möchte ich mich bedanken, dass mir das Austrian Institute of Technology (AIT), im Rahmen des Projektes SynerCIS, diese Diplomarbeit ermöglicht und das entsprechende Material zur Verfügung gestellt hat. Ich habe dabei sehr viel von der Betreuung durch Bernhard Kubicek profitiert, dessen Korrekturen und kritisches Denken mir zugleich Hilfe als auch Motivation waren. Weiters möchte ich nicht auf die anderen Kollegen am AIT vergessen, die mir stets geholfen haben, eine Antwort zu finden, wenn es um verzwickte Details ging und die auch oft zu ausgedehnten Diskussionen bereit waren. Zudem danke ich meinem Professor, Martin Gröschl, der die Kooperation mit dem AIT im Zuge dieser Diplomarbeit erst ermöglichte.

Da diese Arbeit meine letzte Lehrveranstaltung eines 5.5 jährigen Studiums ist, möchte ich an dieser Stelle auch für die Unterstützung meiner Mutter, Sonja Halwachs, meiner Oma Herlinde Nüssel und meiner Freundin Sabrina Simanov danken. Alle drei haben mir geholfen stressige Zeiten zu überwinden, mich zu motivieren und mir die Zeit gegeben, zu lernen und nachzuforschen. Außerdem danke ich meinen Studienkollegen, ohne die ein derartig schnelles Voranschreiten im Studium sehr viel mühsamer gewesen wäre und weit weniger Spaß gemacht hätte. Besonders das Erarbeiten von Übungsaufgaben und Prüfungsvorbereitungen in Lerngruppen war mir, im Nachhinein gesehen, eine große Freude.

Contents

Zusammenfassung

In der vorliegenden Arbeit wurde ein Messaufbau für Dunkel Lock-in Thermographie (DLIT) ausgehend von einer handelsüblichen mobilen Wärmebildkamera entwickelt, und eine entsprechende Auswertungssoftware programmiert. Photovoltaik-Module unterschiedlicher kristalliner und Dünnschicht-Technologien wurden vermessen, nicht nur um den Einfluss der Mess-Parameter zu untersuchen, sondern auch, um die durch DLIT nun zugänglichen Analysemöglichkeiten aufzuzeigen. Korrelationen sowie Unterschiede zu anderen bildgebenden Charakterisierungs-Verfahren werden diskutiert.

DLIT ist eine Weiterentwicklung der konventionellen Thermographie. Zeitreihen der Modul-Oberflächen-Temperaturen, die durch einen modulierten elektrischen Wärmeeintrag in den PV-Zellen eines Moduls entstehen, werden durch zeitliche Fourieranalyse demoduliert. Für jeden Bildpunkt resultiert die Amplitude und der Phasenversatz der Oberflächentemperatur-Schwankungen im Bezug zur elektrischen modulierten Heizleistung.

Die durch DLIT abgebildete Heizleistung von Kurzschlüssen in der Zellstruktur weist eine etwa um den Faktor zehn bessere örtliche Auflösung auf als Analysen mittels klassischer Thermographie. Durch die hohe Informationsmenge pro Bildpunkt und deren erwarteter zeitlicher Periodizität können Schwankungen festgestellt werden, deren Intensitäten kleiner als das Rauschen des Messsystems sind. Da die Temperatur-Diffusionslänge mit der Puls-Frequenz abnimmt, kann die örtliche Auflösung bei hohen zeitlichen Anregungs-Frequenzen verbessert werden. Dies führt jedoch zu einer Verringerung der Schwankungs-Amplitude, und damit zu einer Erhöhung des relativen Rauschens.

Verschiedene Modultechnologien (mono c-Si, poly c-Si, CdTe, a-Si, CIS) werden mittels DLIT, EL, und Thermographie verglichen. Die Ergebnisse zeigen, dass DLIT, speziell in Kombination mit Elektrolumineszenz, ein wertvolles Werkzeug in der Analyse von Photovoltaik-Modulen ist.

Abstract

In presented thesis a dark Lock-in thermography (DLIT) measurement system based on a typical hand held thermography camera was developed, together with according software for measurement evaluation. Photovoltaic (PV) modules of various crystalline and thin film technologies were measured, to not only deduce the influence of measurement parameters, but also to explore analytical possibilities. Correlation and deviations to common imaging methods are discussed.

DLIT is an improved thermography measurement. Time-series of the PV modules' surface temperature variations, caused by modulated electrical heating of PV cells, are Fourier-analyzed in time. This results in an amplitude and a phase for each pixel of the surface relative to the heating pulses.

DLIT images of PV modules show faults with a typical ten times better special resolution than conventional thermography. Due to the amount of temporal measurements per pixel and the expected periodicity, signals amplitudes can be found with intensities smaller than the noise of a single measurement. As the heat diffusion length decreases with the pulse-frequency, the spatial resolution improves with the excitation-frequency. However, the absolute amplitude of surface temperature waves decrease, hence leading to more relative noise intensity in the DLIT images.

Various PV module technologies (i.e. mono and poly c-Si, CdTe, a-Si, CIS) were analyzed using DLIT, EL, and conventional thermograph. The results show that DLIT is a very powerful tool to analyze defects in PV modules that is best paired with electroluminescence.

1 Introduction

Photovoltaics is a well established technology with ongoing development and a tremendous growth potential for the future. Further development needs sufficient characterization and quality insurance techniques to improve fabrication processes. Dark Lock-in thermography (DLIT) is an already known characterization process, which improves the resolution of classical thermography.

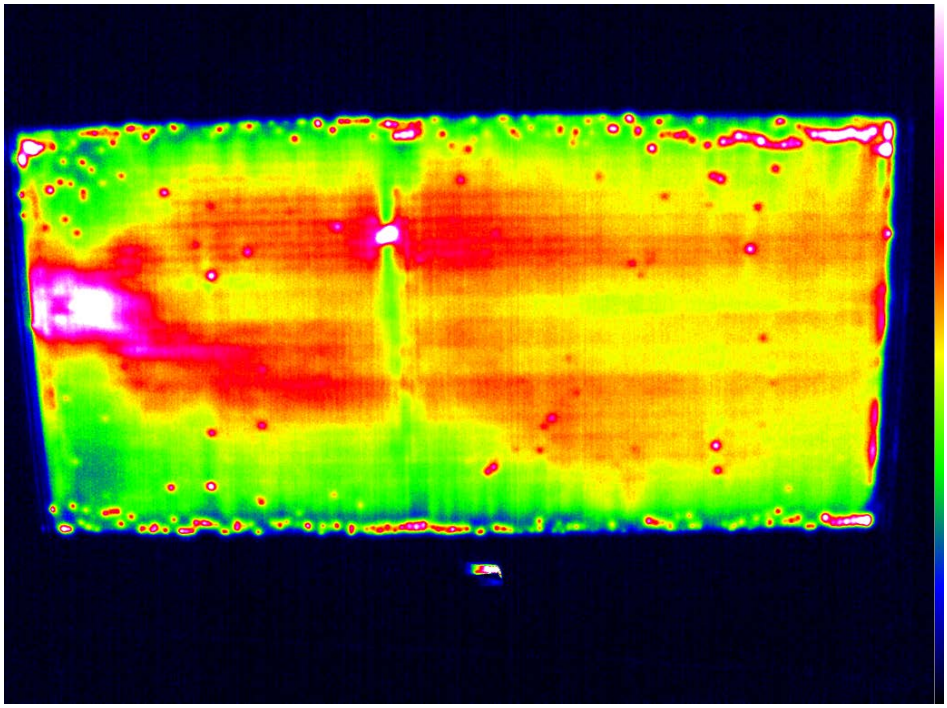

Fig. 1.1: Dark Lock-in thermography of a CdTe module showing many shunts on the border and inside.

DLIT uses the Lock-in principle to reduce statistical noise by modulating heat introduction to a photovoltaics (PV) module. The PV module will be connected to a power source and heated in pulses. Thereby, temperature variations will be introduce to the module, depending on the cell and module structure or possible faults in the structure. The results are shown in images similar to Fig. 1.1, which visualize the amplitude or phase of each surface spot.

This enables qualitative investigations of faults and may be additionally used with electroluminescence or photoluminescence measurements. A lot of studies investigate degradation of modules under various environmental impacts. A comparison of DLIT prior and after these studies may also help to identify differences.

As DLIT is an interesting field in PV characterization, this thesis aims to create an experimental setup at the Austrian Institute of Technology and an evaluation software.

Further, modules of different technologies are measured to analyse and test the system and show analysis results.

Section 1.1 will contain basic information on PV. The functional description in section 1.1.3 will then list processes taking place in a solar cell and how solar cells are described. The sections 1.1.4 and 1.1.5 will compare different module technologies and show the layout of solar cells and PV modules. Finally some typical characterisation methods are summarized in section 1.1.6.

As DLIT is an advanced characterization method based on classical thermography, theoretical background of thermography will be presented in section 2.1. That section contains first some repetitions on radiative heat transfer and the infrared spectrum. Section 2.1.2 and its following sections will explain camera sensor working principles and types, as well as typically used properties of thermocameras.

Next, the heat diffusion equation will be discussed in section 2.2. Therefore, certain terminology as thermal thickness and the diffusion length will be introduced. The behavior of different heat sources to periodical heating is shown in section 2.2.3. Last a brief summary of the processes inside the solar cell in this scenario are written in section 2.2.4.

The measurement technique of DLIT will be explained in section 2.3. First the Fourier analysis and measurement principle of Lock-in will be discussed in sections 2.3.1 and 2.3.2. The mathematical explanation of the DLIT is shown in section 2.3.3 and adapted to the measurement in section 2.3.4. As in this thesis a rectangular current pulse is used section 2.3.5 will outline the differences to using sinusoidal current. The expected error and noise from the measurement was derived and discussed in the sections 2.3.6 and 2.3.7. Finally the evaluation for different heat sources is summarized in section 2.3.8.

The measurement setup will be summarized in section 3.1 and the established software tool for evaluating the measurements is described in section 3.2. To test the setup and the evaluations DLIT measurements have been performed for various module technologies. Thereby some characteristics of the realized measurements were found and are shown in section 3.3. The carried out measurements of different module technologies are afterwards compared and summarized in section 3.4.

1.1 Photovoltaics

The field of photovoltaics (PV) started with the first solar cell at Bell Laboratories in 1954, having an efficiency of 6%. Though first solar cells were mainly for space applications, their advantages (direct energy conversion, no moving parts, no pollution, long life time, flexible adaption of output parameters to specific needs,...) lead to terrestrial energy generators too [21].

Crystalline silicon solar cells were easier to handle, as silicon technologies were already far developed, due to microelectronics. But the advantages of thin film technology (thinner layers, less material, direct band structure, stackable,...) lead to their development in parallel to crystalline silicon based cells. Nowadays there are various different technologies including concentrated solar cells and tandem cells and a lot of effort goes into development of highest possible efficiency, which is at the moment 44.9% for a multi-junction concentrator cell [16], [21], [47].

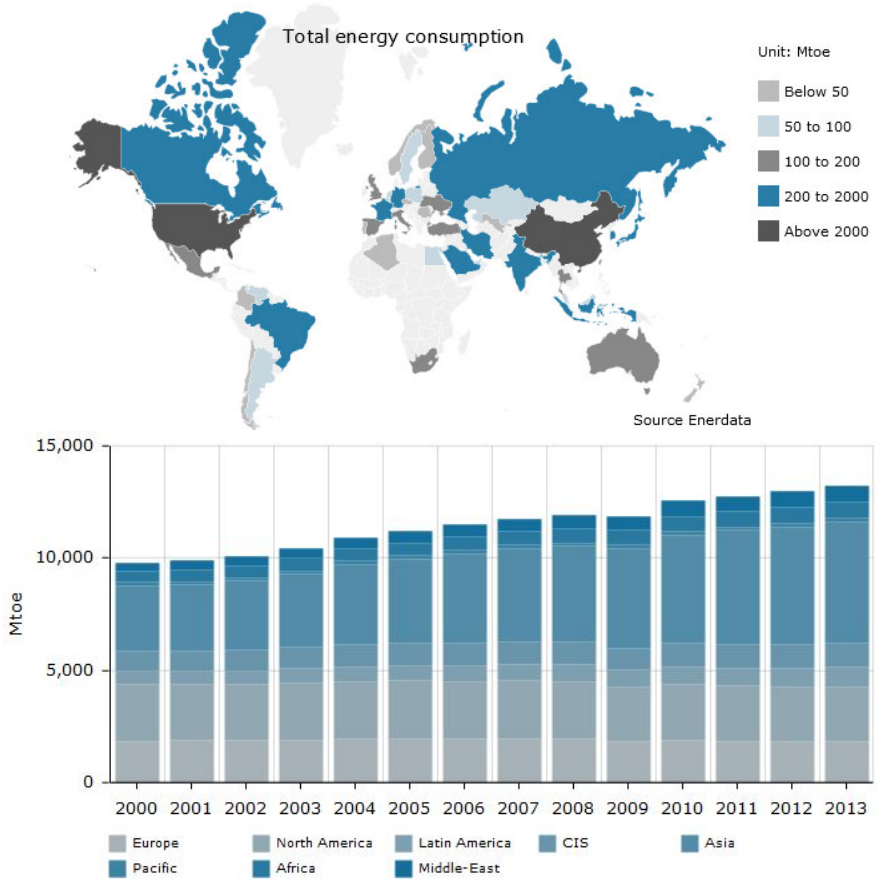

Fig. 1.2: On top the global energy consumption in 2013 is shown according to the regions of the world. It rose from 9797 Mtoe in 2000 to 13217 Mtoe, where Mtoe stands for Mega tons oil equivalent, and 1 Mtoe = 41.868 $\cdot 10^6$ MJ = 11.63 $\cdot 10^9$ kWh according to [43]. Clearly the energy demand of Asia increased most from 2929 Mtoe to 5439 Mtoe These graphs are taken from [13].

1.1.1 Why the world needs PV

The earth's atmosphere provides a natural green house effect, which allows an average temperature of 15 °C instead of -18 °C on earth. CO_2 is part of the atmosphere and its contribution to the green house effect is about 56%. The amount of CO_2 in the atmosphere rose from 280 ppmv to 389 ppmv in between 1850 and 2010, due to increasing industrialization and energy demands, relying on fossile primary energy. This lead to a human induced *anthropogenic* green house effect, which affects earth's climate (2/3 of alp glacier volume is gone, sea level rises about 1.8 mm per year, rising of the average temperature on earth by 0.7 °C per year). It is believed, that these effects extend in the next years, if - among others - CO_2 emission is not reduced. Therefore renewable energy generators, including PV, are an important opportunity to fulfill earth's growing energy demand and reduce CO_2 emissions in energy conversion [40].

The energy reaching earth surface from sun per year is about 1.08 $\cdot 10^{18}$ kWh [40] the world's global energy demand per year from 2000 to 2013 is shown in Fig. 1.2 with a map comparing energy consumption per country. Comparing sun's energy on earth's surface to the total global primary energy demand per year of 13217 Mtoe = 1.537

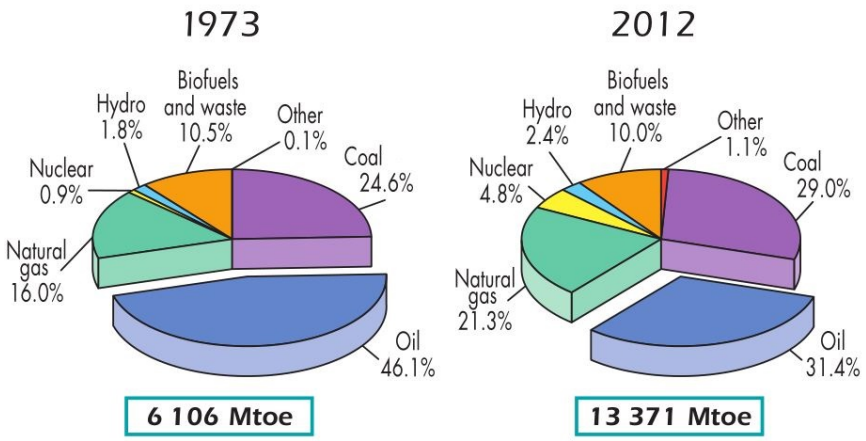

Fig. 1.3: The global energy supply is compared for 1973 and 2012 and split into primary energy sources. As PV is only among the Other 1.1% with other renewable energy sources, there is still a big potential for increase. More than 80% of world's primary energy comes from fossil fuels (coal, oil, natural gas). This graph is taken from [3].

$\cdot 10^{14}$ kWh from 2013, the sun's energy is about 7000 of the earth's energy demand. Therefore direct conversion of sun's energy to electrical energy by PV is an important opportunity for the future. Another one is wind energy. Which has the advantage of being available also at times, when PV generates less energy. Anyway it relies on wind, which is varies in intensity as well.

The global energy supply of 2012 is mostly provided by fossil fuels (coal, oil, gas) as shown in Fig. 1.3. These are limited resources on earth and their exploration and extraction will cost more money and will be more dangerous to find when reaching the limits. The same holds for uranium, needed for nuclear power generation. In comparison to PV energy conversion, the sun's energy is not limited in its availability or at least has a much later limit than fossil fuels. [40]

1.1.2 PV market in Austria

In 2013, PV modules with a power of 263.1 MWp were installed in Austria, mostly grid-connected.The installed power is growing since 2006 (see Fig. 1.4). At the end of 2013 there have been 626 MWp installed, covering 1.1% of Austria's energy demand. A graph of the distribution of different PV material technologies is shown in Fig. 1.5. Concering production of PV modules in Austria, in contrary to the reduction in 2012, 2013 showed a growth of 5.1% measured by the power sum of all produced modules. These had an overall power of 74.475 MWp [6].

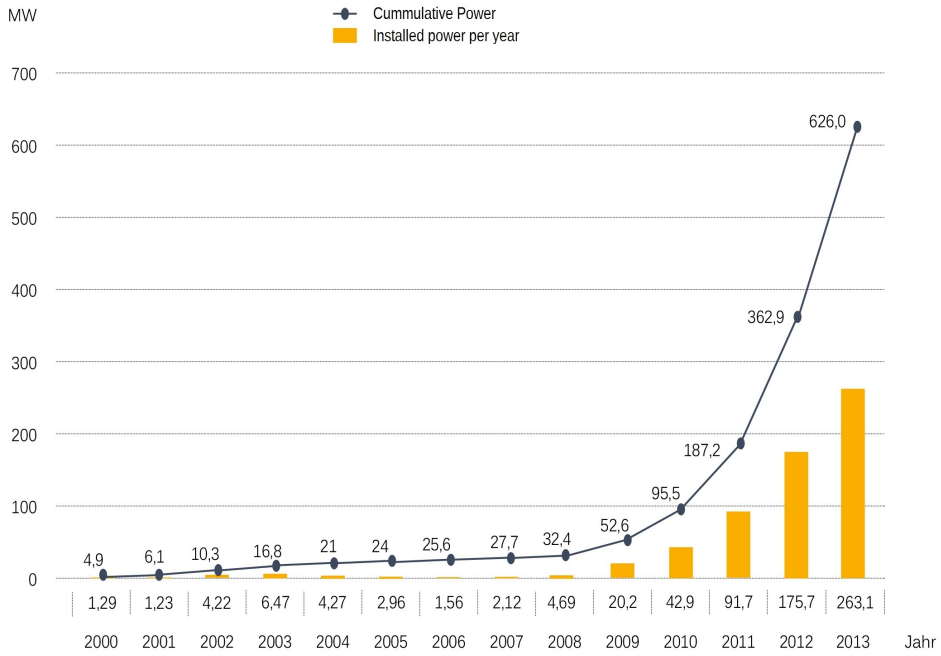

Fig. 1.4: The yearly installations of PV modules in Austria are growing since 2006 taken from [5].

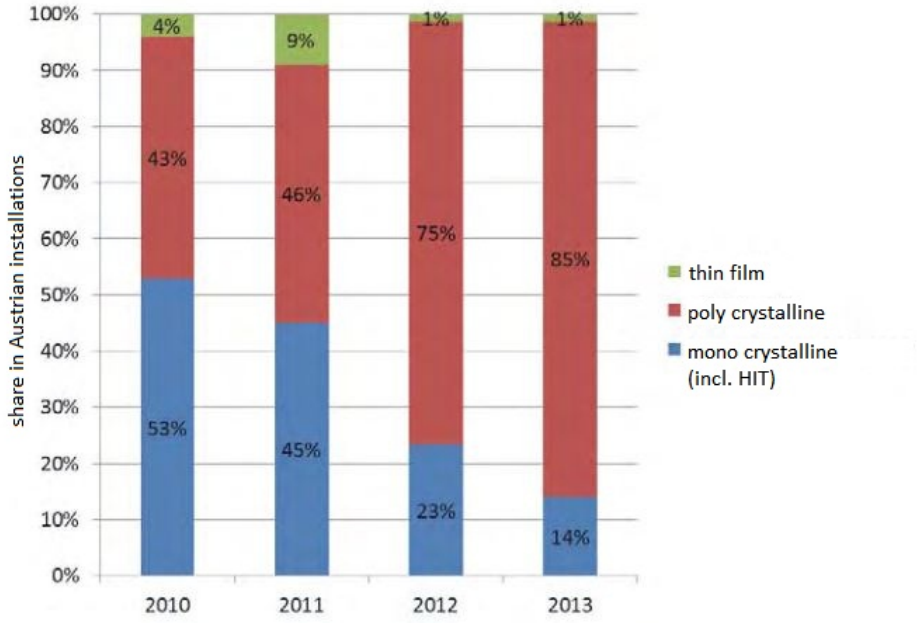

Fig. 1.5: The distribution of the installed PV technology is shown. Poly and mono crystalline modules dominate over thin film. In the last years the share of poly crystalline modules has nearly doubled. The graph is taken from [6].

ZnSe	ZnTe	GaP	CdTe	GaAs	InP	Si	Ge	HgSe	InSb	Sn
2.58	2.26	2.24	1.44	1.35	1.27	1.107	0.67	0.30	0.165	0.08

Tab. 1.1: The band gaps in eV of typical solar cell materials are presented at 300 K taken from [32] with the selection from [40].

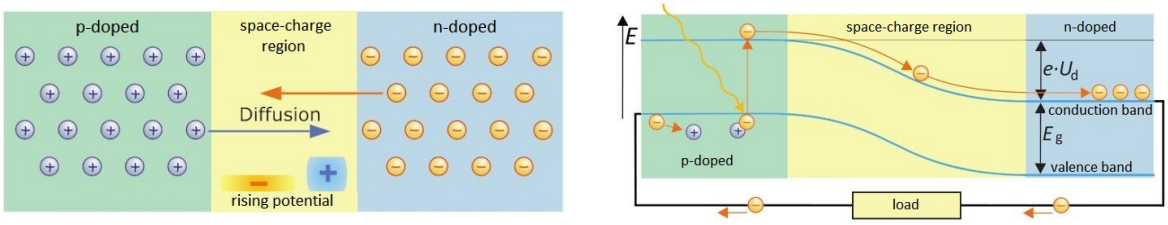

Fig. 1.6: Left the diffusion process at the pn-junction is sketched. Holes move to the right from the p-doped to the n-doped region, electrons move in the opposite direction, indicated by arrows. In between the space-charge region grows while the n-part increases in potential and the p-part decreases. The right figure depicts the resulting potential shape and further current generation. Both were taken from [40].

1.1.3 Functional description of solar cells

Some basic description of solar cells will be explained as following [40]: Solids are separated into metals, semiconductors and insulators, which mainly differ through the size of the band gap between valence and conduction band, which may overlap for metals. For semiconductors the band gap is less than 5 eV (see Tab. 1.1 for common solar cell materials). To rise an electron from the valence band to the conduction band, leaving a hole as positive charge carrier in the valence band, the electron needs to absorb at least the energy of the band gap.

Solar cells generate electrical current from solar illumination. By using the inner photoeffect, a photon is absorbed by an electron, which in turn is excited to a higher energy level. Contrary to the outer photoeffect in general needs higher photon energy, because electrons are released from a solid - if the absorbed photon's energy is above the work function of the solid.

To reduce the binding energy in semiconductor crystal lattices and gain additional free charge carriers, atoms with more or less valence electrons, compared to the actual semiconductor atoms, are added, this is called doping. Introducing *donators*, having more valence electrons, results in more free electrons, thus is called *n-doping*. Doping with atoms having less valence electrons is called *p-doping* with *acceptors*.

Attaching a p-doped semiconductor to an n-doped one initiates a diffusion process of the majority charge carriers across the border regions. Initially both semiconductors are neutral in charge, but have a majority of holes respectively electrons, which tend to attract each other. Thus the n-doped part will get a positive potential, while the p-doped one will reduce its potential (compare to Fig. 1.6). The increasing electrical field will damp the diffusion until equilibrium is reached. The resulting area between the semiconductors is then called *space-charge region* or *pn-junction*. As shown in Fig. 1.6 charge carriers in and around the space-charge region are then separated by the electric field, with electrons moving to the n-doped part.

Unfortunately reality is more complicated than this easy model. Generally the va-

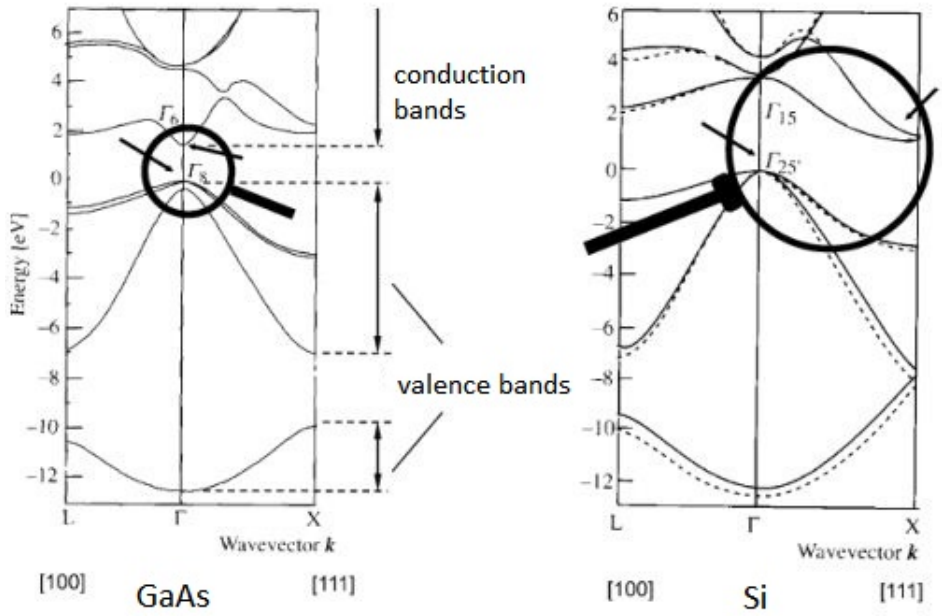

Fig. 1.7: The left graph shows the energy bands in the momentum space for gallium arsenide, the right graph for silicon. For gallium arsenide a photon with at least band gap energy can elevate an electron to the conduction band. In silicon the minimum of the conduction band and the maximum of the valence band differ in wave number. Therefore an absorbed photon with the band gap energy can not solely raise an electron, as the electron needs further momentum of a phonon. Images were taken from [45].

lence band and the conduction band vary in their minima and maxima across a two-dimensional area of a semiconductor. Further in momentum space a minimum of the conduction band is not necessarily at the same wave number (see Fig. 1.7). Semiconductors are called *direct*, if their valence band minimum is at the same wave number as the conduction bands maximum, otherwise they are called *indirect*. In indirect semiconductors, the electron needs to absorb the energy of a photon and needs further a certain momentum from a phonon to reach the conduction band - or a photon with more energy [45]. The probability of a photon-electron and phonon-electron interaction with ideal energy and momentum transmission is less then for an electron only absorbing a photon with ideal energy. Therefore silicon solar cells are in general manufactured thicker (around 180 μm [46]), than thin-film cells (below 10 μm [1]) for a comparable light absorbance, to increase the probability for creating free charge carriers [21], [29].

For the solar cell current generation mechanism, charge carriers are flowing in the so called *reversed bias* direction. A photon-excited electron moves from the p-doped part to the n-doped part, as shown in Fig. 1.6 on the right. *forward bias* would be the mechanism of an LED, attaching a positive voltage from the p-doped to the n-doped part. The current-voltage characteristic of solar cells in the simplest model is [47]

$$j(V) = j_{\mathrm{ph}} - j_{\mathrm{S}} \cdot \left[\exp\left(\frac{eV}{nkT} \right) - 1 \right] \ . \tag{1.1}$$

As solar cells vary in size in terms of their area, in general the current density is used

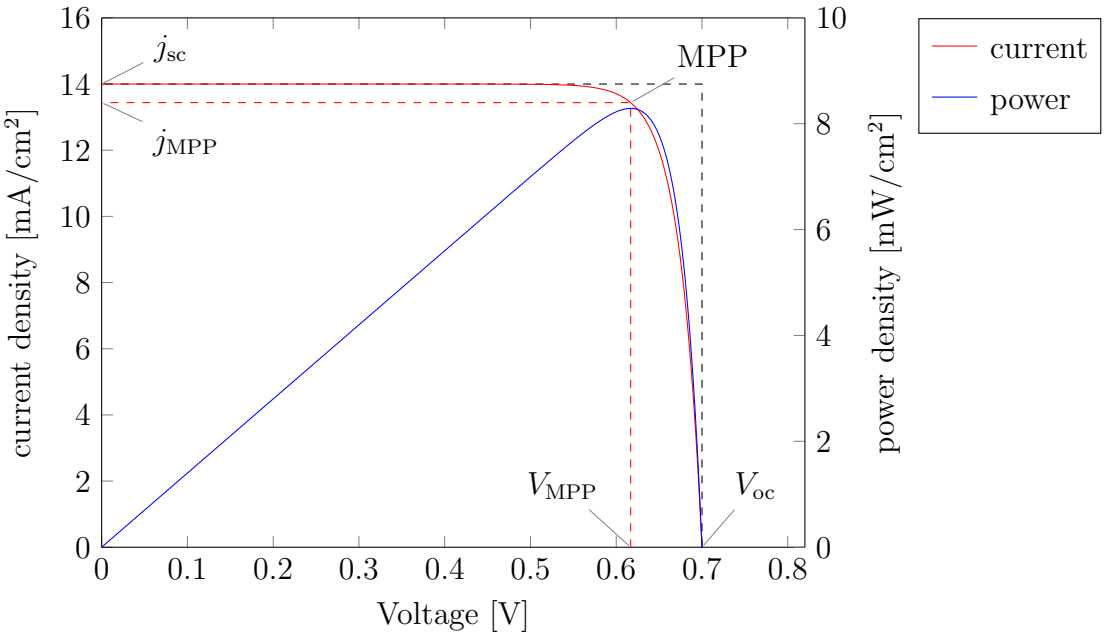

Fig. 1.8: An ideal IV-characteristic and power curve is plotted for a single cell using e/k=11604.5 K/V. The fill factor can be determined by the ratio of the MPP rectangle (red) to the big rectangle (black).

for better comparison, and shall be kept in mind if further talked about current. Here j_{ph} is the total generated photo current in the cell, and j_{S} is the reverse saturation current. The Boltzmann-term decreases the photo current due to the voltage V, and n is the ideality factor describing the recombination mechanisms in the cell, set to one in the simplest case, and typically varying between one and two [34], [12]. Fig. 1.8 shows the IV-characteristic of the solar cell with its important points.

A solar cell can be characterized by the *open circuit voltage* $V_{\mathrm{oc}} = V(j = 0)$, the *short circuit current* $j_{\mathrm{sc}} = j(V = 0)$ and the *maximum power point* MPP, defined by j_{MPP} and V_{MPP}. The ratio of these powers defines the fill factor FF

$$FF = \frac{j_{\mathrm{MPP}} V_{\mathrm{MPP}}}{j_{\mathrm{sc}} V_{\mathrm{oc}}} \,. \tag{1.2}$$

An important parameter is the *efficiency* η. It is defined as the ratio of electric output to incident power. In case of solar cells the incident power P_{in} of the whole spectrum on the earth's surface is assigned as 1000 W/m^2[40]. The maximum output power is in the maximum power point leading to [47]

$$\eta = \frac{j_{\mathrm{MPP}} V_{\mathrm{MPP}}}{P_{\mathrm{in}}} \tag{1.3}$$

This equation includes losses due to to non-absorbed light, thermal losses, charge carrier trapping and recombination mechanisms. Light absorbance depends on the band gap, theoretically cutting off any photons below, and on reflexions and transmissions, which are handled with light trapping and anti-reflexion coatings. Absorbed photons will only excite one electron-hole pair, which will dispense the energy difference be-

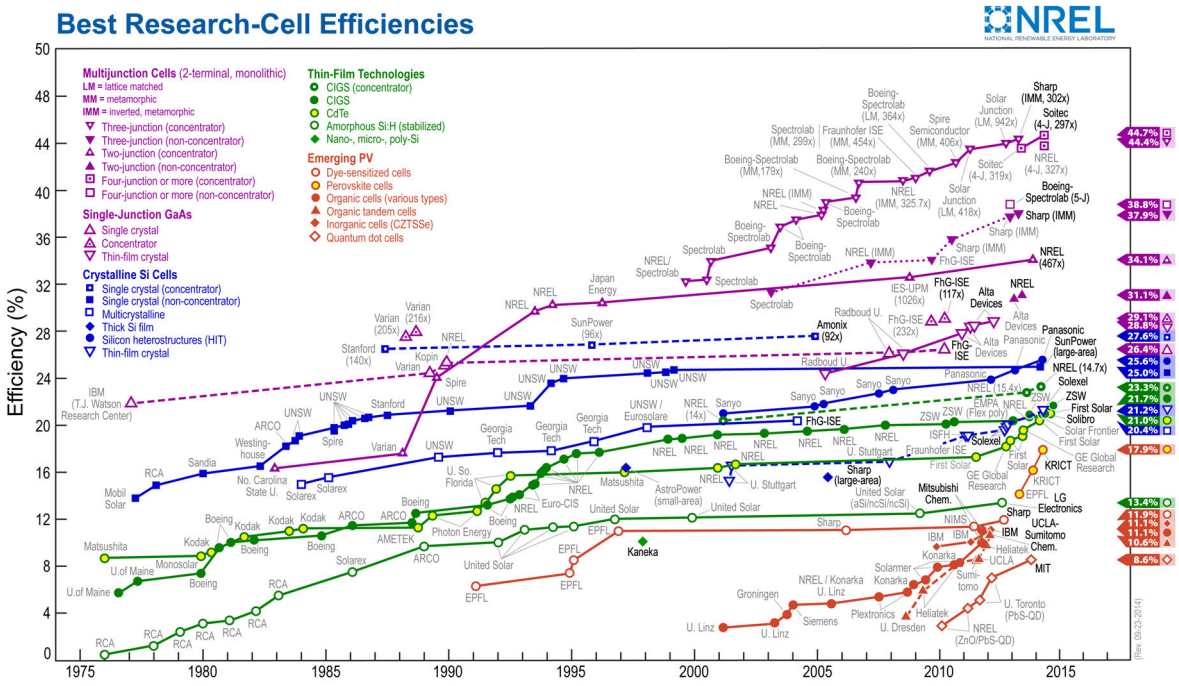

Fig. 1.9: The chart presents the chronological development of record-efficiency cells of different cell technology since 1976 and is updated periodically. This plot is courtesy of the National Renewable Energy Laboratory, Golden, CO

tween the photon and the band gap to heat [47].Only the generated charge carriers, which do not recombine, reach the electrodes and contribute to the output current. The currently best cell efficiencies are listed in Fig. 1.9.

Typically, solar cells are connected in series (called a *string*) and parallel to other cells to form a module. For cells with similar parameters the IV-characteristic from Fig. 1.8 extends proportional to the cells in series (extending voltage) and parallel (extending current). Challenges occur if cells don't fit to each other or if even one single cell differs in its electrical characteristics. This can happen for example, if a cell is shaded. Then the IV-characteristic shifts to less current. But due to series connection to the other cells the shaded cell carries higher current, than in its maximum power point. If expanding the IV-characteristic into the negative voltage half space, the slope is flat. Therefore a current mismatch can lead to high negative voltage in this cell and therefore to consumption of power, instead of production. This cell decreases the power output of the whole module by heating up.

The power loss is handled using *bypass diodes* (see Fig. 1.10). They are connected in parallel to grouped cells, called a *string* so that they don't shunt the cells in normal operation. If one of the cells is then e.g. shaded, the bypass diode will shunt the string, and the module will function, as one string were missing. For economical reasons (easier for manufacture), there is generally no bypass diode for each single cell. Therefore one corrupted cell will always block all other cells of its string.

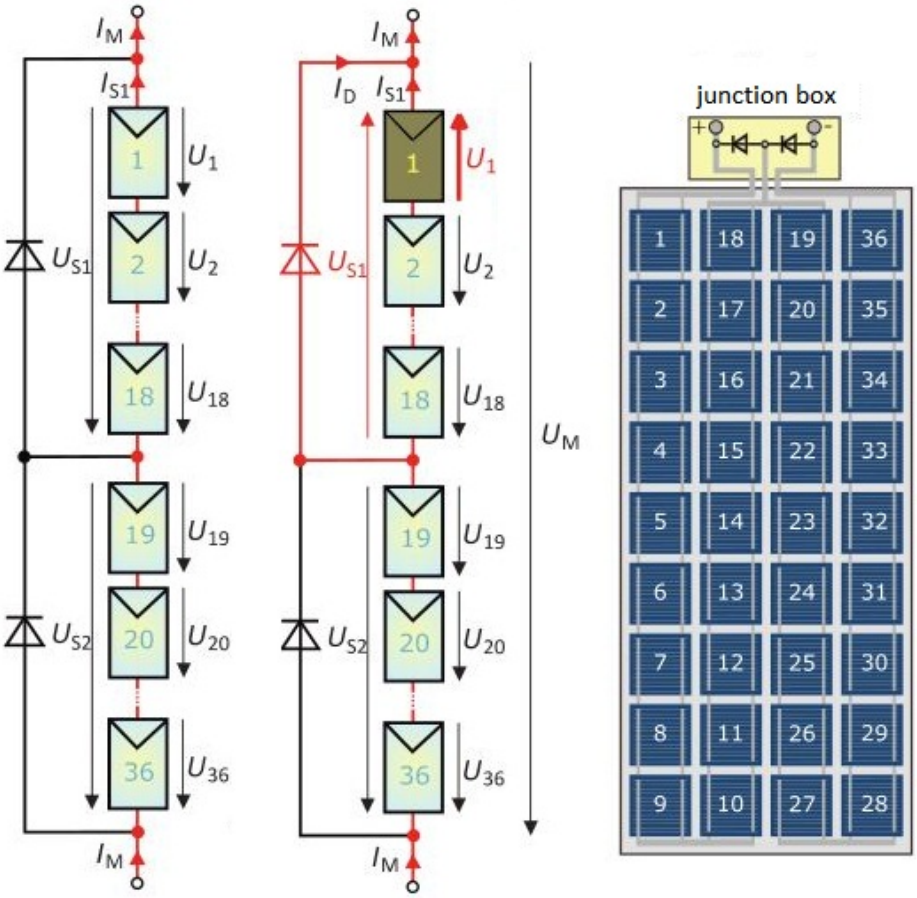

Fig. 1.10: The module on the right consists of two strings, each with 18 cells. On the left, the two strings are shown in a schematic with their bypass diodes. In the middle, the cell number 1 is shaded. The whole string from 1 to 18 is shunted than, while the second bypass diode is still inactive. This image is taken from [40].

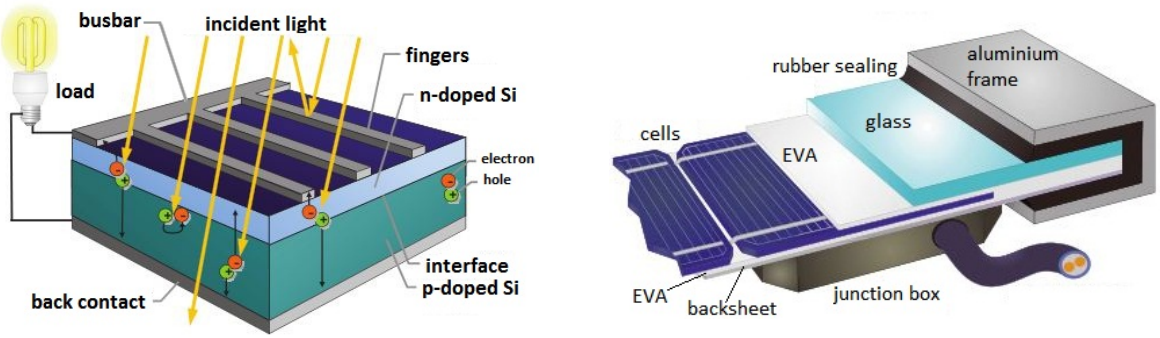

Fig. 1.11: Left, the layers of a silicon cell are shown. The right image shows how cells are integrated into a module. Images are taken from [40].

1.1.4 Crystalline cells

The manufacturing and layout of crystalline silicon cells will be explained following [40]. Metallurgical grade silicon is produced via reduction of quartz (SiO_2) with a purity of 98% at about 1800 °C, which is not pure enough. Cleaning it in the Silane-Process with the use of hydrochloric acid produces trichlor silan in an exothermic reaction, where solar grade-silicon can be separated with chemical-vapor deposition. Silicon is then deposited on a silicon bar at 1000 °C, creating silicon bars with a diameter of about 30 cm and a length of 2 m. Avoiding the cleaning process makes cleaning in the production process necessary, which is then called upgraded metallurgical silicon.

In the next step polycrystalline silicon can be produced by melting these bars and casting them into quadratic blocks. In this case silicon lattices with different orientations are mixed together, forming grain boundaries. The block is afterwards sliced and thereby quadratic polycrystalline silicon wafers are produced.

Monocrystalline silicon needs further treatment. The goal is to produce one big silicon lattice with as little crystal defects as possible. The typical processes are the Czochralski-process and float zone pulling. In the Czochralski-Process silicon is smelted, a single silicon crystal seed is put into the smelt and a monocrystal ingot is slowly pulled out. For float zone pulling a single crystal silicon seed is bonded to one end of a silicon rod and a heating coil smelts up the material, moving from the seed to the other end of the rod. Impurities thereby follow the heat, while the crystal is melting and crystallizing in mono crystalline form. All impurities are thereby moved to the other end of the bar, which will be cut off afterwards. The rest of the bar has higher purity [22].

These round ingots are then sliced to generate round wavers of a thickness between 150 and 350 μm. Squares with rounded edges are cut out, as they are easier to handle, but cutting out a sharp square would waste too much silicon.

The next step is the doping. Generally boron and phosphorous are attached to nitrogen or oxygen to diffuse into the silicon via gas diffusion process at around 1000 °C. The doping grade is dependent on the temperature, the gas velocity and the mixture of the gas. After doping, the surface is etched to clean it and the front and back contact is put upon it (see Fig. 1.11). The back contact is typically a metalized surface, while the front contact consists of busbars and fingers to shade as little surface as possible. As the silicon surface would reflect a lot of light, an anti-reflexion coating made of titan dioxide or silicon nitride (Si_3N_4) is applied. This layer makes the silicon cells look blue.

A module is better protected against environmental hazards than single cells. Typically 32 to 40 Cells with an edge length of 10-20 cm are arranged in a module. The cells are connected and then coated with EVA (ethylen-vinyl-acetate) on both sides at 100 °C and low-pressure in a process called laminating. A backsheet, made of some plastic is added to the back, and a low iron glass on the front side in one step. To avoid breakage of glass the module is surrounded with an aluminium frame and rubber sealing(see Fig. 1.11).

1.1.5 Thin film cells

Thin film modules are an alternative to crystalline silicon based modules. Big device areas are easier to manufacture, thus whole modules are manufactured in a single

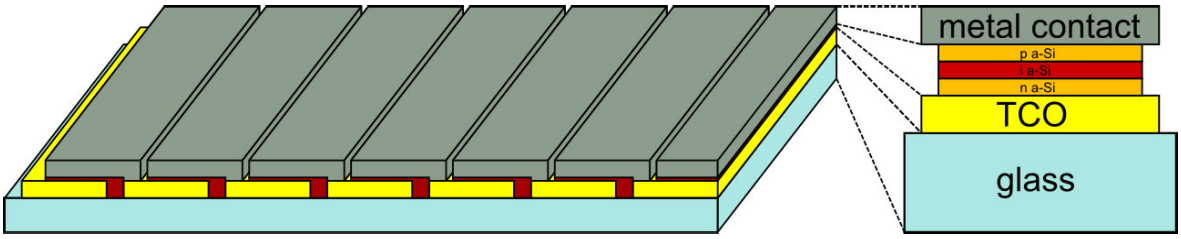

Fig. 1.12: On the right, the layers of a silicon solar cell are shown, the left depicts the formation of the cells to a module, redesigned from [21]. There is a gap between the metal contacts and the a-Si to avoid short cuts. Light goes through the glass and the TCO and then to a n-i-p a-Si cell, where i is an intrinsic layer usually less or even undoped compared to the p- and the n-doped a-Si.

deposition process, which in turn makes avoiding defects more important. The disadvantage is the difference in efficiency, where crystalline modules are around 20%, thin film modules are around 10% [40] and the advance of silicon high purity manufacture techniques above other materials. Main representatives for the thin-film technology are amorphous silicon (a-Si), cadmium telluride (CdTe) and copper indium selenide (CIS) [21], [23].

A-Si is deposited with silane (SiH_4) in chemical vapor deposition (CVD) at about 500 °C, where an alloy of silicon and hydrogen is formed. Therefore it is often written as a-Si:H. The processes are for example called plasma-enhanced CVD (PECVD) or hot wire CVD (HWCVD). The typical structure of an a-Si cell is shown in Fig. 1.12. The p-i-n structure is generally about 1 μm thick. Building a stack of different a-Si p-i-n structures can easily be performed, reducing the thickness of each single cell, forming a tandem cell with each cell having different band gaps, by using different alloys, leading to a better usage of the solar spectrum. Modules are produced in a *superstrate* process, depositing the cell on a *TCO* (=transparent conductive oxide) coated glass substrate. The TCO is used as front contact, while it is transparent for incident light and is first cut in stripes with a laser beam, then deposition takes place with further laser cuts to prevent shunts and provide a connection between the back metal contact and the TCO. Finally a module is generated as in Fig. 1.12, with all cells connected in series. A-Si has a drawback termed as light-induced degradation, which makes its efficiency drop a little, if exposed to light. The process can be reversed by heating the module to about 160 °C. [21]

CIS was further developed to CIGS, introducing gallium in addition to indium to shift the band gap. Today both technologies exist commercially. Their cells are produced in a *substrate* process, starting with the back side, in contrary to the a-Si module where the basic layers are front side. First 1 μm Mo as precursor layer is sputtered and deposited on a soda lime glass substrate. Then, the absorber material $Cu(In,Ga)Se_2$ is coevaporated and deposited at 500-550 °C on the precursor with a thickness of 1-2 μm. This p-doped layer is followed by the n-doped CdS-layer using chemical bath deposition (CBD). An undoped (indicated by the i for intrinsic in Fig. 1.13) ZnO layer is added by sputter deposition. And finally, a heavily doped ZnO:Al window layer is deposited after sputtering [2], [21]. In actual version of the chart in Fig. 1.9, CIGS cells show the best single cell efficiencies of all thin-film technologies.

CdTe is deposited on a TCO first, in Fig. 1.13 a combination of indium tin oxide

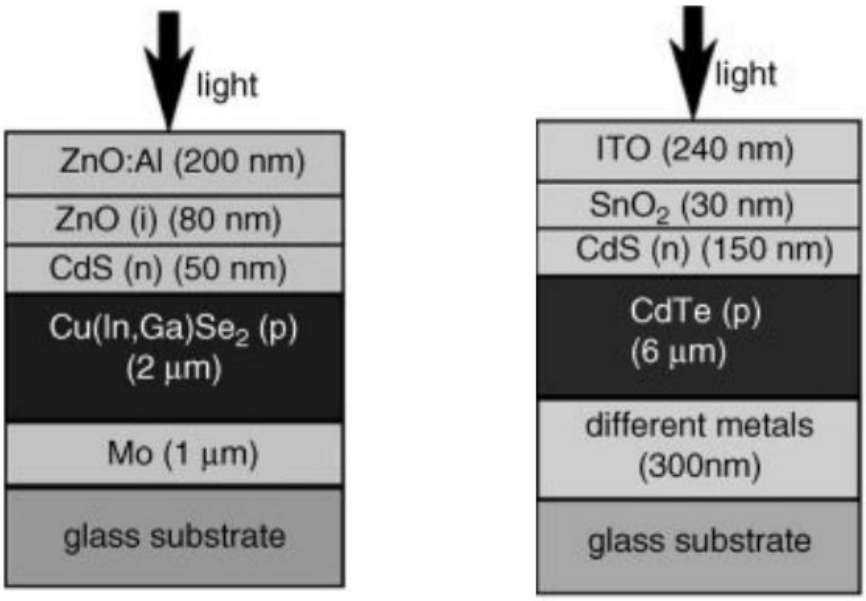

Fig. 1.13: The layers and their corresponding thicknesses for typical CIS (left) and CdTe (right) solar cells are shown, taken from [2].

(ITO) and SnO_2 is depicted. A thin CdS layer is provided for higher efficiencies. Then a CdTe layer with a thickness of 5-10 μm is added by, for example, close spaced sublimation (CSS). In this process the substrate area and the CdTe-powder are separated by a few mm or cm in rough vacuum (10^{-6} to 10^{-5} bar). By heating the substrate and the source with lamps, CdTe can be transported onto the substrate. Other processes are spraying, screen printing, sintering and electrodeposition. CdTe has its optical band gap close to the optimum and is easy to manufacture. One problem with these modules is the toxicity of the used materials, which is mainly a problem of acceptance in the markets [2], [21], [39].

1.1.6 Typical characterization methods

As solar cells and modules in general show inhomogeneities and defects, quality measurements enable the improvement of this technology. Further, certain effects can be analysed for scientific purpose. The following sections will be an introduction to some typical characterization methods.

Electroluminescence

The functional description showed that solar cells can be described as diodes with photons being absorbed, generating charge carrier pairs, which leads to a current. If a solar cell is driven in forward bias direction, charge carriers recombine at the band gap similar to a LED, emitting photons with an energy of the size of the band gap. This inversive process is called electroluminescence (EL) and leads any electrically driven part of the solar cell to emit photons.

The typical setups for spatial resolution is shown in Fig. 1.14. A CCD camera collects photons from a solar cell or a module, afterwards showing an image of the

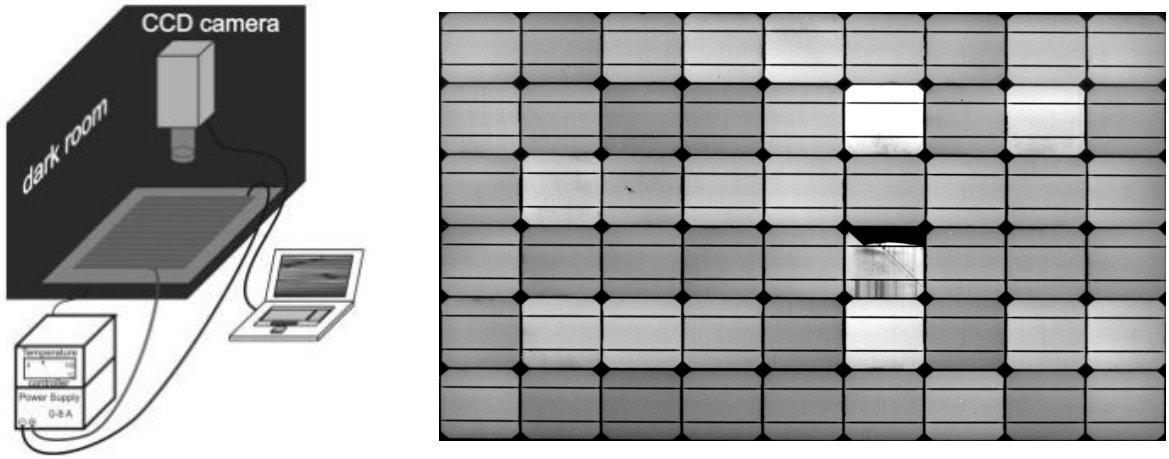

Fig. 1.14: The Schematics of an EL measurement setup for spatial resolution on the left is taken from [2]. On the right an example EL image of a mono crystalline silicon module is shown. The cells being more brighter show more activity, one cell can be identified as broken and on the left is a cell with a dark point, which has no photon output in the measured range.

spatial emission. Therefore only connected and working cells will be shown brightly, all others will be dark - including broken out parts as well as shunts. A typical EL image is shown in Fig. 1.14.

As this process is the reverse process of the photovoltaic electric energy generation principle, it visualizes differences in cell activity for connected cell parts and their performance. Measurement times reach from a few seconds up to some minutes, based on the driving current, for measuring one module [2].

Photoluminescence

Photoluminescence (PL) is a process visualizing photons emitted by electron transitions from higher to lower energy states after excitation due to incident light, which can be filtered, for providing only certain energy. Solar cells or modules don't need to be connected, so this method can be performed for blank wafers as well. The responding photon's energy is characteristic for different band-to-band transitions, depending on the incident photon's energy. This characterization method depends on the filtered energy range and the knowledge about the energy band structure of the material of investigation [2], [20].

A measurement setup can use various light sources as white light from a halogen or xenon lamp and may in some setups be filtered by a monochromator. Lasers and laser diodes were used as well, as in Fig. 1.15. In Modern setups infrared LED array illuminate a sample. A CCD camera behind a filter measures the photoluminescence radiation. An image from the investigation of a single polycrystalline cell in a module is shown in Fig. 1.15 [2], [31].

Bright / Dark thermography

For this characterization method, the setup does not differ from Lock-in thermography (without the modulation part), described closer in section 3.1. As for EL, photons

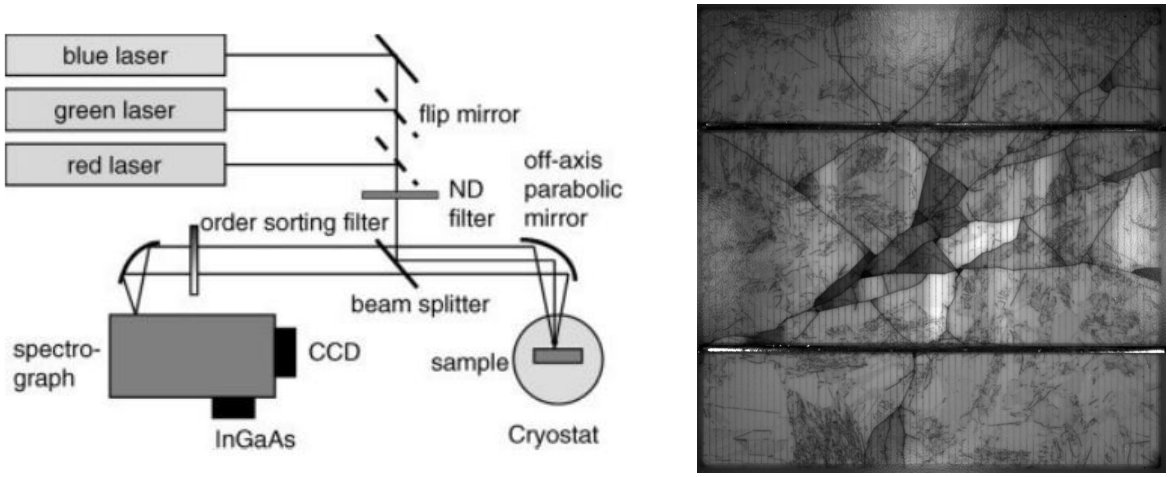

Fig. 1.15: Schematics of a PL measurement setup is shown on the left and taken from [2]. InGaAs is the chosen photo detector material. The right shows a sample PL image from a poly crystalline cell, which is broken apart in the middle. Though these pieces are not connected any more, the respond to the PL.

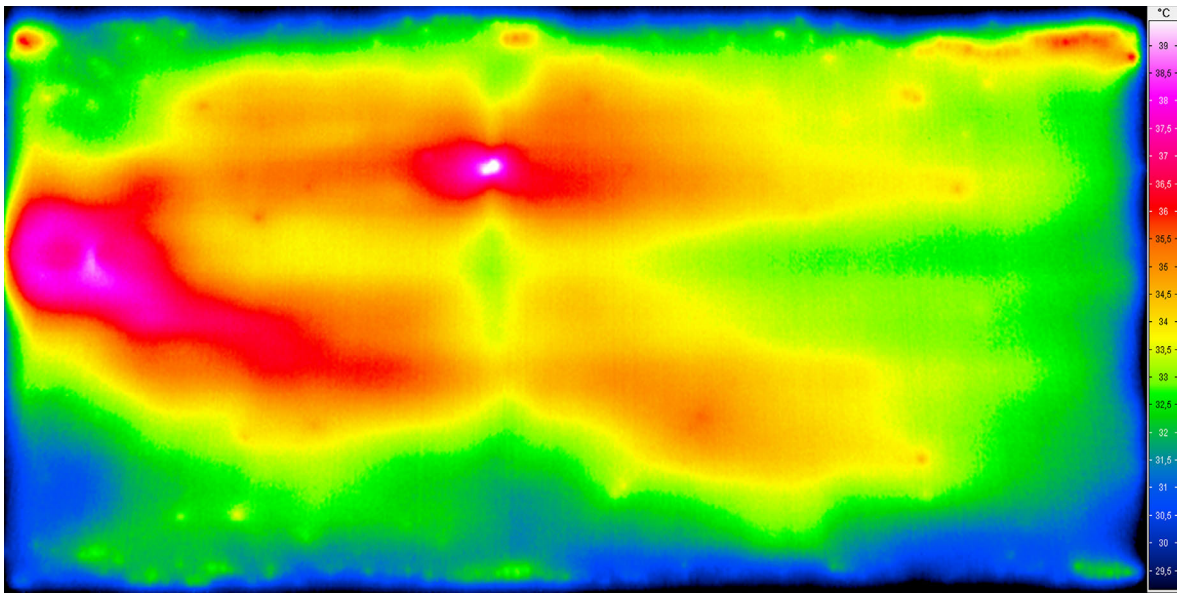

Fig. 1.16: A sample Dark thermography image is shown for a CdTe module. The range is between 29 °C and 39.5 °C.

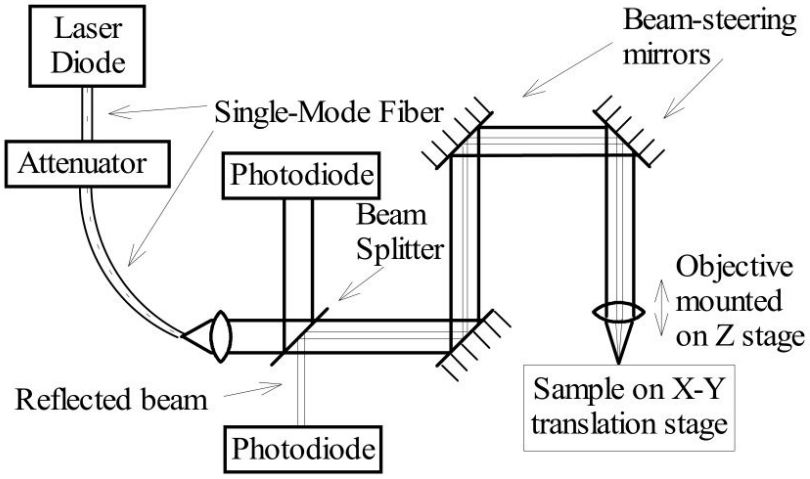

Fig. 1.17: Schematics of a LBIC measurement setup is taken from [24]. The upper photo diode measures the incident light intensity, the lower is evaluating reflected light.

are emitted by electrical stimulation, but the observed photon range is different. EL investigates band gap energies, thermography observes the thermal infrared. Thus this method looks at the spatial resolution of heating upon a module, an example is shown in Fig. 1.16. Dark thermography is easier, as a module is observed indoor, with as less environmental impacts as possible. Bright thermography can be performed outdoor and therefore needs to deal with wind, environment temperature variations, additional irradiation, which makes the method more qualitative.

Nowadays, hand held thermocameras are available which allow outdoor investigations as well. Instead of a current source for the dark, bright investigations may measure modules in situ or solely connected to a resistance. Various effects will lead to locally increase of temperature while a current flow is granted to the module. After some time, a thermography image is recorded [7].

LBIC outdoor/indoor

LBIC stands for light-beam-induced current. For this method a light source is focused on a surface spot of a solar cell. The resulting voltage is measured and the focus moves along the whole surface creating a 2D efficiency image. Extracted information include the uniformity of photo current response, local resistivity variations and the impact of defects.

A typical setup is shown in Fig. 1.17. A laser diode intensity is controlled by an attenuator. The incident light is measured by a photodiode and focused on the sample via some optical setup. The reflected light can be analysed as well, by a second photodiode. Spot sizes in the order of 1 μm to 2.5 mm were realized. The sample can be moved by a computer-controlled motorized cross table to raster a sample [18], [19], [24].

2 Theory

Dark Lock-in thermography combines the characterization method of thermography with the Lock-in principle. This chapter is intended to provide a theoretical background two these to topics and how they are combined to form the Dark Lock-in thermography mechanism, used in this thesis.

2.1 Sensoring Principle for radiative heat

Thermography is a non-contacting measurement technique. The temperature of a surface is determied by the thermal radiation it emmits. Therefore, important information about the spectrum, the dependence between radiation and temperature, and the infrared spectrum will be presented first. Afterwards, different detector and sensor types will be discussed, to provide a comparison to other sensors, than the used microbolometer.

2.1.1 Properties of the spectrum

In 1900, Max Planck calculated the radiation of a black body with discrete energy packets $h\nu$ multiplying Planck's constant h with the frequency ν for a mean oscillating mode. This replaced the continuous portions $k_B T$ derived by the product of Boltzmann's constant k_B and the temperature T of the black body, introduced by Rayleigh and Jeans. He resolved the "ultraviolet catastrophe" and introduced a formula for the spectral radiation density S_λ of a black body at a certain temperature in W/(nm m^2 sr) as the power per wavelength interval $d\lambda$ from a unit area dA into a steradian $d\Omega$ [11]

$$S_\lambda(\lambda, T)\ d\Omega\ d\lambda\ dA = \frac{2hc^2}{\lambda^5} \frac{1}{\exp(\frac{hc}{\lambda k_B T}) - 1}\ d\Omega\ d\lambda\ dA\ . \tag{2.1}$$

If radiation hits an object it can be reflected, absorbed and re-emitted or transmitted. According to Kirchhoff's law the absorbance and emittance of a body are equal. These phenomena are discribed by ratios called reflectance ρ, absorbance α, emissivity ϵ and transmittance τ while $\rho + \alpha + \tau = 1$.

A black body is characterized as an object which has an emissivity and absorbance equal to one [7]. This requires a transmittance and reflectance of zero. The emitted spectrum of a black body is further characteristic for its temperature. Fig. 2.1 shows Planck's law for two temperatures T =25 °C and T =50 °C.

Further derivation of (2.1) by λ and setting to zero results in Wien's law [11] by all constants combining to Wien's constant b_{Wien}. It states that higher temperatures shift

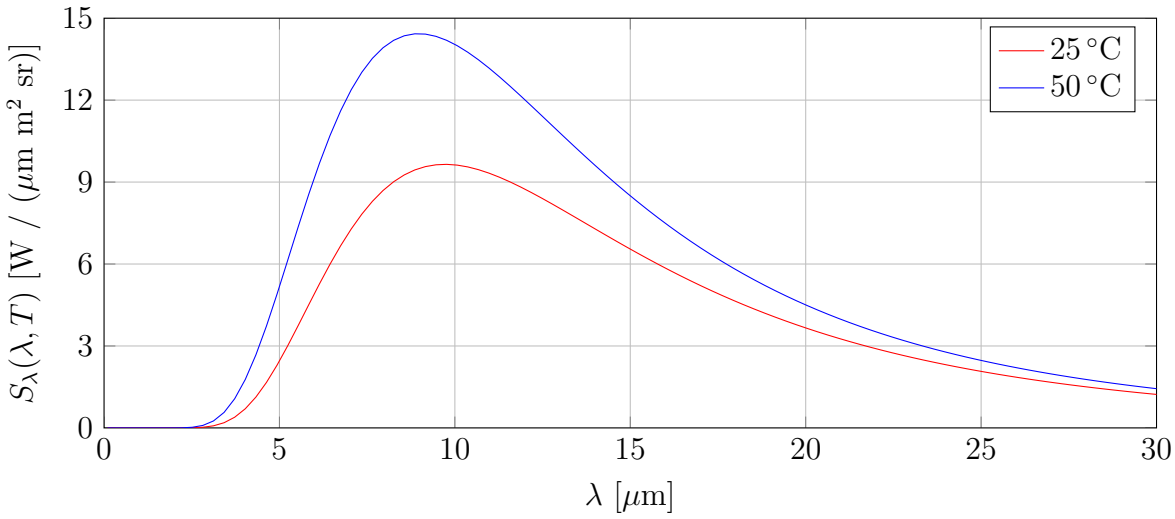

Fig. 2.1: Planck's law (2.1) is shown for T=25 °C and T=50 °C with h=6.62606896 · 10^{-34} Js, c=299 792 458 m/s and k_B = 1.3806504 · 10^{-23} J/K taken from the constant table in [10]. An object with 25 °C has its maximum at a wavelength of ≈ 9 μm.

the peak to lower wavelengths (see Fig. 2.1)

$$\lambda_m \cdot T = b_{\text{Wien}} \quad , \quad b_{\text{Wien}} = 2.897 \cdot 10^{-3}\,\text{K m} \,. \tag{2.2}$$

Integrating Planck's law (2.1) over all wavelengths and further integration over a half sphere returns the power P emitted per area A according to the temperature T of a body. This is called Stefan-Boltzmann law [11] with σ being the Stefan-Boltzmann constant

$$\frac{P}{A} = \sigma \cdot T^4 \quad , \quad \sigma = \frac{2\pi^5 {k_B}^4}{15c^2h^3} \approx 5.67 \cdot 10^{-8}\,\text{W m}^{-2}\,\text{K}^{-4} \,. \tag{2.3}$$

Properties of real materials

Hardly any object can be considered as a black body. In fact, most objects have an absorbance lower then 1 and thus show transmission and reflexion.

Concerning emissivity, there are two types of objects

- **grey emitters:** which have a non-wavelength dependent emissivity,
- **selective emitters:** which have a wavelength dependent emissivity.

For a real body surface with an emissivity < 1, the Planck's law (2.1) has to be multiplied by the emissivity of the specimen. In case of grey emitters, the emissivity can be considered constant $\epsilon = \epsilon_{\text{approx}}$ over the spectrum and the radiated power in the half space may be approximated as [42]

$$\frac{P}{A} = \epsilon_{\text{approx}} \cdot \sigma \cdot T^4 \,. \tag{2.4}$$

If the emissivity is varying too much due to the wavelength and can thereby not be approximated by a constant, Boltzmann's law has to be calculated by integrating

Name	Abbreviation	Wavelength Range [μnm]
Ultraviolet	UV	0.15 - 0.4
Visible	Vis	0.4 - 0.75
Near infrared	NIR	0.75 - 1.1
Shortwave infrared	SWIR	1.1 - 3
J Band	J	$\approx$ 1.25
H Band	H	$\approx$ 1.65
K Band	K	$\approx$ 2.2
Midwave infrared	MWIR	3 - 6
L Band	L	$\approx$ 3.6
Intermediate-wave infrared	IWIR	4 - 20
M Band	M	$\approx$ 4.7
Longwave infrared	LWIR	6 - 18
Very longwave infrared	VLWIR	18 - 50
Far infrared	FIR	25 - 100
Submillimeter	—	100 - 1000

Tab. 2.1: Nomenclatur of spectral ranges [35].

Planck's law (2.1) multiplied by the emissivity $\epsilon(\lambda, T)$ which is in general a function of temperature T and wavelength λ [42]

$$\frac{P}{A} = \int_0^\infty \epsilon(\lambda, T) \cdot S_\lambda(\lambda, T)\, d\lambda\,. \tag{2.5}$$

Often the emissivity is unknown. This is a major problem in thermography [7, Chapter 2.1]. According to [26] the emissivity for glass at 8-14 μm is about 0.92 and according to [27] PVC has an emissivity of 0.93-0.94 in LWIR and SWIR. These materials are interesting, as a PV module has glass at least on front side and some may have some sort of plastic as backsheet, taking PVC as reference (see section 1.1.4 and 1.1.5).

The Infrared Spectrum

Tab. 2.1 shows the different parts of the electromagnetic spectrum from. Thermographic investigations are performed in a range from 3 μm to 30 μm. The absorbance of water vapor and CO_2 leaves two windows in the atmosphere where good transparency can be achieved (see Fig. 2.2) and thermocameras do work in [7], [36]:

- **mid-range or short-range window:** 2 μm to 5 μm and
- **low-range window:** 8 μm to 14 μm.

2.1.2 Camera detectors

The detector of an infrared camera converts radiation to an electrical signal. The signal is generated by absorbing photons and thereby exciting electrons, raising temperature

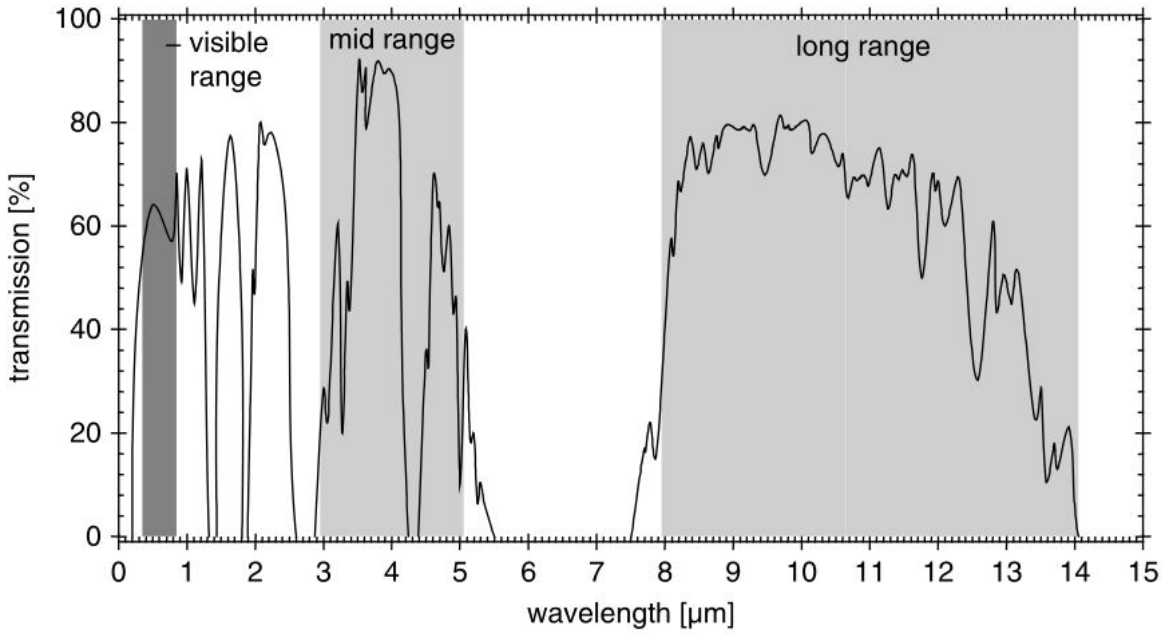

Fig. 2.2: The transmission of the atmosphere shows two windows in the infrared, used for thermocamera operation taken from [7].

or altering material properties e.g. the resistivity. The information in [35] will be summarized in the following section.

Usually a detector consists of an array of smaller sensors, *pixels* - each pixel representing the response of one sensor. A single sensor is often called *unit cell*. Such an array needs to be in the focus of the camera lens system and is called *Focal plane array* (FPA).

Every sensor generates an electrical signal which is read out through a multiplexer. The multiplexing readout circuit (*multiplexer* or *mux* in short) has several inputs and generates less output signals.

The most common sensor is the bolometer. Today the multiplexer and the focal plane array can be manufactured as one part (monolithic) or as two separate parts which are connected afterwards (hybrid, see Fig. 2.3). The latter may cause the problem of shorted sensors, delaminating and incomplete electrical contact. Monolithic arrays have the disadvantages of a lower fill factor and a more complex manufacturing process.

Sensors, where charge carriers (typically electrons) are generated, may be saturated before read out. Saturation is the upper bound of a sensor collecting charge carriers on on capacitor. The sensor can not handle any more charges and this may corrupt neighboring cells by distributing charges to them. This effect is called *blooming*. It happens, if a bright source (compared to visual photography) is viewed over a too large integration time.

There are two typical types of readout multiplexers called CCD and CID for thermocameras. A CCD (*charge coupled device*) shifts charges out of the detector through neighboring cells. In a line of separate sensors, the collected charge is moved from the first sensor to the readout, from the second to the first and so an. Charges (for the easier approach let it be electrons) are collected in a (positive) potential well. The electron is moved onto the next position by making this positions potential more positive

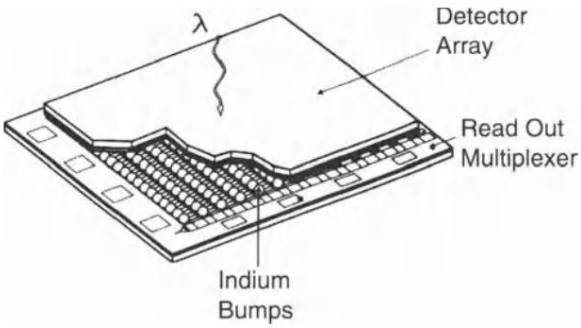

Fig. 2.3: FPA (here called "Detector Array") and multiplexer were manufactured as separate parts and got thereafter connected by "Indium Bumps". They form a connection by introducing heat [35].

than on the electrons actual position. Usually there are several positions and potential wells between two sensors - separating two gathered electron ensembles.

Typically the transfer efficiency of CCDs decreases exponentially with each shifting operation. Further, the readout process decreases the frame rate. An approach is to separate the FPA into subarrays and read them out separately. Another solution is using buried channels (underneath the surface) for the shift operation, which is faster, has a higher transfer efficiency, and therefore generates less noise. Furthermore, CCDs tend to bloom.

CID means *charge injection device*, each sensor has two separate MOS (*metal oxide semiconductor*) capacitors which store the charge and can be addressed directly by the sensors 2D position in the array by voltage addressing techniques. Furthermore, each sensor can be read both destructive or non-destructive - being able to leave the charge in the sensor memory. CID cameras were replaced by CMOS cameras in the consumer section, but are still available for research and industrial requirements [14]

2.1.3 IR sensor types

Various sensor types can be used, which also apply to different parts of the IR spectrum. Some sensors are shortly discussed in this section following [35]. Bolometers were explained in more detail, as the thermocamera in this thesis uses a microbolometer array.

Photoconductive sensors (PCS)

Through the inner photoeffect electrons are excited to the conduction band and thereby change the resistivity of the material. It needs to be considered that the applied current produces additional heat. The advantages are high gain and easier manufacturing [36].

Photovoltaic sensors (PVS)

As PCS, PVS also uses the inner photoeffect to generate an electron in the conduction band, but here the electron and the hole are sensed by measuring the generated voltage difference. Compared to PCS, this method has a better sensitivity by a factor of $\sqrt{2}$. Sensors for PCS and PVS exist for SWIR to LWIR.

Shottky barriers

This sensor works by transferring electrons from a metal to a semiconductor. By the inner photoeffect a photon excites an electron. The electron is bound in the metal by a potential well. By applying a certain voltage, the potential well height and thereby a cut-off wavelength for incident photons can be set. As well as for PVS and PCS, sensors exist for small to long wave infrared [30].

Quantum wells

These sensors consist of alternating semiconductor layers with different band gaps. E.g. GaAs has a smaller band gap and is surrounded by AlGaAs, which has a higher band gap. An applied bias then generates a potential well in the conduction and the valence band according to the difference in the band gaps. The potential well leads to certain quantum states within the conduction band, where electrons can get excited by a photon within the conduction band to a different energy level and same applicable for holes in the valence band. This allows smaller transition energies and therefore, longer wave lengths to be absorbed. It is stated that materials with such small band gaps are more difficult to grow, therefore this sensor type is an alternative using larger bandgap materials. A disadvantage is the low optical absorption of less then 1%. So-called multiquantum wells are intended to increase absorption by stacking [33].

Bolometers

Bolometers are very commonly used and were invented in 1881 by Prof. Langley [44]. Thermal radiation will be absorbed by an absorber material. The absorber should have a low heat capacity to follow changes rapidly and a large absorptivity, typically for 8 - 14 μm, which is in LWIR [17], [36]. The heat will then be transported to a reference resistor, which has a known temperature dependence of its resistivity, a small heat capacity, and low electrical noise. They are connected by a thermal link with high thermal conductance. The resistor also needs to be connected to an appropriate heat sink to decrease thermal noise. Typically a mechanical structure is provided that elevates the bolometer (see Fig. 2.4) [41]. Often a reflector is added to the microbolometer [17].

Early approaches were using the big resistivity change at the transition temperature of superconductors. This lead to massive cooling to less than 4 K. They had low sensitivity, slow response and a large center-to-center spacing of single sensors in an array. Nowadays so called microbolometers or "uncooled bolomotric arrays" (though cooled with peltier elements) are used, which are able to operate at room temperature. Such arrays typically consist of pixels at the size of 17 x 17 μm [17]. A main advantage is the wavelength independent sensitivity.

Pyroelectric

Radiation is absorbed and changes the temperature of the sensor. The temperature change invokes a current by changing surface charges. "*By adding an electric field, the pyroelectric effect can be increased to a value proportional to (temperature-dependent) electric permittivity $\mu(T)$ of the dielectric. This is called the 'field amplification of*

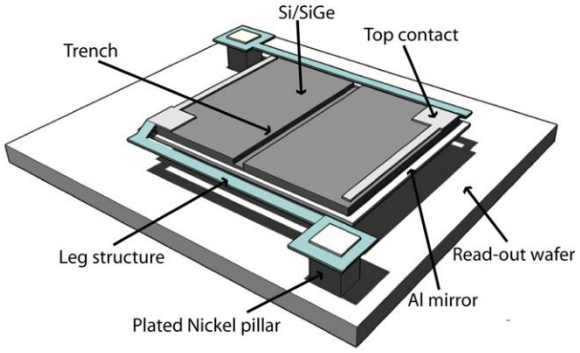

Fig. 2.4: In the depicted single microbolometer pixel, a Si/SiGe thermistor is used. The legs are sandwich structures of SiN with TiW in between, where TiW is used as electrical contact to the nickel. The resistivity can be measured through the two nickel structures which elevate the sensor. Picture taken from [17].

pyroelectric effect' or 'bolometric ferroelectric effect'" [36]. This property makes them useful as motion sensors. For measuring a non-alternating temperature, the incident light to the sensor is chopped to produce a periodically alternating temperature signal. As bolometers they have the advantage of wavelength-independent sensitivity, while not absorbing below $5\,\mu$m for typical materials without a certain coating, and room temperature usage [36].

2.1.4 Properties of thermocamera sensors

An IR sensor can be described by many parameters. Some of these will be shortly explained in this section.

NEDT

This stands for *noise equivalent delta temperature* (often called NETD for *noise equivalent temperature difference* as well [36]). It corresponds to the difference in temperature on a sample that matches a camera pixels noise. These temperatures are therefore not resolvable [35]. NEDT may also be called *temperature resolution* and can be calculated, with knowing the background temperature T_0, the actual sample temperature T_{sample}, the RMS noise voltage U_{noise} of the camera and the output voltage generated U_{out} by T_{sample}

$$\text{NEDT} = \frac{T_{\text{sample}} - T_0}{\frac{U_{\text{out}}}{U_{\text{noise}}}} = \frac{U_{\text{noise}}}{U_{\text{out}}} \cdot \Delta T \,. \tag{2.6}$$

If the output signal equals the RMS noise, the temperature difference equals the NEDT. [36]

Quantum efficiency (QE)

The quantum efficiency is defined as the ratio of the electrons generated to the amount of incident photons. Thus the value is between zero and one and wavelength dependent,

as different wavelengths λ have different energy packet-sizes of photons defined by $E_\gamma = h \cdot \frac{c}{\lambda}$ with h being Planck's constant and c being the speed of light. It may be measured using an incident monochromatic beam of defined power for the certain wavelength.

Responsivity

This parameter describes the output current, if the incident radiation has the power of one Watt (sometimes also measured in volts per watt) [35].

Readout noise

Each detector has its own readout noise that depends on the temperature and its design. It adds up to other noise sources [35].

2.1.5 Narcissus effect

The Narcissus effect causes additional reflection problems to the measurement setup: If a thermography camera is orthogonally looking on a plane sample (e.g. a photovoltaik module which has a flat front and back side), it might see itself as a reflection on the surface. This corrupts the measurement because the camera inside might be cooled, while the outside has higher temperature, and hence the reflexion is inhomogeneous and will overlay with the sample response. Inclining the camera from orthogonal vision to the object adds image distortion to the measurement, avoids back reflection to the camera itself [7]. This was applied to the measurement setup in section 3.1.

2.2 Thermal Conduction

The radiative heat transport has been discussed above. This section is dealing with the thermal processes in a sample. Therefore, the heat diffusion equation and its solutions will be discussed. The final section, about the processes in solar cells, will provide background information on this sample type, investigated in chapter 3.

2.2.1 Heat diffusion equation for solids

Assuming a temperature difference ΔT between two thermally connected locations x_1 and $x_2 = x_1 + dx$ introduces a temperature gradient $\partial T/\partial x$ in location x between them. Experiments show that (according to the 2^{nd} theorem of Thermodynamics) there will be a thermal flux, proportional to the cross section area A between x_1 and x_2 via the thermal conductivity in W/(K m) λ [10]

$$\frac{\partial Q_x}{\partial t} = -\lambda \cdot A \cdot \frac{\partial T_x}{\partial x} \ . \tag{2.7}$$

In vector notation T is a time dependent skalar field $T(\vec{r}, t)$ in three-dimensional space $\vec{r}$. Then the heat flow $\partial_t Q = \dot{Q}$ can be written as surface integral over the the negative temperature gradient and the according proportionality constant $\lambda = \lambda(\vec{r})$ resulting in

$$\partial_t Q = -\oint_A \lambda(\vec{r}) \ \nabla T(\vec{r}, t) \ d\vec{A} = -\int_V \nabla \cdot (\lambda(\vec{r}) \ \nabla T(\vec{r}, t)) \ dV \ , \tag{2.8}$$

transformed to a volume integral over the divergence by Gauss's theorem.

Further the heat in a material with mass density $\rho(\vec{r})$ is proportional to the temperature $T(\vec{r}, t)$ of the body via the specific heat $c_{\mathrm{p}}(\vec{r})$ [10]

$$Q = \int_V \rho(\vec{r}) \ c_{\mathrm{p}}(\vec{r}) \ T(\vec{r}, t) \ dV \ . \tag{2.9}$$

Deviating by the time t will only affect the temperature $T(\vec{r}, t)$ and results in the difference of heat content of the body

$$\partial_t Q = \int_V \rho(\vec{r}) \ c_{\mathrm{p}}(\vec{r}) \ \partial_t T(\vec{r}, t) \ dV \ . \tag{2.10}$$

Setting (2.8) and (2.10) equal plus a space dependent, specific heat introduction term $\partial_t q(\vec{r})$ in the volume V results in the integral equation

$$\int_V \rho(\vec{r}) \ c_{\mathrm{p}}(\vec{r}) \ \partial_t T(\vec{r}, t) \ dV = -\int_V \nabla \cdot (\lambda(\vec{r}) \ \nabla T(\vec{r}, t)) \ dV \ + \ \int_V \partial_t q(\vec{r}) dV \ . \tag{2.11}$$

This can be re-written to a differential equation as the three-dimensional *heat diffusion equation*

$$\rho(\vec{r}) \ c_{\mathrm{p}}(\vec{r}) \ \partial_t T(\vec{r}, t) = -\nabla \cdot (\lambda(\vec{r}) \ \nabla T(\vec{r}, t)) \quad + \quad \partial_t q(\vec{r}) \ . \tag{2.12}$$

Assuming a homogenous and isotropic body, the proportionality factors and the density can be considered as constant. This leads to

$$\rho c_{\mathrm{p}}\ \partial_t T(\vec{r},t) = -\lambda \Delta T(\vec{r},t)\ +\ \partial_t q(\vec{r})\ . \tag{2.13}$$

Then the one-dimensional heat diffusion equation for a temperature $T = T(x,t)$ can be optained as

$$\rho c_{\mathrm{p}} \frac{\partial T(x,t)}{\partial t} = \lambda\ \frac{\partial^2 T}{\partial x^2}(x,t)\ -\ \partial_t q(\vec{r})\ . \tag{2.14}$$

2.2.2 The diffusion length

An interesting one-dimensional physical system is, a periodically oscillating heat source $P_0 \cdot \exp[i\omega t]$ with vanishing temperature in infinite distance. This case can be considered, if an areal heat source at the surface of an infinitely thick body, introduces one-dimensional heating into the body - in z-direction - with a frequency $f = \omega/2\ \pi$.

For this case a possible soultion of (2.14), can be derived separating the differential equation for a time dependent part proportional to $\exp[i(\omega t+\phi)]$ and a space dependent damping part proportional to $\exp[\alpha z]$ to [7]

$$T(z,t) = A \cdot e^{-\frac{z}{\Lambda}} \cdot e^{i(\omega t - \frac{z}{\Lambda} + \phi)}\ , \tag{2.15}$$

where ϕ is a possible arbitrary phase shift and

$$\begin{aligned} \Lambda &= \sqrt{\frac{2\lambda}{\rho c_p \omega}} \text{ and} \\ A &= \frac{p_0}{\sqrt{\lambda \omega c_p \rho}}\ . \end{aligned} \tag{2.16}$$

Λ is called the *thermal diffusion length*. It determines the damping of temperature with distance.

The amplitude and phase are derived by using (2.7) as Neumann boundary condition at $z = 0$ for the temperature and the specific power p_0 per unit of the heat introduction surface in $\mathrm{W/m^2}$ with an external time dependent oscillation $\exp[i\omega t]$.

$$\begin{aligned} p_0 \cdot e^{i\omega t} &= -\lambda \cdot \left(-\frac{A}{\Lambda}(1+i) e^{-\frac{z}{\Lambda}\cdot(1+i)} \cdot e^{i(\omega t+\phi)} \right)\Bigg|_{z=0} \\ p_0 &= \frac{A\lambda\sqrt{2}}{\Lambda} \cdot \underbrace{\frac{(1+i)}{\sqrt{2}} e^{i\phi}}_{=1,\ \phi=-\pi/4}\ . \end{aligned}$$

As the amplitude is chosen to be real, an assumed periodic areal heat source leads to a phase delay in temperature at the origin of $\pi/4$, if expanded by $(\sqrt{2}/\sqrt{2})$.

Amplitude and diffusion length do depend on material parameters and the driving frequency which will be further discussed in the next sections. Fig. 2.5 shows the diffusion length for different materials with the material parameter taken from Tab. 2.2.

Material	**Density** [kg/m^3]	**Specific Heat** [J/(kg K)]	**Heat Conductivity** [W/(m K)]	**reference**
silver	10 525	234	407	[7]
glass (window)	2 700	840	0.78	[7]
silicon	2 330	700	149	[7]
CdTe	5 860 (at 300 K)	210	6.2 (at 20 °C)	[37]
PVC	1 400	880	0.16	[7]

Tab. 2.2: This table presents an overview of different material parameters for calculating the diffusion length according to (2.16).

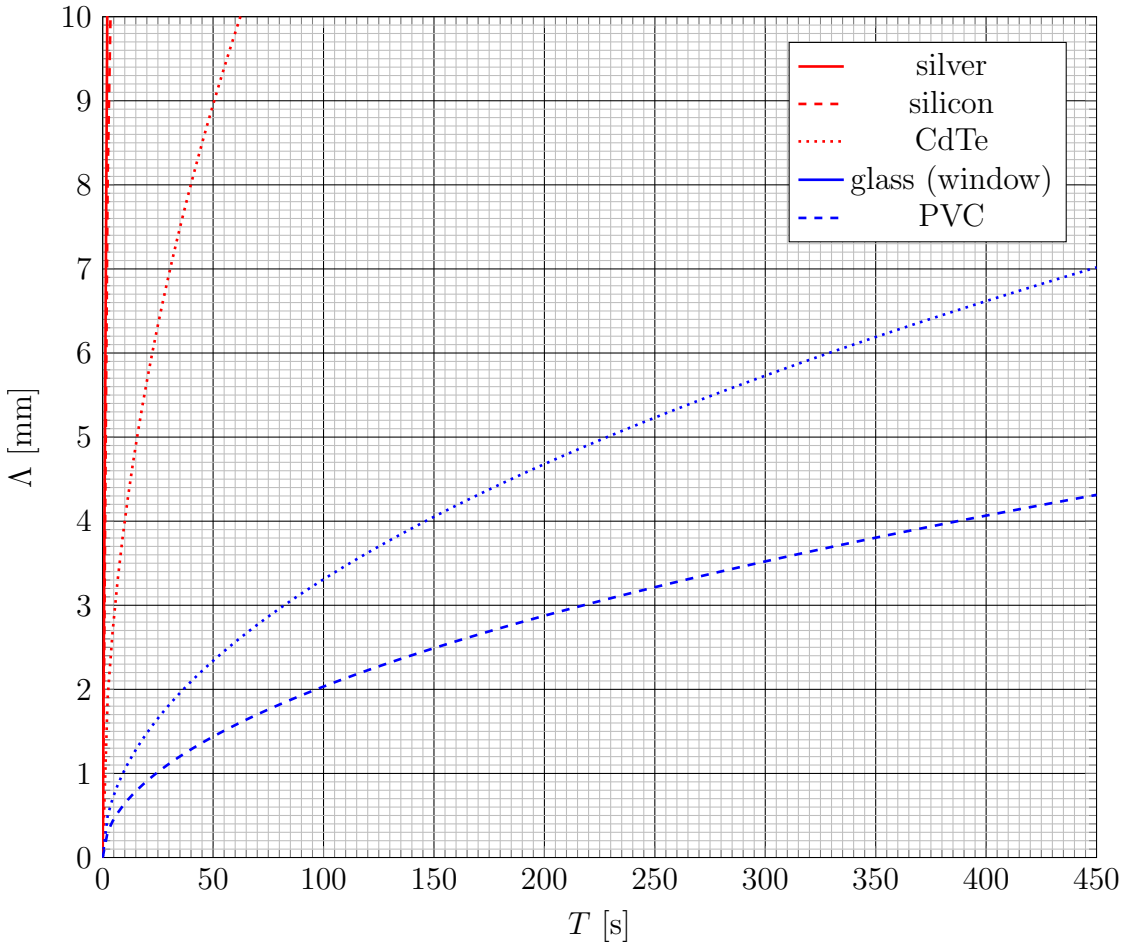

Fig. 2.5: The $1/\sqrt{f}$ dependence of the diffusion length from (2.16) is shown for different materials. The material parameters are listed in Tab. 2.2. Higher diffusion length means farther temperature expansion in the material. Silver as a metal shows far temperature extension as do silicon and CdTe, used for solar cell production (see section 1.1.4 and 1.1.5). Higher frequencies decrease temperature extension, also for good conductors. According to the shape of glass and PVC, they are most responsible for the thermal thickness of PV modules on front and back side. Furthermore, thin film cells have a physical thickness of about 1-10 μm and can thereby considered as thermal thin (see section 1.1.5).

Thermal thickness

The thermal thickness will be introduced following [7] to compare different materials in terms of the introduced heat waves. This modeling is based on the diffusion length Λ and its damping of the temperature which is thus negligible for longer distances.

Therefore samples with a thickness above the diffusion length are called *thermally thick* and thinner samples are called *thermally thin*. As the diffusion length is based on material parameters and on the frequency of an oscillating heat introduction, different materials could be considered thermally thin, even if their physical thickness is not comparable.

Thermally thin samples show no temperature gradient in the height. That makes it possible to model them in 2D and neglect temperature differences between the above and the bottom surface. This needs to be considered, for instance if a thermally thin sample is mounted on a heat sink, which changes the thermal behavior of the sample dramatically.

In contrast thermally thick samples can be considered as infinitely thick and a heat sink on the bottom does not affect the heat spreading in the above surface, when heat is introduced above. These samples need to be modeled in 3D.

2.2.3 Heat sources

According to the shape, there are three main heat sources: Point, extended and line heat sources. These are further modeled differently for thermally thick or thin bodies.

Point sources

The two-dimensional solution in section 2.2.2 can be extended to the three-dimensional space following [7]. The heat diffusion equation (2.13) will be solved for a point heat source inside an isotropic and homogeneous (for the first approach infinite) body, which is periodically heated with $P(T) = P_0 \cdot e^{i\omega t}$. The solution can again be obtained by separation of the differential equation as in section 2.2.2, but with the damping being proportional to $1/r \ \exp[\alpha r]$ due to the spherical symmetry as

$$T(r,t) = \frac{A}{r} \cdot e^{-\frac{r}{\Lambda}} \cdot e^{i(\omega t - \frac{r}{\Lambda} + \phi)} \ , \tag{2.17}$$

The diffusion length is the same as in (2.16), the amplitude changes and again an arbitrary phase ϕ is added for general solution.

The Neumann boundary condition of the introduced heat $P(t) = P_0 \cdot e^{i\omega t}$ is chosen for an infinitely small volume at the origin. Thus, heat is introduced to a spherical surface $4\pi r$ with a radius r approaching zero. Using (2.7) with this boundary condition

returns

$$\begin{aligned} P_0 \cdot e^{i\omega t} &= \lim_{r\to 0}\left(-4\pi r^2\lambda\left[(-1)\cdot\frac{A}{r^2}\cdot e^{i(\omega t+\phi)}e^{-r\frac{\sqrt{2i}}{\Lambda}} - \frac{A}{r}\cdot e^{i(\omega t+\phi)}\cdot\frac{\sqrt{2i}}{\Lambda}\cdot e^{-r\frac{\sqrt{2i}}{\Lambda}}\right]\right) \\ &= 4\pi\lambda\cdot e^{i(\omega t+\phi)}\left[A\cdot\lim_{r\to 0}(e^{-r\frac{\sqrt{2i}}{\Lambda}}) - \lim_{r\to 0}(r\cdot A)\cdot\frac{\sqrt{2i}}{\Lambda}\cdot\lim_{r\to 0}(e^{-r\frac{\sqrt{2i}}{\Lambda}})\right] \\ &= 4\pi\lambda\cdot e^{i(\omega t+\phi)}\left[A\cdot 1 - 0\cdot\frac{\sqrt{2i}}{\Lambda}\cdot 1\right] = A\ 4\pi\ \lambda\ e^{i\omega t+\phi} \quad \rightarrow \quad \phi = 0\,. \end{aligned}$$

Thus the amplitude (for an infinitely thick body) is

$$A = \frac{P_0}{4\pi\lambda} \tag{2.18}$$

and is further not dependent on the driving frequency in this case, and the specific heat capacity, but still on the heat conductivity. Here the temperature function is in phase with the driving heat source. For emitting only in one half space the amplitude would need to be doubled and the scenario would change to a point source on the surface of a body.

Very small real heat sources can be approximated as point sources, if the resolution of the measurement system is bigger then the heat source extensions. IR cameras, for example (see section 2.1.2), which are collecting photons coming from a more extended area than the heat source, will integrate thereby over the whole source and cancel the divergence by averaging [7]. Otherwise the solution in (2.17) would diverge in source position, as $\lim_{r\to 0}(1/r) \to \infty$.

The infinitely thick body was an approach to avoid edge effects. As mentioned in section 2.2.2, the thickness of a body needs to be compared to its diffusion length. For a thermally thick body, the above solution holds. But for thin bodies of thickness $d \lesssim \Lambda$ it needs to be considered that the heat flow across the boundary is not allowed. Therefore cylindrical coordinates turn the three-dimensional problem into a two-dimensional one with radius r, height z and source position at the origin.

The heat flow can be cancelled across some arbitrary boundary by introducing mirror heat sources. In this model, adding a heat source $P_1 = P_0$ at the origin, would lead to doubled amplitude in one half space, as above. P_0 and P_1 hold for all thicknesses above Λ. For thinner bodies additional pairs of heat sources need to be introduced, the more, the thinner they get. Mirrors are always at $z = 0$ and $z = d$. For $d \approx \Lambda$ one source P_2 at $z = 2d$ has to block heat crossing $z = d$ with same magnitude as in source position $P_2 = 2 \cdot P_0$. Further P_2 needs to be cancelled at $z = 0$ with $P_3 = P_2$ in $z = -2d$. With these terms and the amplitude in (2.18), (2.17) turns into

$$\begin{aligned} T(r,T) = \frac{1}{4\pi\lambda}\Bigg[&\frac{2P_0}{r}\cdot e^{-\frac{r}{\Lambda}}\cdot e^{i(\omega t-\frac{r}{\Lambda})} \\ &+ \frac{(2+2)\cdot P_0}{\sqrt{r^2+4d^2}}\cdot e^{-\frac{\sqrt{r^2+4d^2}}{\Lambda}}\cdot e^{i\left(\omega t-\frac{\sqrt{r^2+4d^2}}{\Lambda}\right)}\Bigg]\,, \end{aligned} \tag{2.19}$$

where $(2+2)$ comes from $P_2 = P_3$, which are both $2d$ away from source position.

Further decrease of d/Λ will lead to more and more pairs of heat sources, with d approaching 0, turning into a line heat source parallel to the z axis. This source still has cylindrical symmetry, but the problem reduces to the first dimension in r.

Line sources parallel to z

The solution of the heat diffusion equation (2.13) for line sources is obtained following [7] by using cylindrical coordinates (r, ϕ, z) where radial symmetry leaves a one-dimensional problem in r. It is equivalent to a point source in a thermally thin body.

The solution is described by the modified Bessel function of second kind of order zero $K_0(x)$, or by the so-called *Kelvin functions* $ker(x)$ and $kei(x)$

$$\begin{aligned} T(r,t) &= AK_0\left(\frac{r}{\Lambda}(i+1)\right)e^{i(\omega t+\phi)} \\ &= A\left(ker\big(\frac{r\sqrt{2}}{\Lambda}\big) + ikei\big(\frac{r\sqrt{2}}{\Lambda}\big)\right)e^{i(\omega t+\phi)} \ . \end{aligned} \tag{2.20}$$

As in the previous section, Λ is the diffusion length and the amplitude can be calculated using the Neumann condition (2.7) with an oscillating line power source $P_0 \cdot e^{i\omega t}$ combined with and the cylindrical lateral surface area $2\pi rd$ for $r \to 0$

$$P_0 e^{i\omega t} = -\lambda \lim_{r\to 0}\left(2\pi rd \cdot A\frac{\partial K_0}{\partial r}\left(\frac{r}{\Lambda}(i+1)\right)\right)\cdot e^{i(\omega t+\phi)} \ . \tag{2.21}$$

Useful properties of $K_n(x)$ are [8]

$$\frac{2n}{x}K_n(x) = K_{n+1}(x) - K_{n-1}(x) \tag{2.22}$$

$$\frac{dK_n(x)}{dx} = -K_{n-1}(x) - \frac{n}{x}K_n(x) \ . \tag{2.23}$$

Therefore, the derivative of the modified Bessel function $K_0(\alpha x)$ equals $-\alpha K_1(\alpha x)$, with $\alpha = (i+1)/\Lambda$. This leads to

$$P_0 = \lambda \cdot 2\pi d \cdot A \cdot \lim_{r\to 0}\big(r\alpha\ K_1(r\alpha)\big)\cdot e^{i(\phi)} \ , \tag{2.24}$$

where the limes approaches 1 according to WolframAlpha [9]. Thus the amplitude is

$$A = \frac{P_0}{2\pi\lambda d} \tag{2.25}$$

Compared to (2.18) there is an additional factor $1/d$ now for thin plates of thickness d. There is no dependence on the heat capacity or the driving frequency and the temperature function is in phase with the driving power as well as for thermally thick bodies.

Extended sources

According to the thermal thickness of a body, again two cases have to be separated following [7]. The areal source introducing oscillating heat $P_0 \cdot e^{i\omega t}$ will in both cases be approximated as infinitely large, respectively with larger extensions than the diffusion length or it will cover one whole side for small bodies.

The first case for thermally thick bodies has already been shown in section 2.2.2 in (2.15) and (2.16)

$$T(z,t) = A \cdot e^{-\frac{z}{\Lambda}} \cdot e^{i(\omega t - \frac{z}{\Lambda} + -\frac{\pi}{4})} , \quad A = \frac{p_0}{\sqrt{\lambda \omega c_p \rho}} . \tag{2.26}$$

The second case for thermally thin bodies uses (2.10)

$$P_0 \cdot e^{i\omega t} = m c_p \frac{dT(t)}{dt} . \tag{2.27}$$

to simply derive the solely time dependent temperature function $T(t)$, as heat conduction can be neglected for a body, heating up with all parts synchronously, leading to

$$T(t) = A e^{i(\omega t + \phi)} . \tag{2.28}$$

The constant amplitude A can be calculated, putting $T(t)$ into the above heat equation and avoiding a complex amplitude

$$\begin{aligned} P_0 \cdot e^{i\omega t} &= A \; m c_p \omega \cdot i e^{i(\omega t + \phi)} \\ P_0 &= A \; m c_p \omega \cdot i e^{i\phi} . \end{aligned}$$

using Eulers equality

$$i \cdot e^{i\phi} = i \cdot [\cos(\phi) + i \sin(\phi)] ,$$

A will only be real, if the exponential part is complex, which leaves out $\phi = \pm\pi/2$ and it will be positive for $\phi = -\pi/2$. So the amplitude results in

$$A = \frac{P_0}{m c_p \omega} . \tag{2.29}$$

The amplitude is frequency dependent, not dependent on heat conductivity and the temperature function shows a phase delay of 90° to the surface heat introduction. The amplitude for high Lock-in frequencies is stronger damped in thermally thin bodies, than in thermally thick ones.

line sources parallel to the surface

This section follows [7] for analysing the behaviour of line heat sources, upon or within a sample, but in an area, parallel to the observed surface: A line heat source for equal power per unit length $p^l(t) = P(t)/l$ over the full length l is a cylindrically symmetric

problem only relying on the distance r.

For thermally thick bodies the same conditions can be applied as for line sources parallel to the z-axis, but seen in different geometry. The temperature function (2.20)

$$T(r,t) = AK_0\left(\frac{r}{\Lambda}(i+1)\right)e^{i(\omega t+\phi)}\ , \tag{2.30}$$

with A from (2.25) holds for buried line sources. For surface line sources it has to be doubled for the transmission in only on half space

$$A = \frac{P_0}{\pi\lambda d} = \frac{p_0^l}{\pi\lambda}\ . \tag{2.31}$$

As for thermally thin point sources, there is no phase delay between the oscillating power $P(t) = P_0 \cdot e^{i\omega t}$ and the temperature expansion $T(r,t)$.

Thermally thin line sources can be adapted from the case of extended heat sources in thermally thick bodies. In thermally thin bodies, the temperature difference through the thickness can be neglected, thus only the lateral heat diffusion contributes. This reduces the heat diffusion equation to a Cartesian one-dimensional problem in x, which was already solved in (2.15) and (2.16) for the depth z

$$T(x,t) = A \cdot e^{-\frac{x}{\Lambda}} \cdot e^{i(\omega t - \frac{x}{\Lambda} + -\frac{\pi}{4})}\ . \tag{2.32}$$

The differences are that heat spreads into $-x$ and $+x$ direction, thereby halving that amplitude and that the power per surface area $p_0 = P_0/A_S$ needs to be transformed to the power per unit length p_0^l by knowing

$$P(t) = P_0 \cdot e^{i\omega t} = p_0 \cdot A_S e^{i\omega t} = p_0^l \cdot l e^{i\omega t}\ . \tag{2.33}$$

The surface area is in this case the cross section area ld as the product of the length of the heat source l and the thickness of the body d leading to $p_0 = p_0^l/d$ and

$$A = \frac{p_0^l}{2d\sqrt{\lambda\omega c_p\rho}}\ . \tag{2.34}$$

As for thermally thick extended heat sources, the temperature extension is delayed by 45° and the amplitude of the temperature function is frequency dependent, in contrary to line sources in thermally thick bodies.

2.2.4 Heat introduction to solar cells

This last section shall show how heat is created and distributed in the case of solar cells (see section 1.1) following [7].

One typical heat source is simple Joul heat by the conduction of electric current through a resistor. For solar cells this can be applied at local shunt points, where the current density J (current per unit area) is multiplied by the specific resistivity ρ, turning into the power density per area p. Joul heat can be neglected for current flow perpendicular to the solar cell (if not through a shunt resistance), as the specific resistivity of silicon solar cells is about $1\,\Omega$m and the typical current density is

$30\,\mathrm{mA/cm^2}$, which leads to only about $0.018\,\mathrm{mW/cm^2}$, which is 0.018% of the incident power density of $100\,\mathrm{mW/cm^2}$.

For extended shunts a different parameter - the so-called sheet resistance ρ_s - is introduced, which defines the specific resistivity per thickness of a layer. In case of solar cells this applies to horizontally current flow in the emitter or contact grid layer. Again, for non-shunt current flows, and a normal current density of the mentioned $30\,\mathrm{mA/cm^2}$ Joul's heat can be neglected.

A main heat source is the internal photoeffect. If the energy $h\nu$ of a photon with frequency ν (see section 2.1.1) is well above the band gap, it will excite a hole and an electron giving both summed up the energy difference between photon and band gap. The excited charge carriers will then free their spare energy above their conduction level as phonons thus heat. This effect mostly heats the p-n junction.

If the quantum efficiency of a solar cell does not equal 1, their are photons that are absorbed by the material itself without generating charge carriers. This holds at least for all photons having less energy than the band gap, being unable to afford the energy for freeing charge carriers.

Further there is the process of Peltier heating. Charge carriers are generated at the pn-junction and move to their corresponding electrode, thereby transferring energy from the pn-junction to the electrodes. This does not effect the heat of the whole cell, but it leads to local cooling at the pn-junction and local heating at the electrodes, resulting in an additional temperature contribution at the electrodes.

Finally not all created pairs of charge carriers do reach the electrical contacts. These, which don't contribute to the electrical current will recombine and most of them in the depletion region. This may lead to an emitted photon or, if not, to dissipated heat. By the radiative recombination the ensemble of electrons and holes looses the excited energy of the two free charge carriers and thereby their mean ensemble energy decreases as the number of electrons and holes stays constant, leading to cooling.

2.3 Dark Lock-in thermography

The basics of thermography, corresponding sensors and heat diffusion were discussed in the above sections. The separate theories will be combined in this section, explaining the technique of Dark Lock-in thermography. First Fourier analysis is reviewed shortly and the Lock-in process is described. The following sections will discuss several conditions, important for the measurement interpretation.

2.3.1 Fourier analysis

Fourier analysis allows a series expansion of a function $f(t)$ in a trigonometric basis called a *Fourier series*:

$$f(t) = \frac{a_0}{2} + \sum_{\ell=1}^{\infty} a_\ell \cos(\ell\omega t) + b_\ell \sin(\ell\omega t) \ , \tag{2.35}$$

where a_ℓ and b_ℓ are constant factors called *Fourier coefficients* and $\omega = 2\pi/T$ is the angular frequency defined by the period length T. An exact solution can be provided, if f(t) has the following properties [15]

- the function is periodic with a period T holding $f(t+T) = f(t)$,
- the function is piecewise continuous within bounded intervals in $0 \leq \mathrm{t} \leq \mathrm{T}$,
- the limit points of this neighboring bounded intervals requires an existing left-hand and right-hand limit (the endpoints 0 and T need only to exist as left-hand or right-hand limit),
- the function contains no discontinuities.

a_ℓ and b_ℓ can be calculated by the corresponding inner product on both sides of (2.35) and further applying of trigonometric transformations with $\ell = 1$ referred to as *basic frequency* and all higher indices as *overtones*:

$$\begin{aligned} a_0 &= \frac{2}{T}\int_0^T f(t)dt \\ a_\ell &= \frac{2}{T}\int_0^T f(t)\cos(\ell\omega t)dt \quad , \quad \forall\ \ell \in \mathbb{N} \\ b_\ell &= \frac{2}{T}\int_0^T f(t)\sin(\ell\omega t)dt \quad , \quad \forall\ \ell \in \mathbb{N} \end{aligned} \tag{2.36}$$

The factor $a_0/2$ represents the mean of the function $f(t)$ within the interval [0,T]. a_0 is here doubled to obtain common formulas and hence needs to be halved in (2.35).

The real valued coefficients a_ℓ and b_ℓ can be converted to an amplitude A_ℓ and a phase shift φ_ℓ by

$$\begin{aligned} A_\ell &= \sqrt{{a_\ell}^2 + {b_\ell}^2} \\ \varphi_\ell &= -\arctan\frac{b_\ell}{a_\ell} \ , \end{aligned} \tag{2.37}$$

For computational approaches a finite sum leads to the approximation

$$f(t) \approx A_0 + \sum_{\ell=1}^{n} A_\ell \cos(\ell\omega t + \varphi_\ell) \tag{2.38}$$

has the variance σ^2 to the exact function [8, Chapter 7.4]

$$\sigma^2 = \frac{1}{T}\int_0^T \left[f(t) - (A_0 + \sum_{\ell=1}^{n} A_\ell \cos(\ell\omega t + \varphi_\ell)) \right]^2 dx \ . \tag{2.39}$$

Fourier analysis, especially through the *Fast Fourier Transformation* (FFT) algorithm, is commonly applied in various topics, as it enables the investigation of frequency components. Some applications are audio conversion, image processing, convolution, signal processing and magnet resonance tomography. In the presented thesis the enhanced FFT algorithm, could not be used, as the amount of data from one measurement exceeded the RAM limits of used PCs.

Example sawtooth

A sawtooth function $f(t) = t$ with $-\pi \leq t \leq \pi$ has the period $T = 2\pi$ leading to $\omega = 1$. As $f(t)$ is odd, meaning $f(-t) = -f(t)$, it follows that all a_ℓ equal zero. Calculating the remaining coefficients b_ℓ according to (2.36) results in

$$f(t) \approx 2\sum_{\ell=1}^{n} \frac{(-1)^{\ell+1}}{\ell} \cos(\ell t - \frac{\pi}{2}) \ , \tag{2.40}$$

as plotted in Fig. 2.6 [15].

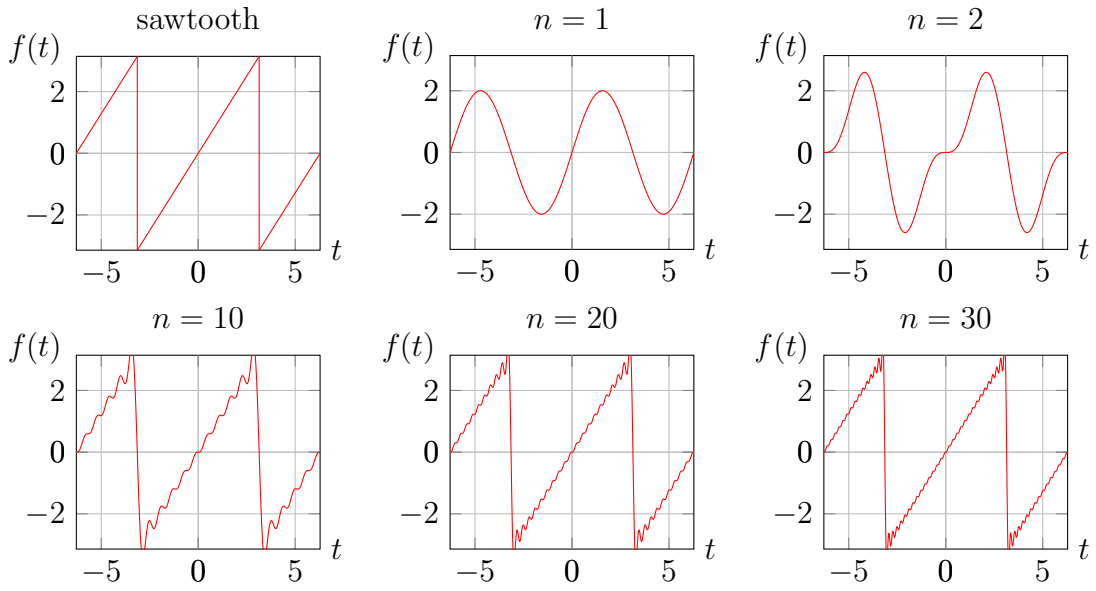

Fig. 2.6: The upper left figure shows the sawtooth function, the others show Fourier series expansions (2.40) of different order.

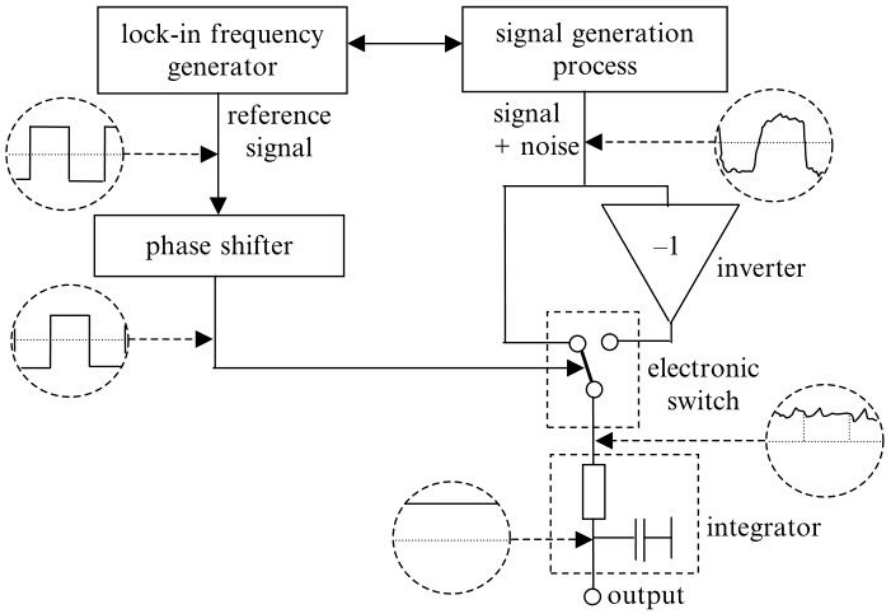

Fig. 2.7: A "signal generation process" generates a modulated signal, which consists of noise. The modulation signal (in this case rectangular) is bypassed and afterwards used for demodulation. In this simple case demodulation happens, as switching between the output and its inverse with the Lock-in frequency. This output signal can then be extracted via low-pass filtering. taken from [7].

2.3.2 Lock-in-Technique

The Lock-in principle is based on signal modulation and demodulation to reduce statistic noise and will be explained following [7].

On can consider a system that reacts to an input signal by an output signal, which is additionally noisy. The Lock-in technique allows to reduce the output noise by a periodically modulation of the input signal with a modulation signal. Often the input signal is already periodical signal and no further modulation needs to be done. For non periodic input signals, easy approaches are pulsing or in general rectifying, e.g. chopped light.

A signal may be generated by an electrical device driven by a current source. If the signal is correlated to the incident current (as the voltage drop on a resistor) an alternating current could be used instead of a constant current to implement the modulation. However, some circuits may be damaged by alternating current. These however could at least be pulsed.

If fed with a modulated input signal, the measurement will return a modulated output signal with statistical noise. Thermal noise can then be cancelled, if the periodic modulation function is known. The frequency of the modulation is called *Lock-in frequency* $f_{\text{Lock-in}}$. An example is shown in Fig. 2.7, which is based on the fact that the non-noise signal is in phase with the modulation signal and that the noise on the positive half wave cancels with the noise on the negative half wave. This is due to the fact that the noise remains statistical after modulation. Hence only symmetric distributed noise noise can be decreased with this technique.

Beside of reducing statistical noise, the Lock-in technique also suppresses constant (non input signal dependent) components and non-correlated additional signals. These might be for instance reflections in an infrared measurement, which lead to additional incident photons, but remain always a constant additive to the alternated temperature of a sample. In contrary, background reflections with integer multiple frequencies as the modulation signal will add systematic errors to the output signal. This could be possible, if measuring at $f_{\text{Lock-in}} = 50\,\text{Hz}$ and gaining reflexions from running electronic devices in the surrounding.

The output signal will be clearer the longer the measurement is performed. This depends relatively on the chosen Lock-in frequency and may cause long measurement times. The advantage of this technique is the reduction of statistical noise and non-modulation-correlated external errors compared to steady-state measurements. Additionally different Lock-in frequencies may have different characteristic effects on the sample an will therefore lead to more specific investigations (see section 2.3.8).

2.3.3 The mathematical approach

The mathematics behind the Lock-in technique is correlated with the Fourier analysis following [7]. The above mentioned output signal can be written as a time dependent function $F(t) = f_0 + f(t)$ with a constant part f_0. The demodulation is done by calculating the integral mean of this output signal with a time dependent *correlation function* $K(t)$. Where the periodic correlation function will be chosen to be zero if solely integrated over integer multiples N of their whole period T. This property will vanish the constant part f_0 and returns the extracted signal S

$$S = \frac{1}{N \cdot T} \int_0^{N \cdot T} F(t)K(t)dt \; . \tag{2.41}$$

Digitized measurements with equi-distant discrete values F_i have to be averaged by a sum instead. Then the correlation function turns into *weighting factors* K_i with M integer steps per period, if time steps are equidistant

$$S = \frac{1}{N \cdot M} \sum_{i=1}^{N \cdot M} F_i K_i \tag{2.42}$$

In general there are two types of of weighting factors used. *Wide-band correlation* uses rectangular-shaped weighting factors being -1 for one half period and +1 for the other while *narrow-band correlation* uses sine and cosine functions.

According to the Nyquist theorem there always need to be at least two samples per period otherwise the extracted signal can not clearly be demodulated. Using narrow-band correlation requires at least four samples per period, as the sampled function with frequency ω will be demodulated with the frequency ω for the basic harmonic. The demodulation is an integral over the product of these leading to $\exp[i\omega t] \cdot \exp[i\omega t] = \exp[i2\omega t]$. Assuming the above mentioned Lock-in frequency $f_{\text{Lock-in}}$ and a sample rate

f_s, the Nyquist theorem leads to the important rule

$$f_{\text{Lock-in}} \leq \frac{f_s}{4} \,. \tag{2.43}$$

This can be adapted for the ℓ-th higher harmonics, resulting in a factor of $2(\ell+1)$ instead of four.

As outlined in section 2.3.1, any periodic function (within some mathematical constraints) can be approximated as a series expansion of trigonometric functions. This expansion can be transformed to a sum of amplitude cosine products for the basic frequency and its overtones with corresponding phase differences and the arithmetic mean (2.38). An in-phase signal would solely consist of cosine parts and phase differences are defined relative to that cosine.

Using the addition theorem

$$\cos(a \pm b) = \cos(a)\cos(b) \mp \sin(a)\sin(b) \tag{2.44}$$

on $f(t)$ for each ℓ in (2.38) will obtain

$$\begin{aligned} f(t) &= A_\ell \cdot \cos(2\pi\ell f_{\text{Lock-in}} t + \varphi_\ell) \\ &= A_\ell \cdot \cos(2\pi\ell f_{\text{Lock-in}} t)\cos(\varphi_\ell) - A_\ell \cdot \sin(2\pi\ell f_{\text{Lock-in}} t)\sin(\varphi_\ell) \,. \end{aligned} \tag{2.45}$$

With the correlation functions

$$\begin{aligned} K_\ell^{0^\circ}(t) &= \cos(2\pi\ell f_{\text{Lock-in}} t) \\ K_\ell^{-90^\circ}(t) &= \sin(2\pi\ell f_{\text{Lock-in}} t) \end{aligned} \tag{2.46}$$

the demodulation (2.41) - doubled to be consistent with the formulas presented in (2.36) - of the output signal $F(t)$ will return the Fourier coefficients

$$\mathcal{C}_\ell = \frac{A_\ell}{2} \cdot \cos\varphi_\ell \quad \text{and} \quad \mathcal{S}_\ell = -\frac{A_\ell}{2} \cdot \sin\varphi_\ell \,. \tag{2.47}$$

As the phase refers to the cosine, the sine component is 90° delayed. $\mathcal{C}_\ell = S_\ell^{0^\circ}$ is the so called *in-phase signal* and $\mathcal{S}_\ell = S_\ell^{-90^\circ}$ is refered to as *quadrature signal*. The amplitude and phase can then be calculated by

$$\begin{aligned} A_\ell &= \sqrt{\mathcal{C}_\ell^2 + \mathcal{S}_\ell^2} \\ \varphi_\ell &= -\arctan\left(\frac{\mathcal{S}_\ell}{\mathcal{C}_\ell}\right) \end{aligned} \tag{2.48}$$

in agreement with (2.37).

In the discrete, equidistant case, the weighting factors are

$$\begin{aligned} K_{\ell,i}^{0^\circ} &= \cos\left(2\pi\ell f_{\text{Lock-in}}(i-1)\right) \\ K_{\ell,i}^{-90^\circ} &= \sin\left(2\pi\ell f_{\text{Lock-in}}(i-1)\right) \end{aligned} \tag{2.49}$$

where ℓ is the overtone index and i is the frame number. The $(i-1)$ is a correcting

shift for the sum in (2.42) starting at $i = 1$. The discrete demodulation also needs to be multiplied by a factor of two.

Depending on the physical processes leading to the sample response, the output signal will have a phase delay to the modulation signal. If this delay is 0° or 90°, then the in-phase respectively the quadrature signal already shows the extracted signal. If not, the signal $S_\ell^{\varphi'}$ of an arbitrary phase shift φ' can be calculated by

$$S_\ell^{\varphi'} = A_\ell \cdot \cos(\varphi' - \varphi_\ell) \tag{2.50}$$

for all overtones. Typically, the basic frequency carries the most important information. In many cases it depends on the modulation frequency, whether the output signal just consists of basic frequency components or also shows its overtones.

2.3.4 Fourier analysis of a camera based measurement

Following [7] a camera based system allows to measure a series of images in a non-contacting way. Each image is called a *frame* and consists of an array of pixels. These frames represent a two-dimensional space (x, y) and their time series represents a third dimension of time t thereby forming a three-dimensional measurement. Each pixel $p(x, y)$ can thus be treated as having an independent time expansion $p(x, y, t)$.

Camera based systems return frames, where each pixel contains an intensity or some transformed quantity as the temperature of an object emitting IR-radiation (see section 2.1.1). A camera based Lock-in measurement leads to a series of frames, where each pixel $p(x, y, t)$ represents a periodic output signal with additional noise and other possible corruptions.

The frequency $f_{\text{Lock-in}}$ of the modulation is assumed to be known and the frame rate f_s needs to be set according to (2.43). In the easiest case, the modulation and the frame rate of the camera can be electronically triggered via a PC and thereby synchronized. This would cancel any phase differences between the in-phase signal $\mathcal{C}_\ell$ and the modulation signal. Otherwise an asynchronous measurement is performed, leading to an additional global constant phase shift for all pixels.

The pixel series $p(x, y, t)$ can be demodulated by performing Fourier analysis as introduced in section 2.3.1 and 2.3.3. S_{mean} is simply the arithmetic mean for all times

$$S_{\text{mean}}(x, y) = \frac{2}{N \cdot T_{\text{Lock-in}}} \sum_{t=0}^{t=N \cdot T_{\text{Lock-in}}} p(x, y, t) \; . \tag{2.51}$$

Where $T_{\text{Lock-in}}$ is the Lock-in period length $T_{\text{Lock-in}} = 1/f_{\text{Lock-in}}$. $\mathcal{C}_\ell$ and $\mathcal{S}_\ell$ need to be calculated by summing over all times and additionally multiplying $p(x, y, t)$ with the corresponding trigonometric function at each point in time

$$\begin{aligned} \mathcal{C}_\ell(x, y) &= \frac{2}{N \cdot T_{\text{Lock-in}}} \sum_{t=0}^{t=N \cdot T_{\text{Lock-in}}} p(x, y, t) \cdot \cos(2\pi \ell f_{\text{Lock-in}} t) \cdot \Delta t \\ \mathcal{S}_\ell(x, y) &= \frac{2}{N \cdot T_{\text{Lock-in}}} \sum_{t=0}^{t=N \cdot T_{\text{Lock-in}}} p(x, y, t) \cdot \sin(2\pi \ell f_{\text{Lock-in}} t) \cdot \Delta t \end{aligned} \tag{2.52}$$

This formula can be simplified, if all time steps are equidistant and the Lock-in time is an integer multiple of a time step Δt. Then the time step can be cancelled and the Lock-in period length is denoted in frames instead of seconds. Thus all t being integers counting up from 0 to NM where N is the number of periods and $M = f_s/f_{\text{Lock-in}}$ is the number of frames in one period.

If the frame rate is not constant in time, but the time for each frame is known, it is more accurate to use the above formulas as they are, with

$$\Delta t = \begin{cases} \frac{t_1 - t_0}{2} & \text{for } t_0 \\ \frac{t_{i+1} - t_{i-1}}{2} & \text{for } 0 < i < NM \\ \frac{t_{NM} - t_{NM-1}}{2} & \text{for } t_{NM} = N \cdot T_{\text{Lock-in}} \end{cases} . \tag{2.53}$$

As a result there will be $2\ell+1$ images: The *mean image* $S_{\text{mean}}(x, y)$, in-phase images $\mathcal{C}_\ell(x, y)$, and quadrature images $\mathcal{S}_\ell(x, y)$ consisting of the corresponding pixels Fourier analysis. These can be transformed to amplitude and phase by using (2.48), where the phase may contain a phase shift to the modulation signal, if the measurement setup is not synchronized.

2.3.5 Rectangular heating

The derivations in section 2.2.3 refer to a harmonic driving current. The differences in using a rectangular heat introduction will be discussed in this section following [7].

A rectangular current with period T can be described by a rectangular power introduction

$$P(t) = \begin{cases} P_0 & 0 \leq t < \frac{T}{2} \\ 0 & \frac{T}{2} \leq t < T \end{cases} , \tag{2.54}$$

where the definition of the discontinuity point depends on the definition of the Heaviside function and may in some cases be $P_0/2$. The Fourier series of $P(t)$ is:

$$P(t) = \frac{P_0}{2} + \frac{2P_0}{\pi} \cdot \sum_{j=0}^{\infty} \frac{1}{2j+1} \sin\big((2j+1)\omega t\big) \tag{2.55}$$

which can be easily calculated with the formulas in section 2.3.1, knowing that all symmetric parts (cosine) are zero and that all odd frequencies lead to zero by $1 - \cos(j\pi)$. This means that only odd sine components are added to the mean value with the first one being the basic harmonic.

First of all the introduced heat $P_0 T/2$ of the rectangular current separates into a constant heating, the basic harmonic and higher harmonics. Hence, the basic harmonic is driven with less energy than introduced. Putting the same heat into a comparable sinusoidal heating with a mean value equal to the amplitude, generating an all time

positive wave will lead to

$$P_0 \cdot T/2 = \int_0^T (A + A\sin(\omega t))\, dt = A \cdot T \tag{2.56}$$

as the integral of a sine over a full period vanishes, the amplitude of $P_0/2$ would be introduced. The same result could be obtained by a geometrical approach, when adding the left over area of the second half period to the area covered in the first half period to form a rectangular heating.

The rectangular introduced basic harmonic has an amplitude $A_{\text{rect}} = 2P_0/\pi$ compared to the sinusoidal introduced one with an amplitude $A_{\text{sin}} = P_0/2$. Therefore the energy lost in higher harmonics results in

$$\int_{t=0}^{T} (P_{\text{rect}}(t) - P_{\text{sin}}(t))\, dt \tag{2.57}$$

As the amplitude of the rectangular sinus is larger than the mean value, the basic harmonic component will be negative in some part of the second half wave. Shifting the power axis in the integral by adding the difference $d = 2P_0/\pi - P_0/2$ will obtain $(P_0 + d)T/2$. To correct the shifting the area $d \cdot T$ needs to be subtracted to get the solution of the first part of the integral $(P_0 - d)T/2$ and the second part is still $P_0T/2$. This obtains the energy difference relative to the complete introduced energy $P_0T/2$

$$\left(\frac{2P_0}{\pi} - \frac{P_0}{2}\right) \cdot \frac{T}{2} = \left(\frac{4-\pi}{2\pi}\right) \frac{P_0T}{2} \approx 0.1366 \frac{P_0T}{2};. \tag{2.58}$$

This results in about 13.66% lost signal to the basic harmonic part, due to the fact, that the solutions of (2.13) can be super positioned.

Additional errors can be introduced by the higher harmonics, if the sample rate is close to the Lock-in frequency. For sample rates much higher then the Lock-in frequency the weighting factors (2.49) approach the sine and cosine function and the identity

$$\int_0^{2\pi} \sin(\omega t)\sin(n\omega t + \varphi)dt = \int_0^{2\pi} \cos(\omega t)\sin(n\omega t + \varphi)dt = 0\ , n = 3, 5, 7, \ldots \tag{2.59}$$

cancels all higher harmonic frequency parts, returning the same result as a sinusoidal heat introduction.

These introduced errors also depend on the type of the heat source. Extended heat sources are least critical, as their amplitude decreases with $1/\sqrt{f_{\text{Lock-in}}}$ or $1/f_{\text{Lock-in}}$ depending on their thermal thickness, as shown in (2.29) for thermal thin and (2.16) for thermal thick materials. Hence higher harmonics are damped more with rising order as $f_\ell = \ell f_{\text{Lock-in}}$. Further, the higher harmonics in (2.55) have a lower power amplitude compared to the basic harmonic's, as they are proportional to $\ell = (2j + 1)$. Together this leads to a 9 times lower temperature response for the first higher harmonic in a thermally thin body compared to the basic harmonic.

Point heat sources are more critical, as their temperature function is independent of the Lock-in frequency for all thermal thicknesses (see section 2.2.3), there will be

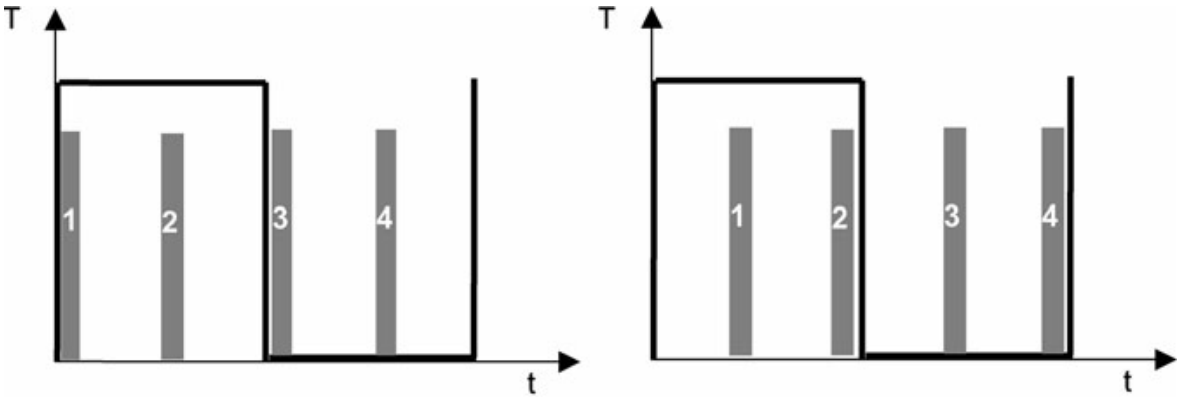

Fig. 2.8: The thick line is the rectangular temperature function for a point heat source. Four frames are taken within one heating period. The frames integration time is indicated by the grey area, which is shown thicker for better illustration and would actually just be a thin line. The shutter is closed outside the grey area. In both cases the camera will show the same response, but there is a certain phase difference of about 90° between the left and the right graph. The resulting demodulated signal will have a phase shift of 45° in both cases and for all phase shifts in between [7].

a rectangular temperature function in source position. This results in an important influence of the integration time of the digital system (e.g. the integration time of a camera compared to the time with closed shutter). Fig. 2.8 illustrates that problem in the most critical case of $f_s = 4f_{\text{Lock-in}}$. The phase shift between the two cases is about 90°, but the demodulation will lead to a phase shift of 45° as the camera response in both cases is completely the same. Only if the integration time meets the discontinuity point, the phase shift will be more accurate.

In the mentioned example of a camera based measurement, with a frame rate being 4 times the Lock-in frequency, a phase error of $\sigma_\varphi = \pm 45°$ will be obtained. This error drops with the number of frames per period, as it solely depends of the phase distance between two frames. If the number of frames per Period is M, then a simple approximation of this error σ_φ can be calculated in degrees as

$$\sigma_\varphi = \frac{360}{2M} \tag{2.60}$$

So for $M = 150$ it will be $\pm 1.2°$. The more accurate calculation depends on the frame integration time t_{int} relying on a factor of $1/(4t_{\text{int}} f_{\text{Lock-in}})$.

The described errors are dependent on the multiple of the sample rate relative to the Lock-in frequency. For too low sample rates the errors need to be considered. For more than 10 samples per Lock-in period, the errors are usually very small and can therefore be neglected.

Further, the different damping of each frequency part leads to different curve shapes in the distance to a point source. The shape of the rectangular heating is kept in source position $r = 0$ and is smoothed the farther the distance. Fig. 2.9 shows this effect as a function of diffusion lengths from 0 to 2Λ simulated up to the 99th harmonic. The smoothing turns the rectangular shape of the source position to an exponential wave very close to the source and this smooths out to a sine for longer distances.

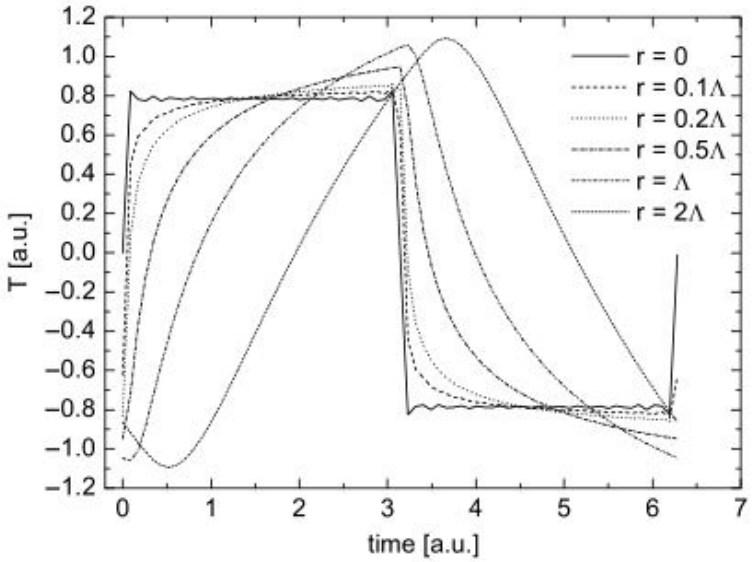

Fig. 2.9: One period of the temperature function for a point source at $r = 0$ is shown from the source from $r = 0$ to $r = 2\Lambda$, where Λ is the diffusion length. The simulation goes up to the 99th harmonic (refering to (2.55)). In farther distances, the rectangular shape smooths and an increasing phase shift is introduced. For better comparison the amplitudes are scaled to their basic harmonics. Taken from [7].

2.3.6 Error propagation

Error propagation allows to estimate the relative standard deviation σ_f of a function $f(x, y)$ by knowing the relative standard deviation σ_x,σ_y of its independent variables x, y by partial differentiation

$$\sigma_f = \sqrt{\left(\frac{\partial f}{\partial x} \cdot \sigma_x\right)^2 + \left(\frac{\partial f}{\partial y} \cdot \sigma_y\right)^2} \tag{2.61}$$

Calculating the amplitude from the Lock-in output signals

The following derivation considers some known error in the Lock-in output signals $\mathcal{C}$ and $\mathcal{S}$. These errors are $\sigma_\mathcal{C}$ and $\sigma_\mathcal{S}$. The amplitude follows (2.48). The partial derivations of $A(\mathcal{C}, \mathcal{S})$ are

$$\begin{aligned} \frac{\partial A}{\partial \mathcal{C}} &= \frac{1}{2}\frac{1}{\sqrt{\mathcal{C}^2 + \mathcal{S}^2}} \cdot 2\mathcal{C} = \frac{\mathcal{C}}{\sqrt{\mathcal{C}^2 + \mathcal{S}^2}} \\ \frac{\partial A}{\partial \mathcal{S}} &= \frac{1}{2}\frac{1}{\sqrt{\mathcal{C}^2 + \mathcal{S}^2}} \cdot 2\mathcal{S} = \frac{\mathcal{S}}{\sqrt{\mathcal{C}^2 + \mathcal{S}^2}} \,. \end{aligned} \tag{2.62}$$

Thus the error in the amplitude is

$$\sigma_A = \sqrt{\frac{\mathcal{C}^2}{\mathcal{C}^2 + \mathcal{S}^2} \cdot \sigma_\mathcal{C}^2 + \frac{\mathcal{S}^2}{\mathcal{C}^2 + \mathcal{S}^2} \cdot \sigma_\mathcal{S}^2} = \sqrt{\frac{\mathcal{C}^2\sigma_\mathcal{C}^2 + \mathcal{S}^2\sigma_\mathcal{S}^2}{\mathcal{C}^2 + \mathcal{S}^2}} \,. \tag{2.63}$$

If $\sigma_{\mathcal{C}} = \sigma_{\mathcal{S}}$ it follows

$$\sigma_A = \sigma_{\mathcal{C}} \ . \tag{2.64}$$

Calculating the phase from the Lock-in output signals

The following derivation considers some known error in the Lock-in output signals $\mathcal{C}$ and $\mathcal{S}$. These errors are $\sigma_{\mathcal{C}}$ and $\sigma_{\mathcal{S}}$. The phase follows (2.48). The partial derivations of $\varphi(\mathcal{C}, \mathcal{S})$ are

$$\begin{aligned} \frac{\partial \varphi}{\partial \mathcal{C}} &= -\frac{1}{1+\left(\frac{\mathcal{S}}{\mathcal{C}}\right)^2} \cdot \frac{-\mathcal{S}}{\mathcal{C}^2} = \frac{\mathcal{S}}{\mathcal{C}^2+\mathcal{S}^2} \\ \frac{\partial \varphi}{\partial \mathcal{S}} &= -\frac{1}{1+\left(\frac{\mathcal{S}}{\mathcal{C}}\right)^2} \cdot \frac{1}{\mathcal{C}} = \frac{\mathcal{C}}{\mathcal{C}^2+\mathcal{S}^2} \ . \end{aligned} \tag{2.65}$$

Thus the error in the phase is

$$\sigma_\varphi = \frac{\sqrt{\mathcal{S}^2\sigma_{\mathcal{C}}^2 + \mathcal{C}^2\sigma_{\mathcal{S}}^2}}{\mathcal{C}^2+\mathcal{S}^2} \ . \tag{2.66}$$

If $\sigma_{\mathcal{C}} = \sigma_{\mathcal{S}}$ it follows

$$\sigma_\varphi = \frac{\sigma_{\mathcal{C}}}{\sqrt{\mathcal{C}^2+\mathcal{S}^2}} = \frac{\sigma_{\mathcal{C}}}{A} \ . \tag{2.67}$$

2.3.7 Noise characteristics

Dark Lock-in thermography is a camera based measurement setup and is applied to e.g. photovoltaic modules in the dark to suppress distracting effects of varying photon intensity and the inner photoeffect to control IR-emission only via an applied a.c. current. This section shows the theoretical approach to estimate the noise and shows how the noise is being measured from the gathered data.

Theoretical approach

The theoretical approach is following [7]. In Dark Lock-in thermography an object is measured with an IR-camera. This camera can be characterized by the NETD (see section 2.1.4), the noise equivalent temperature difference, based on the measurement of one Pixel over $k >> 1$ successive measurements, with the arithmetic mean $\bar{p}(x, y)$. The standard deviation of the camera noise is then

$$\sigma_{\text{cam}}(x,y) = \frac{1}{k}\sqrt{\sum_{i=1}^{k}(p(x,y,t_i) - \bar{p}(x,y))^2} = \frac{\text{NETD}}{c} \ . \tag{2.68}$$

where c is the camera scaling factor. If σ_{cam} is not measured in digits but in K then $c = 1$. As a camera consists of many pixels, this value may vary across the image, but this will not be considered further.

For constant frame rate and equidistant temperature steps, Δt can be set to 1 in (2.52). Further $T_{\text{Lock-in}}$ can be written as M frames per period, $f_{\text{Lock-in}}$ as $1/M$ and t can be written as j in terms of (2.49) with j counted inside each period therefore generating a double sum. N is still the number of periods of investigation and ℓ will be set to one to consider only the basic frequency here. The pixel data $p(x, y, t)$ will rewritten to $p_i(x, y)$ for the i-th frame, which results in

$$\begin{aligned} \mathcal{C}(x,y) &= \frac{2}{NM} \sum_{i=1}^{N \cdot M} \cos\left(\frac{2\pi(i-1)}{M}\right) p_i(x,y) \\ \mathcal{S}(x,y) &= \frac{2}{NM} \sum_{i=1}^{N \cdot M} \sin\left(\frac{2\pi(i-1)}{M}\right) p_i(x,y) \ . \end{aligned} \tag{2.69}$$

Next each pixel $p_i(x, y)$ can be seen as a sum of a constant mean part $\bar{p}(x, y)$, a periodical varying part $\Delta p_i(x, y)$ relative to the constant part and a statistical noise part $p_i^N(x, y)$ relative to both others.

$$p_i(x,y) = \bar{p}(x,y) + \Delta p_i(x,y) + p_i^N(x,y) \tag{2.70}$$

This equation requires that the mean value $\bar{p}(x, y)$ does not vary over time. So the system is considered to have a stable mean temperature and the heating phase is passed.

Evaluating the measurement results in

$$\begin{aligned} \mathcal{C}(x,y) &= 0 + \bar{\mathcal{C}}(x,y) + N^{0^\circ}(x,y) \\ \mathcal{S}(x,y) &= 0 + \bar{\mathcal{S}}(x,y) + N^{-90^\circ}(x,y) \ . \end{aligned} \tag{2.71}$$

The constant part vanishes, as the full integral over a sine or cosine is zero, $\bar{\mathcal{C}}(x, y)$ and $\bar{\mathcal{S}}(x, y)$ are the desired temperature variation signals and $N^{0^\circ}(x, y)$ and $N^{-90^\circ}(x, y)$ are the signals noise

$$\begin{aligned} N^{0^\circ}(x,y) &= \frac{2}{NM} \sum_{i=1}^{N \cdot M} \cos\left(\frac{2\pi(i-1)}{M}\right) p_i^N(x,y) \\ N^{-90^\circ}(x,y) &= \frac{2}{NM} \sum_{i=1}^{N \cdot M} \sin\left(\frac{2\pi(i-1)}{M}\right) p_i^N(x,y) \ . \end{aligned} \tag{2.72}$$

The standard deviations of the above are the standard deviations $\sigma_{\mathcal{C}}$ and $\sigma_{\mathcal{S}}$ of the signals $\mathcal{C}$ and $\mathcal{S}$. It is dependent on the noise in each pixel $p_i^N(x, y)$ which has the standard deviation σ_{cam} according to (2.68). Using the statement that the variance of

a sum over k different pixels equals the sum of the variances of each pixel results in

$$\begin{aligned}
\sigma_{\mathcal{C}}^2 &= \frac{1}{k}\sum_{j=1}^{k}\left(N^{0^\circ}(x_j,y_j)\right)^2 = \sum_{i=1}^{N\cdot M}\left(\frac{2}{NM}\cos\left(\frac{2\pi(i-1)}{M}\right)\sigma_{\text{cam}}\right)^2 \\
&= \left(\frac{2\sigma_{\text{cam}}}{NM}\right)^2 \cdot \frac{NM}{2} = \frac{2\sigma_{\text{cam}}^2}{NM} \\
\sigma_{\mathcal{S}}^2 &= \frac{1}{k}\sum_{j=1}^{k}\left(N^{-90^\circ}(x_j,y_j)\right)^2 = \sum_{i=1}^{N\cdot M}\left(\frac{2}{NM}\sin\left(\frac{2\pi(i-1)}{M}\right)\sigma_{\text{cam}}\right)^2 \\
&= \left(\frac{2\sigma_{\text{cam}}}{NM}\right)^2 \cdot \frac{NM}{2} = \frac{2\sigma_{\text{cam}}^2}{NM}\,,
\end{aligned} \tag{2.73}$$

as the sum over the square of cosine or sine returns $M/2$ in each of the N periods. Thus the standard deviations of the signals are equal to

$$\sigma_{\mathcal{C}} = \sigma_{\mathcal{S}} = \sigma_{\text{cam}}\sqrt{\frac{2}{NM}}\,. \tag{2.74}$$

This results show, that the signal gets less noisy the more frames are recorded. As the deviation shows, it is important to consider only full periods for the signals $\mathcal{C}$ and $\mathcal{S}$. It further does not matter, if a lot of periods are measured or only a few periods with a lot of frames per period. At the end, only the amount of frames contributing the Fourier analysis process defines the quantity of the noise, as long as for rectangular heating more than ten frames per Lock-in period are measured according to section 2.3.5.

Pixel noise

Each pixel's time series has a corresponding approximated Fourier series (2.38) with an error depending on the number of overtones chosen. The *pixel's noise* has been calculated using the standard deviation of these signals (2.39).

If the temperature function is not truly periodic, because of e.g. temperature instabilities in the testing environment, then the period start and end point may not be equal. This introduces further noise to the measurement. As does the Fourier approximation with only the basic frequency (see section 2.3.5). For increasing amount of overtones, long measurements and no temperature instabilities the pixel noise approaches the camera noise σ_{cam}.

Image noise

The *image noise* was an attempt in this thesis to have a quantitative comparison, between different images with strong local variations. The noise definition considers the deviation of one pixel to its average surrounding.

One can consider only the two horizontally and two vertically neighbours, called the *direct neighbours* or also the four diagonal neighbours, which is then a square around a pixel or even farther squares of neighbours. The amount of considered neighbours

can be described by a radius around a center pixel where the biggest square's edge has $(2r + 1)$ pixels.

With a local definition of noise, edges in the image are regarded as noise as well, but in case of a Dark Lock-in measurement images of the same object are compared. Therefore all compared images have the same contours. Furthermore, contours should generally expand through a few pixels and thus have smooth transitions to some neighbours as least.

The method is based on the convolution of an image with a gaussian kernel. The image noise is then calculated as the standard deviation between the image and its blurred version.

The blurred image $p_{\text{blur}}(x, y)$ represents a weighted mean image, based on surrounding of each pixel. A kernel $m(\xi, \eta)$ is created with a Gaussian distribution

$$m(\xi, \eta) = \frac{1}{\sigma\sqrt{2\pi}} e^{-\frac{\xi^2+\eta^2}{\sigma^2}} \tag{2.75}$$

spreading across a 17x17 square. The standard deviation σ is chosen as two pixels, forming a kernel that covers nearly 100% of the Gaussian distribution.

Moving this kernel across all pixels $p(x, y)$ of an image results in the blurred image

$$p_{\text{blur}}(x, y) = \sum_{\xi=-8}^{8} \sum_{\eta=-8}^{8} p(x + \xi, y + \eta) m(\xi, \eta) \ . \tag{2.76}$$

Finally the standard deviation of the image $p(x, y)$ and the blurred image $p_{\text{blur}}(x, y)$ is calculated within a selectable rectangular range $[(x_{\min}, y_{\min}) \ , \ (x_{\max}, y_{\max})]$ by

$$\sigma^2_{\text{img}} = \frac{1}{(x_{\max} - x_{\min} + 1)(y_{\max} - y_{\min} + 1)} \sum_{x=x_{\min}}^{x_{\max}} \sum_{y=y_{\min}}^{y_{\max}} (p(x, y) - p_{\text{blur}}(x, y))^2 \tag{2.77}$$

Unfortunately, the algorithm fails on the investigations in section 3.4, it was not compatible with the qualitative impression of the presented images. Further tests on different sample images and various details may reveal the current problems and improve this method. It was revealed that phase image need to be shifted before applying this method, otherwise the phase overflow will corrupt the algorithm.

2.3.8 Heat source detection

As outlined in section 2.2.3 different heat sources show different amplitude and phase dependencies on the Lock-in frequency and the material parameters. Their response further varies with the thermal thickness of the material and may also be delayed in phase. Tab. 2.3 summarizes the above results. Following [7] the different images' properties will be outlined.

In Dark Lock-in thermography there are four important images: The in-phase $\mathcal{C}(x, y)$, the quadrature $\mathcal{S}(x, y)$, the amplitude $A(x, y)$ and the phase image $\phi(x, y)$, where the signal S is the temperature T. Sometimes a fifth image is the $\mathcal{C}/\mathcal{S}$ image, but this one is only interesting for microscopic investigation and therefore ignored here.

	thermal thin		thermal thick	
Heat source	$T(r,t)$	$\Delta\varphi$	$T(r,t)$	$\Delta\varphi$
Point	$\frac{P_0}{2\pi\lambda d} K_0\left(\frac{r}{\Lambda}(i+1)\right) e^{i\omega t}$	$0°$	$\frac{P_0}{4\pi\lambda \cdot r} \cdot e^{-\frac{r}{\Lambda}} \cdot e^{i(\omega t - \frac{r}{\Lambda})}$	$0°$
Extended	$\frac{P_0}{mc_p\omega} \cdot e^{i(\omega t - \frac{\pi}{2})}$	$-90°$	$\frac{p_0}{\sqrt{\lambda\omega c_p \rho}} \cdot e^{-\frac{z}{\Lambda}} \cdot e^{i(\omega t - \frac{z}{\Lambda} - \frac{\pi}{4})}$	$-45°$
Line	$\frac{p_0^l}{2d\sqrt{\lambda\omega c_p \rho}} \cdot e^{-\frac{x}{\Lambda}} \cdot e^{i(\omega t - \frac{x}{\Lambda} - \frac{\pi}{4})}$	$-45°$	$\frac{p_0^l}{\pi\lambda} K_0\left(\frac{r}{\Lambda}(i+1)\right) e^{i\omega t}$	$0°$

Tab. 2.3: The temperature functions for different heat sources derived in section 2.2.3 are shown. $T(r,t)$ needs to be replaced by $T(x,t)$ for thermal thin line sources and by $T(z,t)$ for thermal thick extended sources.

Amplitude image

The amplitude image is the easiest image to understand, as it directly shows the amplitudes and is always positive. In contrary to the phase image the amplitude image $A(x,y)$ can be used to show temperature differences between the heat sources. It carries the information about heat source intensities.

For point heat sources, it shows a tight maximum in source position, but not as tight, as the in-phase image (compare to Fig. 2.11).

In the amplitude and quadrature image, point sources are less blurred for higher Lock-in frequencies, due to lower diffusion lengths and weaker damping in the term $\exp(-r/\Lambda)$. The blur around a point source is called *halo*.

Extended heat sources are shown in both thermally thin and thick media. Comparing to Tab. 2.3 shows that the amplitude is dependent on $1/f_{\text{Lock-in}}$ respectively $1/\sqrt{f_{\text{Lock-in}}}$. Therefore, the intensity decreases with larger Lock-in frequencies.

As point heat sources have a better spacial resolution for high Lock-in frequencies, where the extended sources are weak, extended heat sources have a higher amplitude for low Lock-in frequencies. A high Lock-in frequency measurement and a low Lock-in frequency measurement has to be performed to show both effects.

Phase image

The phase image $\phi(x,y)$ is the only image not effected by the surface emissivity. Every point source is shown with same brightness, as they all are in-phase with each other. It can be used to see weaker heat sources in the surrounding of strong ones, as they would be overlapped by the stronger heat sources in the amplitude image. If samples show a very detailed surface with a lot of contours, this image may be the best to use, e.g. for ICs.

Around all heat source, the phase image degrades linearly, and therefore does not show a sharp peak for point heat sources. The spatial resolution is defined by the diffusion length as shown in Fig. 2.10.

This image may produce locally noisy pictures in areas without any heat source or thermal connection to heat sources. The signal varies arbitrarily therefore any pixel there may show different phases, which does not look smooth in coloured pictures.

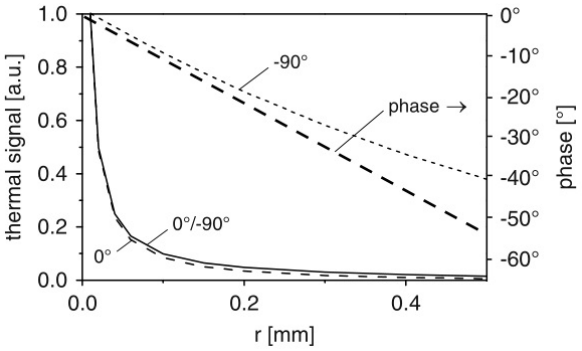

Fig. 2.10: The in-phase, quadrature and phase signal are shown around a point source at $r = 0$. The r-range is chosen up to the diffusion length of 0.58 mm at a Lock-in frequency of 88 Hz. Therefore the graph shows the spacial resolution of the phase image to be at around the diffusion length. All signals, but the phase are scaled to meet at a distance of 10 μm. The graph is taken from [7].

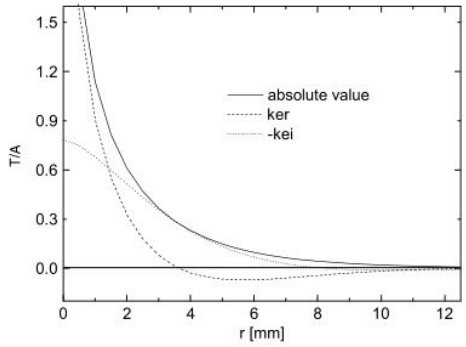

Fig. 2.11: The Kelvin functions $ker(x)$ and $kei(x)$ are plotted for a diffusion length of 3 mm, taken from [7].

In-phase image

The in-phase $\mathcal{C}(x, y)$ resolves point heat sources the most localized. Point sources, in thin media, are in this image described by the *ker*-function, which shows a tighter maximum at $r = 0$ then the amplitude image in Fig. 2.11, as it can be approached by $\ln(x/2)$ for small distances. The *ker*-function turns negative, shortly beyond the diffusion length.

Extended heat sources, extending more than the diffusion length are not visible for thermally thin samples. In thermally thick samples it shows a resolves extended heat sources, if the camera resolution is below the thermal diffusion length.

Quadrature image

The quadrature image $\mathcal{S}(x, y)$, in contrary to the in-phase image, is described by the *kei*-function for point sources in thermally thin media. Compared to the *ker*-function in Fig. 2.11 the *kei*-function has a finite maximum in source position and spreads quite far. Point heat sources are blurred up to 2Λ and have a pronounced halo around them (see section 3.3.6). It shows extended heat sources quite well, due to their phase shift.

3 Measurement

Various measurements have been performed to find the best parameters for various module technologies. The found characterizations are presented after the explanation for the setup and the software tool. Finally a section about the results discusses one module of each measured technology, comparing to other characterization methods and showing investigated module faults.

3.1 Measurement setup

Dark Lock-in thermography measurements, see section 2.3, are performed with a setup shown in Fig. 3.1. To isolate the measurement from all the light sources in the control room, a wall separates the user, inside the control room from the actual measurement part.

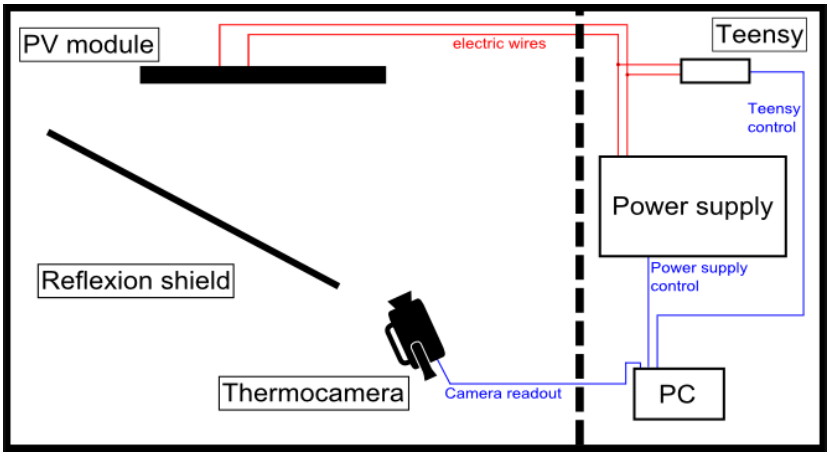

Fig. 3.1: The setup is shown from above. A dashed line indicates a wall that separates the control room on the right. The room part is shaded when measurements are performed.

PV modules are mounted to a wall by aluminium profiles (see Fig. 3.2) and are connected to a power supply. To avoid self reflection (see section 2.1.5), the thermocamera is inclined to the module. To avoid reflected environmental effects, a reflexion shield made of cardboard and styrofoam is positioned in certain distance to the module.

An Infratec VarioCAM HD thermocamera is used, shown in Fig. 3.2. It uses an uncooled microbolometer FPA (see section 2.1.3) and supports a maximum frame rate of 30 frames per second (FPS) at an image resolution of 1024x768. The spectral range spreads from 7.5 to 14 μm measuring temperatures from -40 to 1200 °C. The NEDT is 0.05 K using a 16-bit ADC [28].

The camera can not be triggered without additional equipment and is connected to the PC with a network cable for readout. This connection enables the maximum

Fig. 3.2: PV modules are mounted to the wall by using aluminium profiles. The reflexion on the module shows the reflexion shield. The thermocamera is shown on the right (see text).

frequency of 30 FPS, SD card storage would only allow 10 FPS.

Camera recording is performed using InfraTec's Software IRBIS3. This software offers acquisition at 1, 2, 3, 6, 7.5, 10, 15 and 30 fps. For better comparison, measurements for one module are always taken at 450 frames per Lock-in period through glass and for a-Si and c-Si from the back side at 150 frames per period.

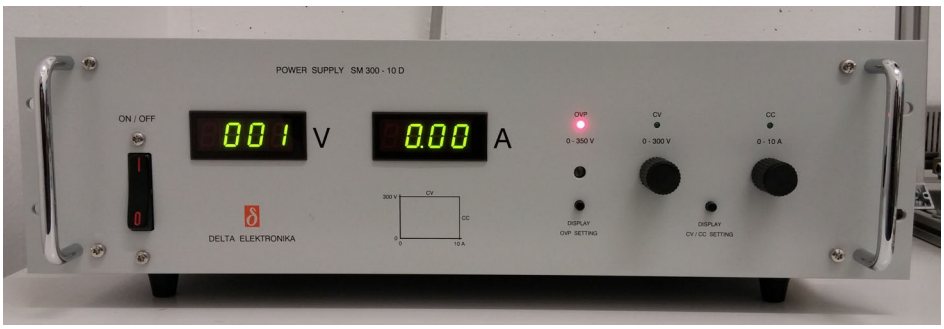

Fig. 3.3: The DELTA ELECTRONICA power supply allows to limit current and voltage, indicating the limitation with LEDs. It is controlled via serial communication.

A Lock-in frequency is set by serial communication to a microcontroller PCB ("Teensyboard") [38] running Arduino based software [4]. The short program controls the altering of the module current via a measurement control circuit explained in section 3.1.1 and shown in Fig. 3.4. It is short cutting the module every half Lock-in period, providing rectangular heating pulses to it, as outlined in section 2.3.5. By using 450 respectively 150 frames per period the measurement exceeds the minimum of ten frames per period, where errors from the pulsed heating can be neglected.

The power supply can be limited in current and voltage via the PC. Fig. 3.3 shows an image of the used DELTA ELECTRONICA. Limits are chosen to operate the module below its the short circuit current (see section 1.1.3).

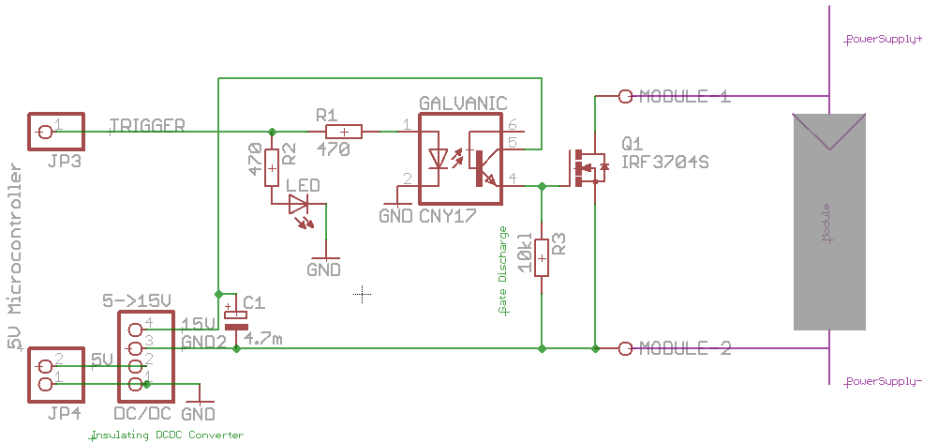

Fig. 3.4: The measurement control circuit is shown in the middle. On the right is the PV module and on the left are the connection pins to the Teensy board.

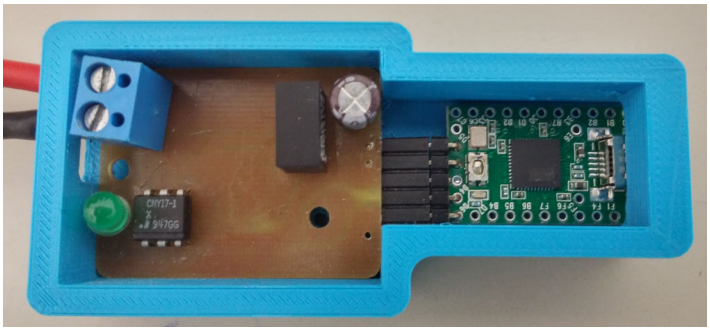

Fig. 3.5: The green Teensy PCB on the right is connected to the measurement control circuit board on the left. A green LED in the lower left indicates the current state. The red and black cable on the left are the connections to the module, the MOSFET is on the bottom side. Via micro USB the teensy can be connected to a PC.

3.1.1 Measurement control circuit

As outlined in section 2.3, the heating power of the PV module has to be modulated. This is done by a MOSFET used as switch. The schematics are shown in Fig. 3.4 and the board in Fig. 3.5.

Fig. 3.4 shows three pins coming from the Teensy on the left. The Teensy supply voltage is step-up converted from 5 V to 15 V, which is needed to fully switch the MOSFET. The trigger signal from the Teensy, toggles on/off every half Lock-in period. Its on-state is indicated by an additional status LED. The resistor in parallel to the MOSFET unloads the gate capacitance and enables off-switching.

As currents and voltages applied to the module, may be harmful to the PC or the Teensy, the trigger signal is provided to the MOSFET via a galvanic insulation. This is realized by a CNY17 VISHAY optocoupler. According to the data sheet the optocoupler can not bear higher current then 100 mA, which is enough for switching a MOSFET. For short cutting the power supply a MOSFET with small internal resistance is device of choice.

Fig. 3.6: The thermocamera is elevated by a stand on the right side. On the left is the reflexion shield made of cardboard and styrofoam, sticked together with some type. Black felt cloths are put upon leaks in the shield.

3.1.2 Measurement procedure

Before starting a Lock-in measurement, a setup is performed (see Fig. 3.6). A module is mounted on the wall. The shield on the left will block temperature profiles from behind, coming from heating pipes or electronic devices.

In the next step, a reference emitter is added to the setup depicted in Fig. 3.7, preferably in the same focal plane as the module. The reference emitter is made from two parallel wires between crocodile claim. This wire resistance is placed in series with the module, and thermally indicates current flow. It is made from two thin wires, to decrease the maximum temperature, and to improve the mechanical robustness.

The idea of the reference emitter is to know the absolute phase shift. In future software advancement it could be used to quantitatively detect phase difference according to the glass upon the module.

It can be used after the software analysis to shift the phase image. This corrects the coloured phase image as the asynchronous measurement creates some random phase shift between the thermocamera and the driving current.

Shifting the phase image according to the reference emitter generates a phase-image scaled from -2π to 0. The 0-phase upon the module, underneath the glass can be approximated by searching for the first transmitted point source, regarding to the phase. Comparing to Tab. 2.3 point heat sources have a constant advance in phase compared to line or extended heat sources. The transmission through the glass adds a further constant phase to all heat sources, but does not compensate the phase difference to point sources.

After the camera is focused set on the module surface, a topography image is taken, for possible image corrections. Some topography images in Fig. 3.8 show a temperature gradient on the surface of the module . This leads to a small absolute difference between the peak temperature of e.g. equal point sources at different locations in each camera frame. It can be ignored as a constant effect due to using a Lock-in

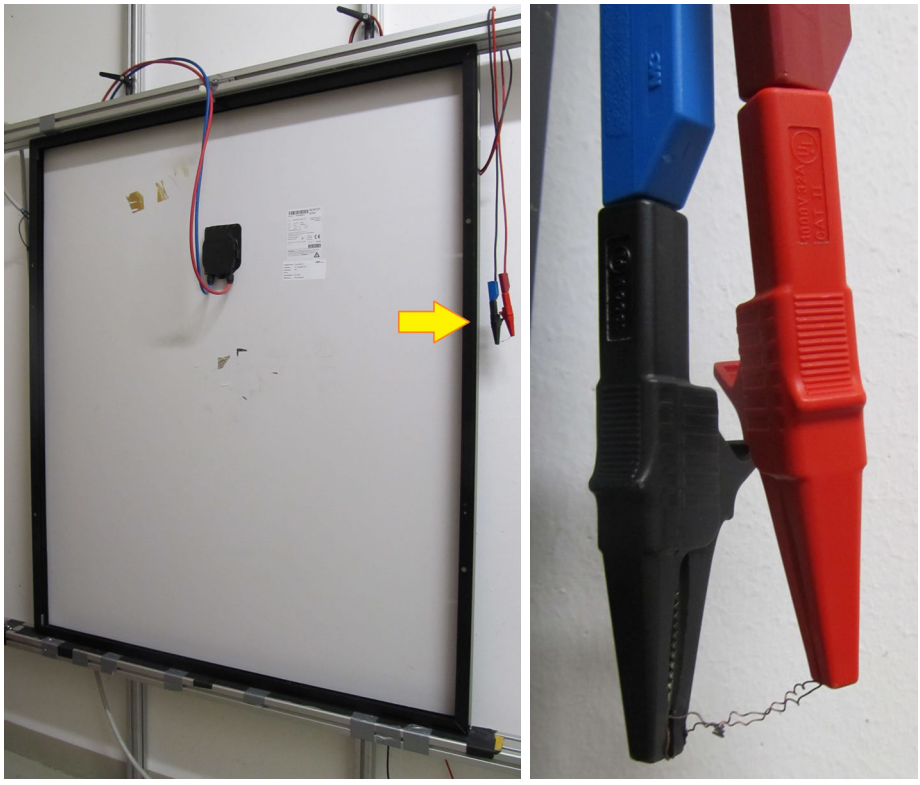

Fig. 3.7: Left a photography of the backside measurement of an amorphous silicon module is shown with the reference emitter on its right side. The reference emitter, enlarged on the right, consists of two parallel wires.

measurement. Future investigated surfaces may show emissivity differences, as they may contain different materials, having different emissivity at same temperature or different structures, that contain plains with different orientations, resulting in different emission intensities. All these differences will show different virtual temperatures for areas, having the same real temperature. These effects can not be ignored.

Further, any physical contact with the module heats or cools it locally. These locations can be seen in the topography image as well (see Fig. 3.8) and corrupt the correction. As all modules had a plain surface containing only one material (glass or backsheet), evaluations without the emissivity corrections were sufficient for qualitative investigations. A correction meachnism would need to recalculate the photon intensities $I \propto T^4$ from the topography image temperatures and calculate a factor for each pixel relative to the maximum intensity. Corrupted images are then converted to the according intensities as well, multiplying each pixel with it's factor and reconverting the intensities to temperatures.

Measurements are further prepared by setting the Lock-in period to the Teensy. As stated in section 2.3.8 at least two different Lock-in periods need to be measured to see different types of heat sources. Initially, always the higher Lock-in period was measured. The power supply is powered on and a specific current and voltage limit is set according to each module type to prevent damage to the module.

Measurements are done at each Lock-in period's stable mean temperature. The first few Lock-in periods will heat the module up to a certain temperature where the

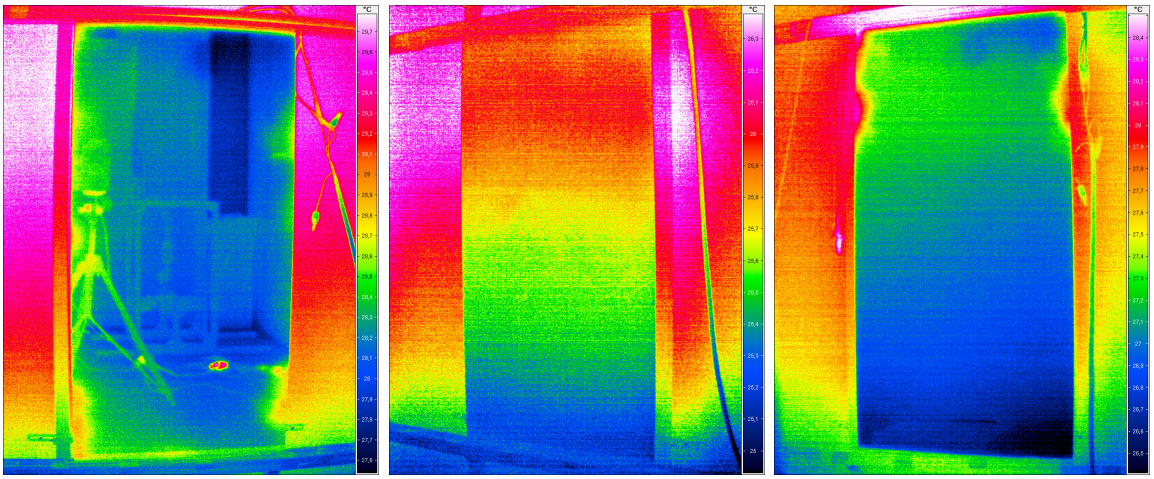

Fig. 3.8: Three topography images from CdTe modules were taken at room temperature before the measurement. On the left image no reflexion shielding is applied and the surrounding temperature emissions can be seen as reflexion on the module (the reflected camera is not the thermocamera). For the center one, the reflexion shield is applied, a temperature gradient can be seen on the module. The right image shows a topography image, with hand prints on the top edges of the module.

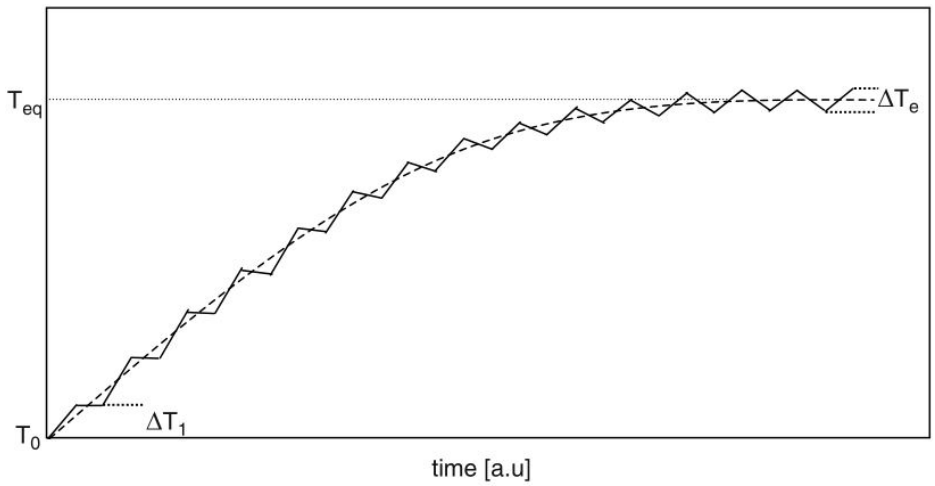

Fig. 3.9: The first Lock-in periods applied to a module a room temperature T_0 will increase the mean module temperature. After a while, heating is compensated by cooling and a stable mean temperature T_{eq} is reached with the amplitude being $\Delta T_e/2$. The dashed line shows the rise of the mean temperature. The image is taken from [7].

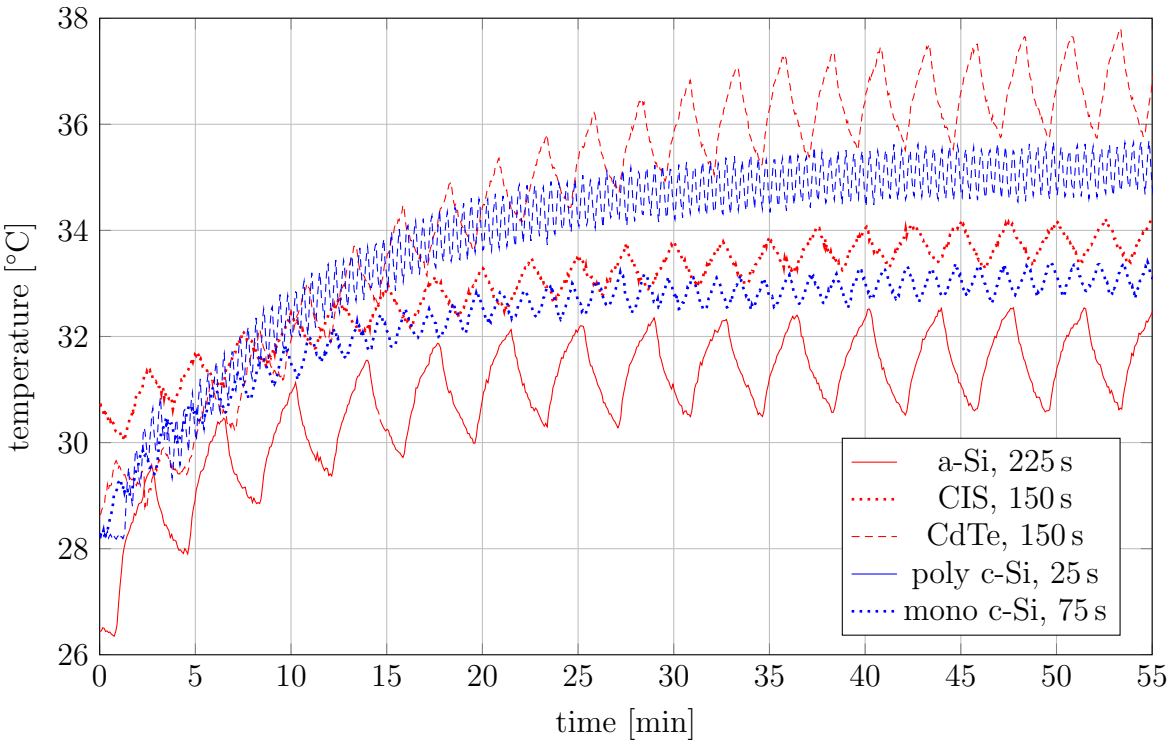

Fig. 3.10: Heatup processes for one module of each module technology was measured with different Lock-in period lengths. After approximately 45 min every module mean temperature can be considered stable.

half period of heating is compensated by the cooling in the second half (see Fig. 3.9). Therefore each period has a different mean temperature, corrupting demodulation. Only for equal mean temperature, the temperature signal coming from the module, can be demodulated as explained in section 2.3.4 without further corrections [7].

Heat-up processes measured for five different PV module technologies are compared in Fig. 3.10. Fig. 3.11 shows the difference in the amplitude image, measured at the same conditions, for a heat-up process measurement and a stable mean temperature measurement.

The heat-up process may take up to 45 min (see Fig. 3.10). The time for the measurement depends on the frame rate used for the two different Lock-in periods, which are suitable for characteristic images. For example a 150 s period and a 30 s period with both 450 constant frames per period (FPP), has frame rates of 3 FPS and 15 FPS. For 10,000 frames this leads to measurement times of about 56 min and 12 min, resulting in 1 hour and 53 minutes for one module.

A measurement consists of 10,000 frames, which are stored in files with 150 frames each. This makes 66 files with all together 14.7 GB storage size. The measurements are stored and afterwards analysed by a self-programmed software tool. This program and its functionality is explained in section 3.2. Its output will be amplitude, phase and in-phase images, which are compared for the different module technologies in section 3.4.

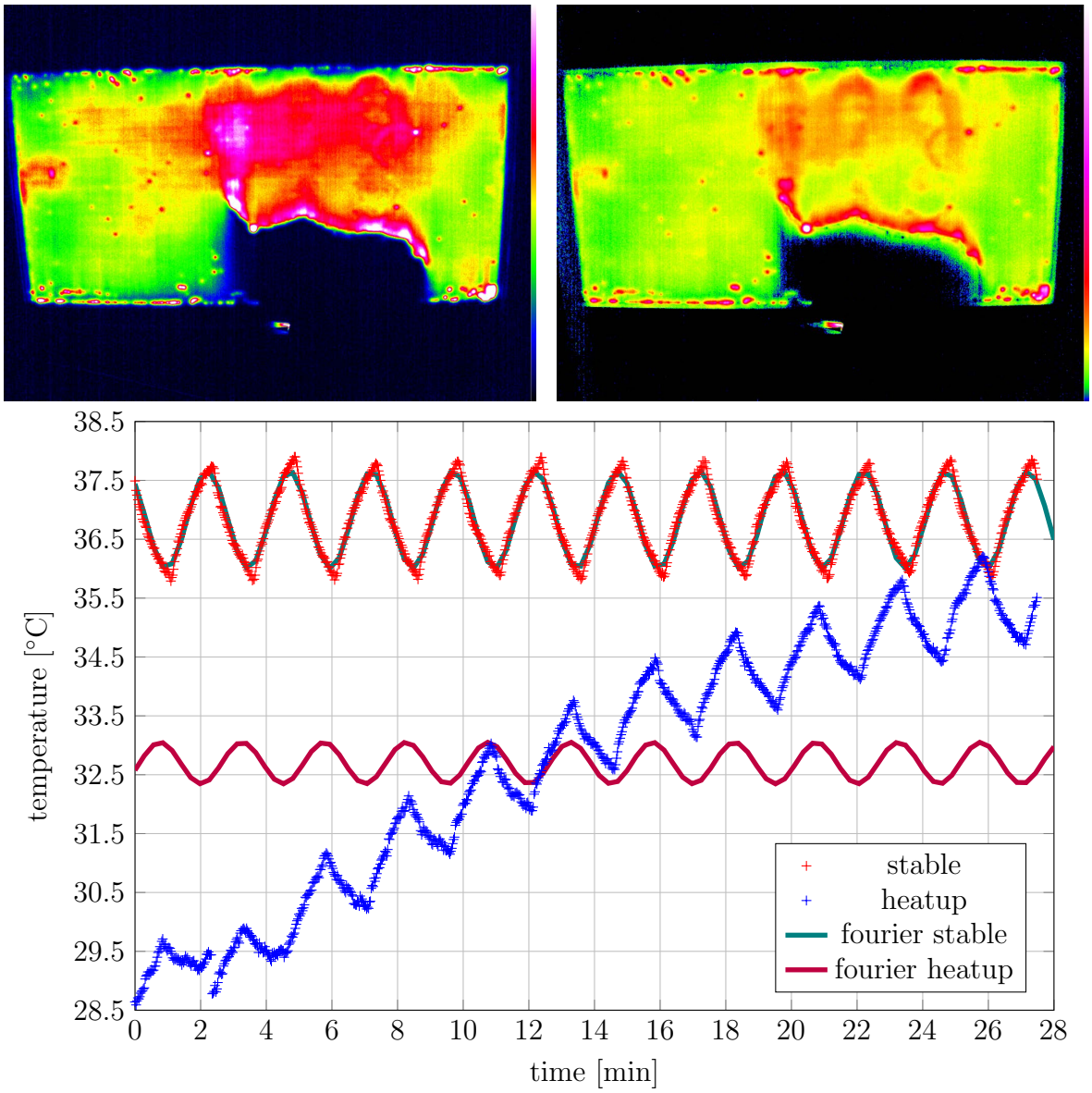

Fig. 3.11: Two DLIT-amplitude images are shown above. Both were measured with 150 s Lock-in period and 3 FPS and analysed over eleven periods. The left amplitude image is from the stable mean temperature measurement, the right is from the heat-up process of the same CdTe module. Below, a bright pixel is plotted for the stable and the heatup process. For comparison, the evaluated Fourier series for the basic harmonic is shown as well. For the heatup process weak point sources are strongly damped and strong ones are more dominant. The signal to noise ratio for the pixel noise according to section 2.3.7 is better for the stable procedure.

3.2 Software Tool

After the aquisition, signals need to be demodulated according to section 2.3.4. This task is done by a self-programmed evaluation tool. The software's functionality and work flow will be explained in the following section.

3.2.1 Functionality

The camera software stores frames in **.irb* files. These binary files are capable of holding more than one frame, saving pixel data in a 16-bit format, plus additional meta-data. Pixel data is saved with 10 mK precision, adding 273.15 K and multiplying by 100, thereby avoiding negative values.

As each frame has $1024 \times 768 = 786,432$ pixels, a single image consumes 1.5 MB storage. A measurement covering 10,000 frames, leads to 15,000 MB or approximately 14.6 GB.

The evaluation software, written in C++ using the QT toolkit [25], treats frames as matrix class objects, consisting of 32-bit floats. The above measurement of 10,000 frames, leads here to 30,000 MB or approximately 29.3 GB. This exceeds the RAM of typical PCs, thus each frame needs to be read and processed separately. Therefore FFT can not be performed, as it would need all frames in the RAM.

The camera software can export single frames into **.asc* text files holding, a matrix of temperatures. The first approach of the evaluation software was to read these files. There were two disadvantages: For temperatures around 30 °C with two digits precision, this results in five characters per temperature value, four numbers and one comma, plus an additional semicolon to separate data. A char is an 8-bit variable leading to 48 bit per temperature value and thus, three times the disc space. The second disadvantage is the slow read-in speed for text files.

To overcome these disadvantages, **.asc* files were converted into 32-bit binary float files (**.bin*) and in a later update to 16-bit binary integer files (**.b16*). This improved reading speed by a factor of 15 comparing **.asc* and **.bin*. The **.b16* files take just as much storage space as the original **.irb* files, and hence double read times.

The **.b16* files left two main problems. The camera software is needed after the measurements to export the **.asc* files and additional time needs to be considered for conversion from **.asc* to **.b16*. Furthermore, **.dat* files were introduced to save the Fourier coefficient images $\mathcal{C}_\ell$ and $\mathcal{S}_\ell$ after demodulation, where a second demodulation was not necessary, if re-importing **.dat* files instead.

On the other hand all the created files consumed extra disc space. The **.asc* file could of course be deleted, but storing **.irb* and **.b16* files takes twice the disc space of solely **.irb* files. Additionally issues came up in the evaluations, requiring the time where each single frame was taken at, for a correct evaluation (see section 3.3.2). This information is stored in the **.irb* files.

Direct reading **.irb* files was finally possible, due to finding patterns and knowing each file contains 150 frames. This allowed least possible storage consumption, evaluation right after the measurement, readout of the frame times and fast data import. The only draw back is that each **.irb* contains 150 files, which for two **.irb* files in the RAM, consumes $3 \cdot 300 = 900$ MB while demodulating. This further limits the

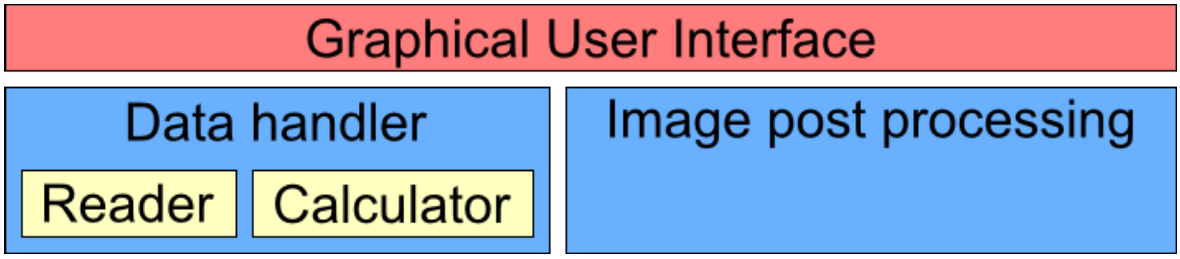

Fig. 3.12: The measurement evaluation software separates in five units for GUI, image post processing, data handling, reader and calculator.

amount of parallel demodulations to three or four, as the used 32-bit PCs offered 4 GB of RAM.

A demodulation using **.irb* files takes about 5 min. If a more accurate evaluation is desired, the time for each single frame is read from the **.irb* files and stored in a time table **.tbl* file. Once saved, the time table can be imported for any further evaluation of this measurement. The time table allows more accurate weighting factors (see section 2.3.3), leading to less error of the Fourier analysis. Reading all frame takes additional 5 min.

Frame times are stored in the **.irb* files in text characters, in a special format for minutes, seconds and milliseconds. Times are only updated after approximately one second. The time format is similar to `MMMss.mmm` where `MMM` stands for an arbitrary amount of digits for minutes, `ss` stands for seconds and `mmm` for milliseconds. Anytime 60 seconds have passed, the whole number typically increases by 40. The evaluation software treads times in milliseconds as integers and corrects the mentioned 1-second time steps linearly, assuming each different frame time is correct.

For the Fourier analysis, two Fourier coefficients ($\mathcal{C} + \mathcal{S}$) for each chosen overtone plus one for the mean image are stored as separate matrix class objects in a vector. In each discrete integral step a frame is pixel wise added, scaled with the corresponding sine or cosine and the time step. The integral is finished by normalizing on the totally integrated time. For amplitude and phase images a separate vector is allocated. After the demodulation, $4n + 5$ matrix class objects are stored in the RAM, dependent on the amount of overtones n additional to the mean image and the four images for the basic harmonic. Each image consuming 3 MB RAM leads to an additional RAM usage of (12n+15) MB.

The evaluation program is roughly separated in classes for GUI, image post processing, data handling, reading and calculating (see Fig. 3.12). Theses five classes are connected through QT signals and slots and in a pyramid hierarchy. The GUI class handles the user input and communicates tasks to the data handler class and the image post processing class. The data handler holds the information on the current task and is responsible for coordinating file import and Fourier analysis. It further calculates amplitude and phase images, imports and corrects time tables and calculates noise (see section 2.3.7) and phase shifts. Reader and calculator are operating in separate threads, enabling parallel reading and processing of **.irb* files. The image post processing class stores information on the currently visible image, allows saving the current image as **.dat* or **.png* file and processes images according to the GUI commands.

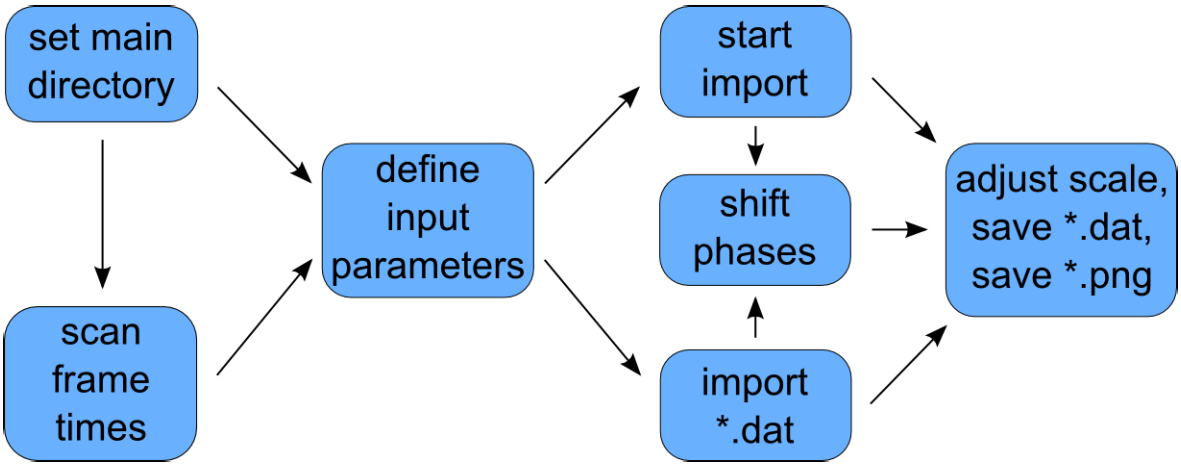

Fig. 3.13: The workflow starts in the upper left, by selecting a directory. The endresult is an image, investigation or **.dat* file on the right. The paths are described in the text.

3.2.2 Workflow

The evaluation process is depicted by Fig. 3.13. The user starts the program called *Lockin* and the window Fig. 3.14 pops up. The window separates in 3 main parts. On the left is a toolbox with various settings. A status bar is on the bottom, indicating `Ready` at that moment. The rest of the window is the image area.

Initially a working directory is specified in the `Main Directory` toolbox item, containing the files from a new measurement. The separate toolboxes on the left of the GUI are shown in detail in Fig. 3.15. The GUI displays the amount of found files, with the estimated number of frames in braces next to `.irb/.IRB` and shows a preview of the first frame found in the selected directory.

A different preview frame can be chosen in the toolbox `Preview Frame` if **.irb* files are present. A dropdown menu allows selection of the **.irb* file and the frame inside this file can be chosen by the spinbox below. Clicking on `grab` imports the selected **.irb* and shows the new preview image.

The preview image can be adjusted in the image area. On the bottom right the currently shown image can be saved as **.png* or **.dat* with a preferred file name. The info on the current scale is shown below the image. There the maximum and minimum value of the `Image` and the currently set `Scale`, as well the cursor position and pixel value are provided. Next to `Scene` the displayed image can be changed to the amplitude, phase, cosine $\mathcal{C}$ or sine $\mathcal{S}$ image. The second dropdown menu allows selection of the Index ℓ and the last dropdown allows selection of the image coloration. The colorbar is at the right of the image and will saved to the **.png* as well. On the lower right of the image, the scale can be adjusted. The top row controls the scale maximum, the bottom row controls the minimum and the center row allows altering the linearity of the colorbar. `Opmax` and `Opmin` will set the scale to the maximum, respectively minimum value of the image, a custom scale limit can be set next to them, with the option of varying between 0 and 100% of the set value. The column on the right allows to set a scale increment and shift maximum and minimum up or down. On the upper left of the image the zoom can be set, while holding down control and scrolling with the mouse allows manual zoom. If displaying the `Preview` image, certain

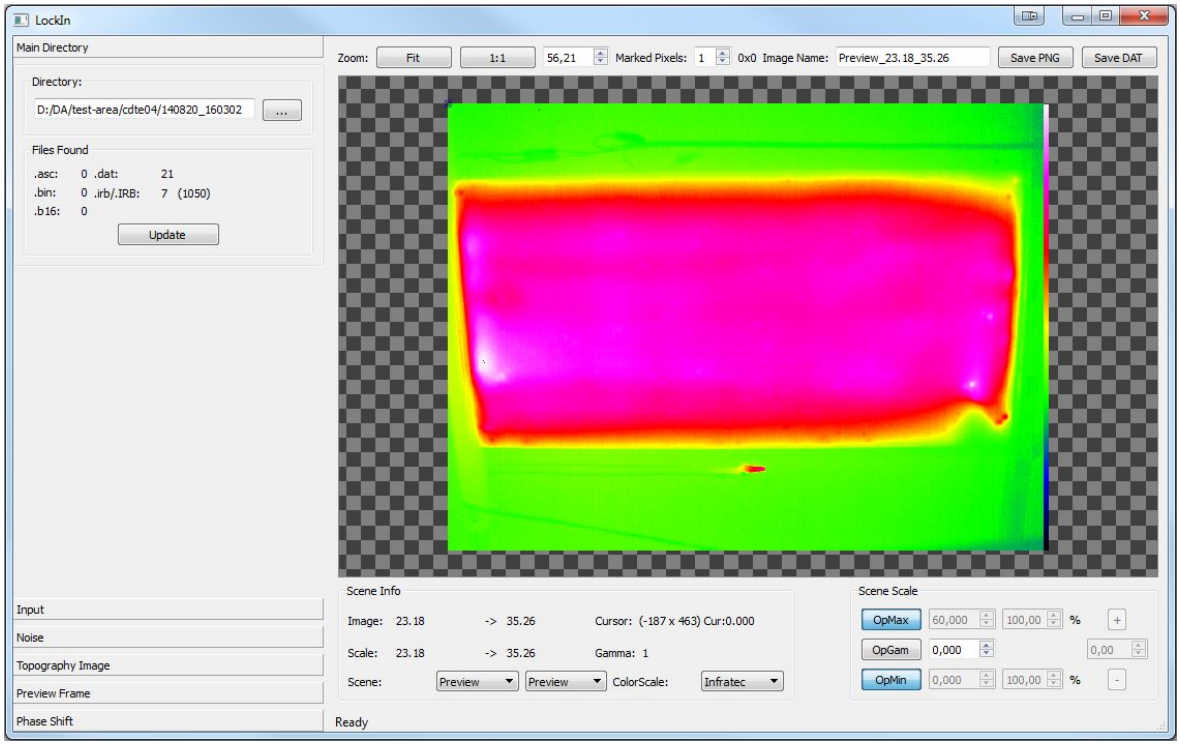

Fig. 3.14: The graphical user interface (GUI) consists of a toolbox section on the left, including the import and a right part for viewing and scaling images. Buttons on the top allow to export images. The toolbox is shown in detail in Fig. 3.15

pixels can be marked by cross hairs. Increasing the `Marked Pixels` spinbox adds cross hairs in the top left corner of the image. They can be dragged and dropped with the left mouse button. Decreasing the number of marked pixels, first deletes cross hairs at (0;0) if present, otherwise the last added first. Marked pixels are stored while importing, are saved to a separate **.txt* files with corresponding position and **.gp* file for visualization with gnuplot. Pixel noise is calculated in the *noise.log* file for all marked images.

In `Input` all parameters for importing the measurement can be set and the import process can be initiated. In the presented example, the user may start with `Scan Frame Times`. The program will then go through all the frames, checking for the time they were taken at, while the status bar indicates how many **.irb* files have been read. The process finishes in saving a **.tbl* file. A present **.tbl* file enables the `Period [ms]` spinbox. The user may now select the start frame, number of periods and overtones to be demodulated. Having scanned for a time table, one enters the Lock-in period in milliseconds instead of entering the amount of frames per period at `Period [Frames]`. The program watches the limits of this investigation and allows only possible input, indicated by the braces next to each spinbox. Before importing the user may check for auto-file saving options. It is recommended to check the **.dat* `Coefficients` export, as they can be imported in further investigations, without the need of a redundant demodulation. A dropdown menu allows the selection of the `File type` to be imported. Checking the `Auto Convert` checkbox, automatically calculates the amplitude and phase image after demodulation. Otherwise, the user has to click on the button, after in-phase and quadrature images are available. `Import` starts the

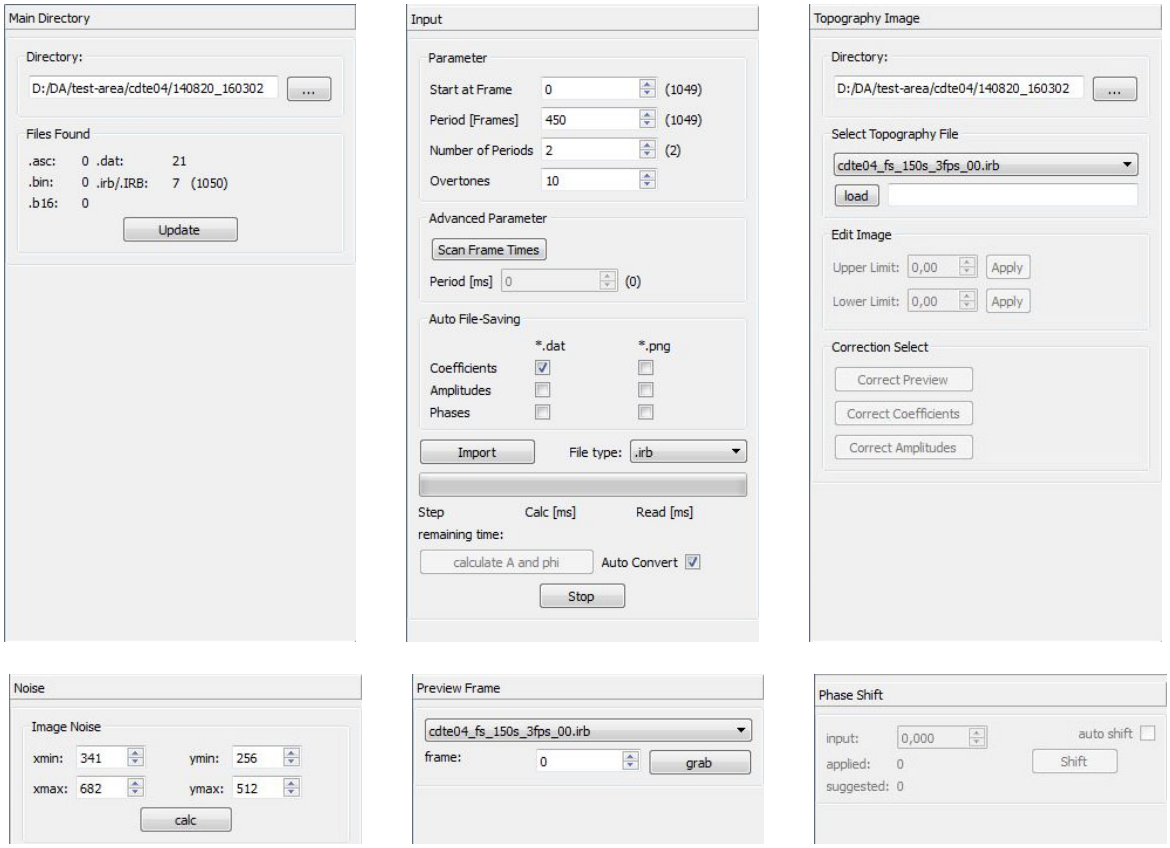

Fig. 3.15: The toolbox of the GUI Fig. 3.14 is separated into several parts. The working directory can be set in `Main Directory`, while all import settings are set in `Input`. The `Topography Image` part allows importing a separate topography image for emission correction. In the `Noise` section the area for calculating the image noise (see section 2.3.7) can be defined. `Preview Image` allows choosing the depicted preview image. Last the `Phase shift` section allows setting the offset phase in rad. This is especially useful, as the overflow corrupts the visibility of phase images.

demodulation by processing files parallel tor importing the next ones. A valid import stores the selected frame parameters under `Paramter` and `Advanced Parameter` in a **.ini* file. Further selections of this memory will recognize the **.ini* file and import the last settings. Already present **.ini* files will be overwritten. While importing a progress bar indicates the progress of the import, additionally to the remaining time and comments in the status bar.

The demodulation process is done, if the status bar writes `done`. The $\mathcal{C}_0$ image will then be displayed in the image area. The index 0 indicates the basic harmonic, while indices greater 0 indicate the corresponding overtone. The images can now be selected, scaled and saved as explained above. Further the image noise was calculated for all generated images in the *noise.log* file. This calculation can be manually triggered using the `Noise` toolbox item. There an area inside the image can be set, which is by default the center ninth of the image. Adjusting this area prior to pressing the import button will affect the area of the automatic calculated image noise.

The $\mathcal{C}$ (cosine), $\mathcal{S}$ (sine) and phase image show a further display option in their dropdown menu indicated by appendix `_shifted`. The phase shift can be set in the

toolbox item `Phase Shift`. For leaving 0, the shifted image equals the basic harmonic image. Selecting an `input` changes the image maximum and minimum to -2π and 0, with 0 being always the selected phase relative to the primary evaluated phase image. A phase shift is applied by clicking the `Shift` button and the currently `applied` phase difference is shown. Checking the auto shift checkbox, will calculate any phase shift, entered in the input spinbox without the need of clicking the button. Leaving the phase shift and clicking on the shift button again, will not change the image. The phase can be shifted within a range of $-\pi$ and π and allows to correct phase overflows in the image. The `suggested` phase shift shows the phase of the pixel with the highest amplitude. Phase shifts are always applied to all shiftable images.

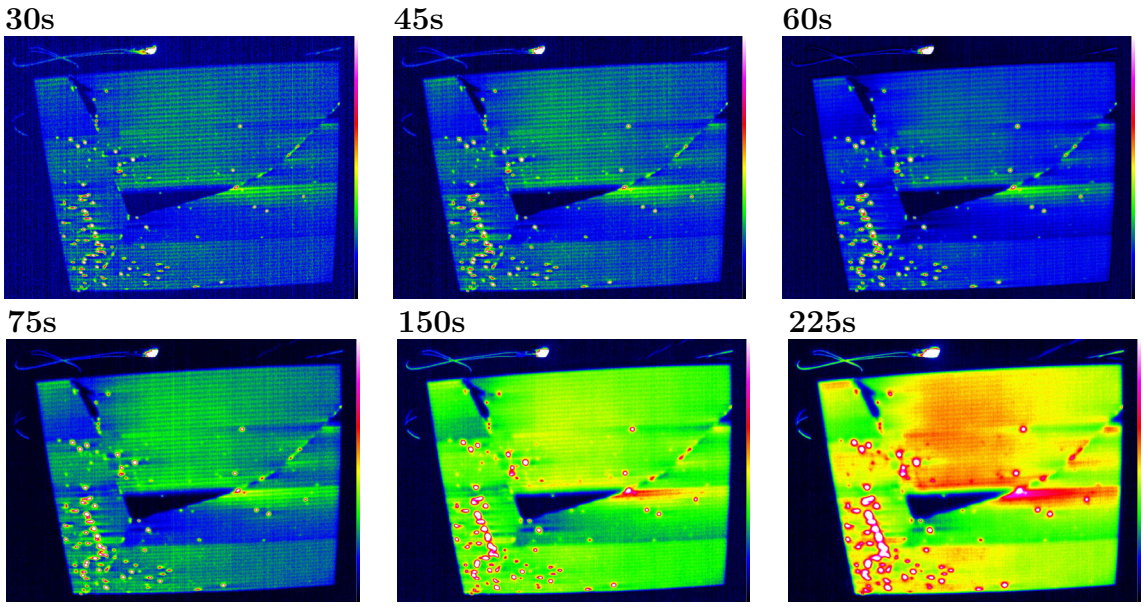

Fig. 3.16: These amplitude images were measured from front side at different Lock-in period lengths. All images are scaled to 20% of their maximum amplitude upon the module. From the shortest to the longest Lock-in period, the module maximum is about: 0.719 K, 1.023 K, 1.250 K, 1.473 K, 2.13 K and 2.524 K. This amorphous silicon module shows several point sources and some extended heat sources. The point sources blur for higher Lock-in period, the extended heat sources become better visible. The dark areas are not plated-through.

3.3 Measurment Characteristics

Various measurements were performed to investigate optimal measurement conditions. In the following sections several comparisons will present the characteristics of the measurement setup.

3.3.1 Frequency dependence

Section 2.2.2 introduced the frequency dependent diffusion length. This dependence increases the resolution of Lock-in thermography compared to steady-state thermography [7]. According to section 2.3.8, the amplitude image varies for different Lock-in frequencies, which was observed in the measurements. In Fig. 3.16 amplitudes at different Lock-in period lengths are presented for an amorphous silicon (a-Si) module. The images are scaled to 20% of the maximum amplitude on the module, to further increase the contrast - the upper 80% are saturated to white.

As mentioned in section 3.1, there are only several possible frame rates to choose. For comparable noise in the results, according to section 2.3.7, all measurements were taken at 450 frames per period and for about 10,000 frames.

The depicted a-Si module was measured from the front side, where glass was covering the module. Refering to Fig. 2.5 glass has a very low diffusion length and therefore the whole module can be considered as thermally thick in these measurements. Only the last two Lock-in periods of 150 and 225 s may be in the order of the thermal thickness. For too low frequencies as 225 s the heat spreads farther and the amplitude image

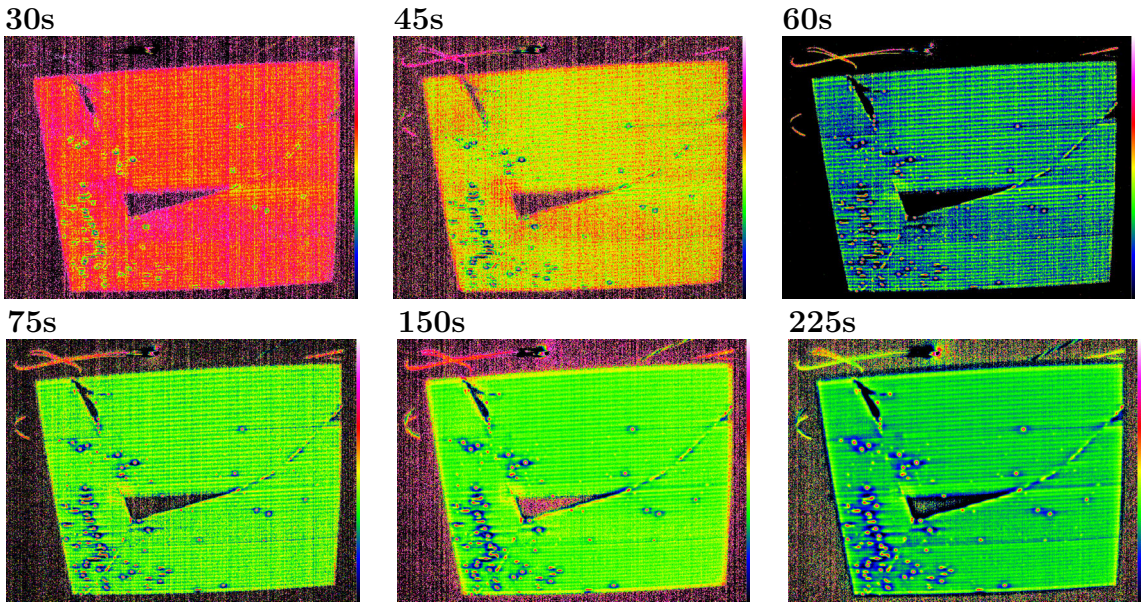

Fig. 3.17: These phase images were measured at different Lock-in periods. The first row from left to right at 30, 45 and 60 s, the second row from left to right at 75, 150 and 225 s. All images are scaled from 0 to -2/5 π] and are phase corrected to be in-phase with the point sources. For short period length the image is very noisy, but for long ones images get blurred. Extended heat sources are not visible.

looks blurred. The blurring can be observed at all point sources and at the shape of the broken out part in the middle. In contrary, the images for too short Lock-in period lengths as 30 s and below do show increasing noise.

The phase images show stronger dependence of the noise on the Lock-in frequency. Fig. 3.17 shows the phase images for the same Lock-in periods, scaled from 0 to -2/5 π. Point sources are scaled in-phase. A good result can be obtained by the phase image of 60 s or 75 s. As discussed in section 2.3.8, all point sources can be viewed in equal brightness in the phase image. Also the extended heat sources, visible in Fig. 3.16 are strongly surpressed and not visible in the phase image.

The decreasing resolution of the point sources are shown in more detail in Fig. 3.18. A point source without disturbing extended heat sources or other point sources is chosen.

Finally the image noise shall be compared for amplitude and phase images. A rectangular area in the upper right of the depicted module from 280;120 to 880;420 is set, to avoid errors from the not contacted areas.

3.3.2 Frame rate corruption

While evaluating the measurements some issues were found with the data, which urged further treatment by the software. If the frame rate of the camera was constant and the heating pulse was truly periodic, then the time step could be omitted, leading to simplified equations mentioned in section 2.3.4.

The camera software stores all the frames in binary files. By looking for similarities inside the file, it was possible to find the UTC time of each frame and the frame data

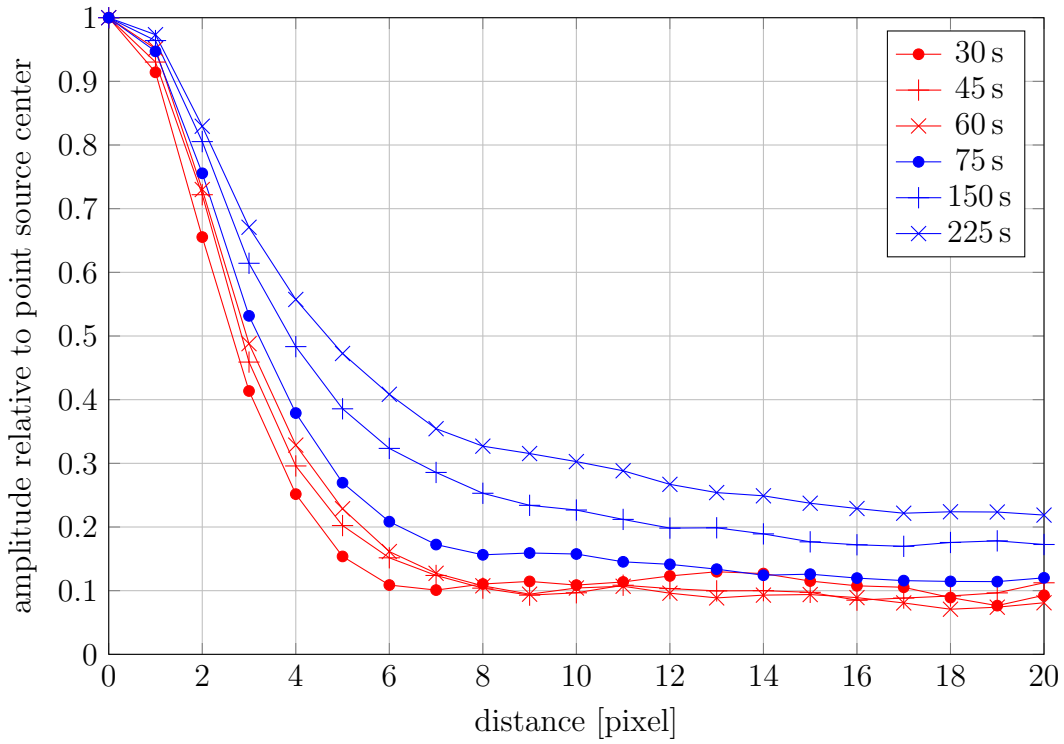

Fig. 3.18: The distance from a point source is shown in pixels, where all data are scaled to the maximum at the center. Within 20 pixels 150 s and 225 s only fall to 20 percent of the point source amplitude temperature, what is double compared to 30 s. In agreement with section 2.3.8 the halo around point sources spreads farther with increasing Lock-in frequency.

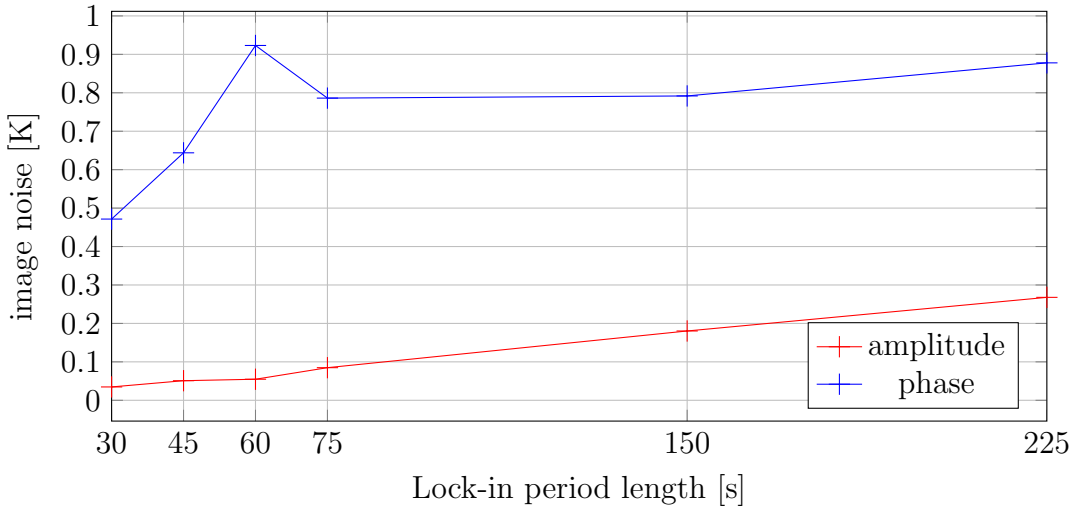

Fig. 3.19: The image noise in absolute values for different Lock-in periods is shown for amplitude and phase images using the attempt described in section 2.3.7. The area was chosen between 280;120 and 880;420 in the upper right of the module shown in Fig. 3.17 and Fig. 3.16.

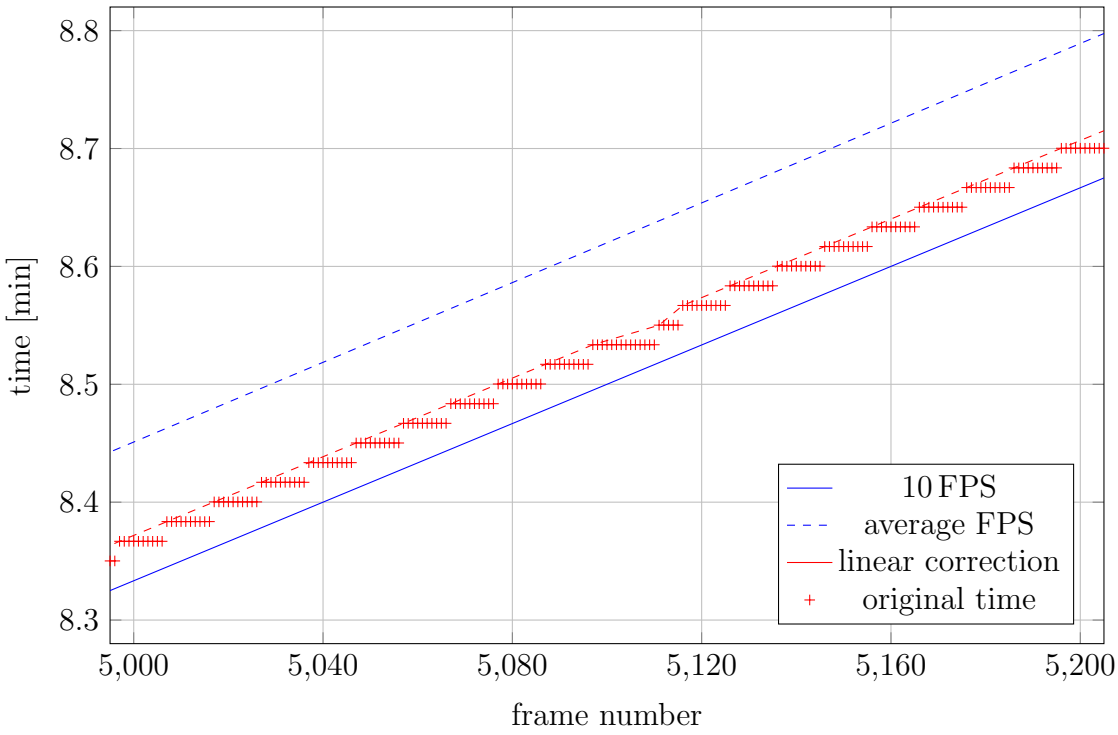

Fig. 3.20: The original time shows the time stamps of each frame according to the camera software, taken from a measurement with 10 FPS. The red line is the applied linear correction to attach every frame to a different, chronological time. In addition the straight line for 10 FPS is shown. The dashed blue line is the straight line between the time of the first and the 10,000ths frame.

itself. On the one hand this allowed direct usage of these files, on the other hand also the time of any frame in milliseconds could be analysed. Fig. 3.20 shows a comparison of the stored time to the average time step if taken the very last and first time and the time line, if the frame rate were constant, measured with the amorphous silicon module at 10 FPS. Further the time correction of the software is shown.

The original time shows the time stamp of each frame according to the camera software. This time differs only every tenth frame in average, although milliseconds are actually saved. Sometimes, as shown around frame 5,100, more frames seem to be taken at the same time and later less at the next time. The time steps are close to one second, so for 30 FPS it was observed to be about 30 frames for each time. As this is not physically, every time step is corrected linearly and each frame in between is set to the according time.

The difference from on step to the next is not exactly 1 second. Thus the original time does not overlap with the blue 10 FPS time line of the actual measurement. This can be seen by comparing to the red dotted data or to the dashed blue line, which is the straight line between the first and the 10,000ths frame. The blue lines are about 6 seconds apart.

These volatile time steps lead to an error, if one is calculating the Fourier series using a constant number of frames per period (FPP), omitting the actual time step. A comparison of the pixel analysis is shown in Fig. 3.21. A pixel in a measurement with 10 FPS and 15 seconds Lock-in period duration (so 150 constant FPP) was evaluated

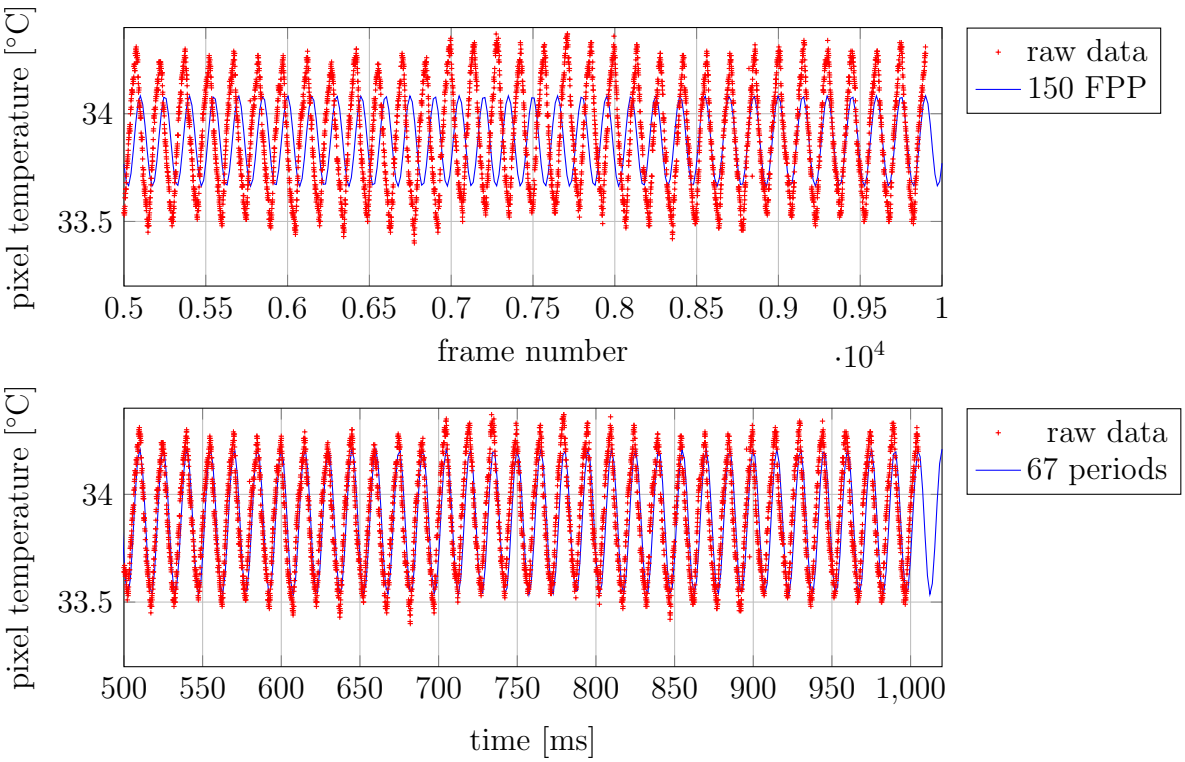

Fig. 3.21: The upper graph shows the basic harmonic of the Fourier series for 150 constant FPP, the lower shows the basic harmonic, after time corrections. The according measurement was taken at 15 FPS, the Lock-in period length was 10 s, and 10,000 frames were acquired. The corrected Fourier series has more than 50% higher amplitude and fits the data more properly, while in the upper graph the Fourier series does only fit in the end.

with and without considering the frame time. Fig. 3.22 compares amplitude and phase of both evaluations.

If the frame rate is constant within one step, these conditions are met. If not, the error does not accumulate, as the next step starts with a correct time and the error is only within the last second. For calculating with constant FPP, the whole series would be corrupted, if there is a slight difference in at least one step.

Some measurements also showed about 40 min of additional time somewhere in between. Subtracting the 40 min from all frames of the second part, both parts fit perfectly together. All these frame rate corruptions are regarded by the developed evaluation software.

3.3.3 Difference between back and front side

Modules with backsheets rise the question of the difference between measuring from the back or front side. Measurements showed that investigations from the back side do require a smaller Lock-in period than measuring the glass side. This section shall show that effect for a mono crystalline silicon (mono c-Si) module. Typically, thin film modules have a glass back, only one available amorphous silicon module had a backsheet.

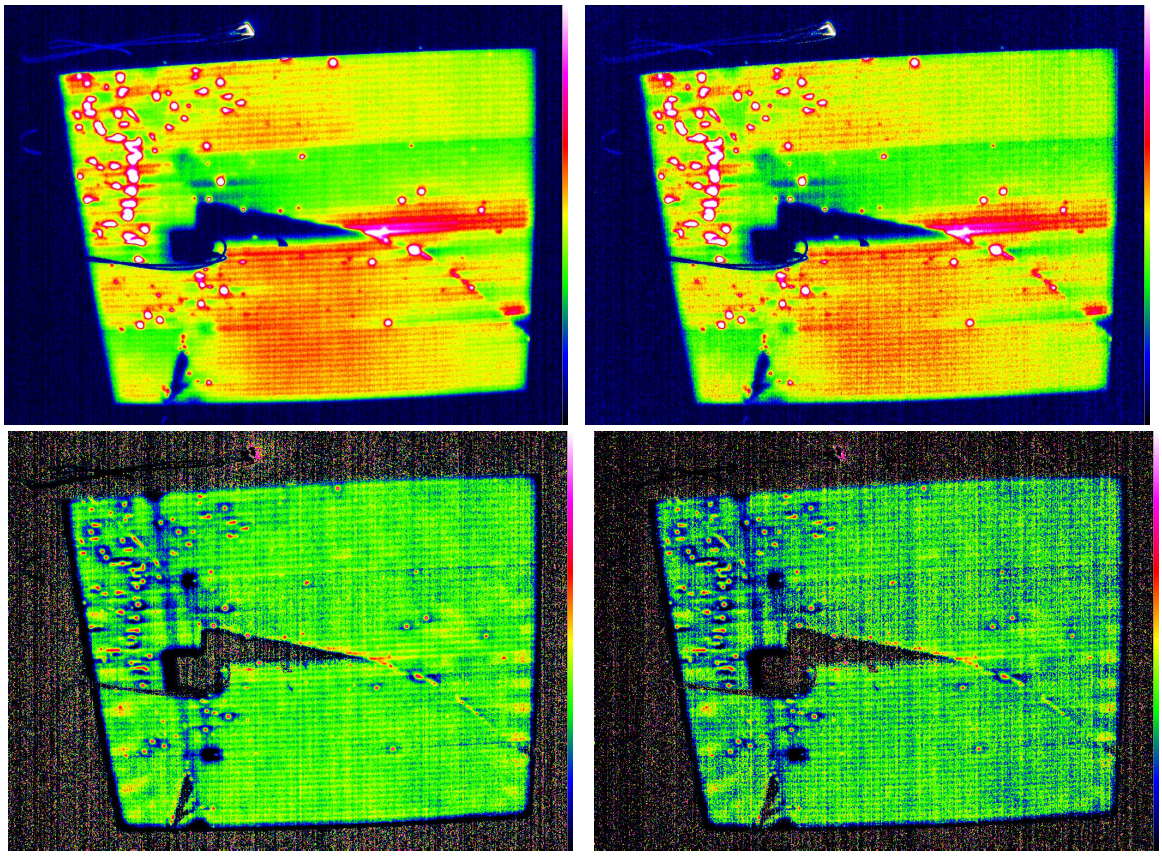

Fig. 3.22: Comparison of the time corrected images on the left and the 150 constant FPP images on the right of a back side measurement. On top the amplitude is shown, below the phase image. The 150 constant FPP amplitude image seems more noisy and the extended heat sources are more damped. Both amplitude images are scaled to 15% of the maximum amplitude on the module. The 150 constant FPP phase image seems also more noisy then the right one, but for the phase it is more obvious than for the amplitude. Both phase images are scaled from in-phase to $-\pi/4$ delay.

The mono c-Si module was measured at 5, 10, 15 and 20 s from back side - each 10,000 frames and 150 constant FPP to be comparable. For front side measurement, as above, 450 constant FPP were performed at 30, 45, 60 and 75 s, again with 10,000 frames each.

The amplitude images for front and back side are shown in Fig. 3.23, the phase images in Fig. 3.24. Noisy images for the lowest times show that front side measurements need to consider longer Lock-in periods than back side. Further front side images look more blurred - best compared at the busbars, which can be seen in the phase image as well. Thus it is preferable to measure the backsheet, instead of to the glass side - if possible. The only draw back is the junction box on the backside, which prevents the analysis of one part of the module.

Comparing the phase between the reference emitter and the in-phase signal of the module exhibits a delay, which is related to the transversed material. Tab. 3.1 shows a comparison for the glass and the backsheet side. Glass seems to cause a higher phase difference, which could be the reason for the greater blur of front side measurements. The phase difference decreases with rising Lock-in period length, which is in perfect

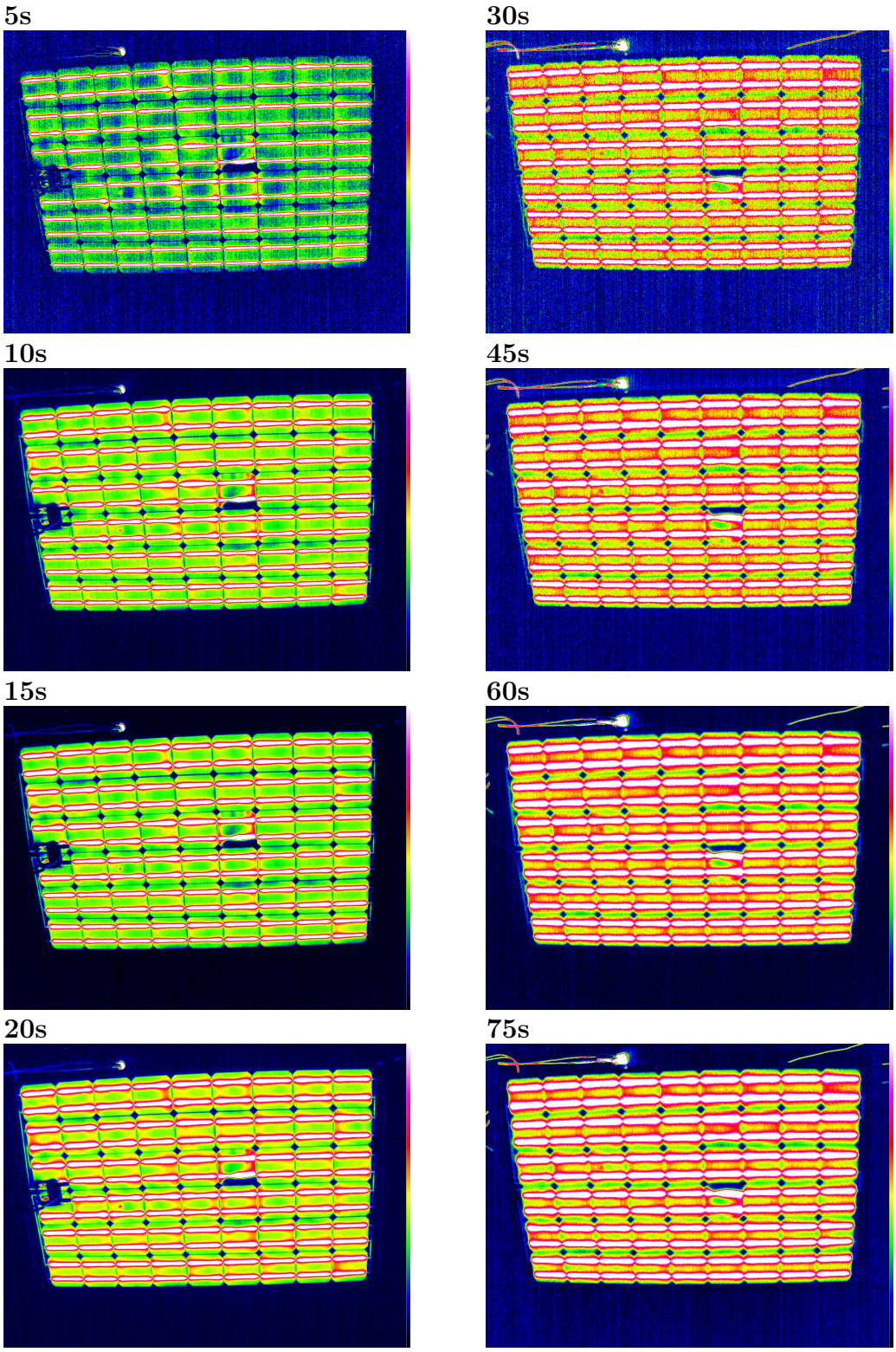

Fig. 3.23: All amplitude images are scaled from 0 to 30% of the maximum on the module. The images on the left show the back side measurement, the right shows front side measurements.

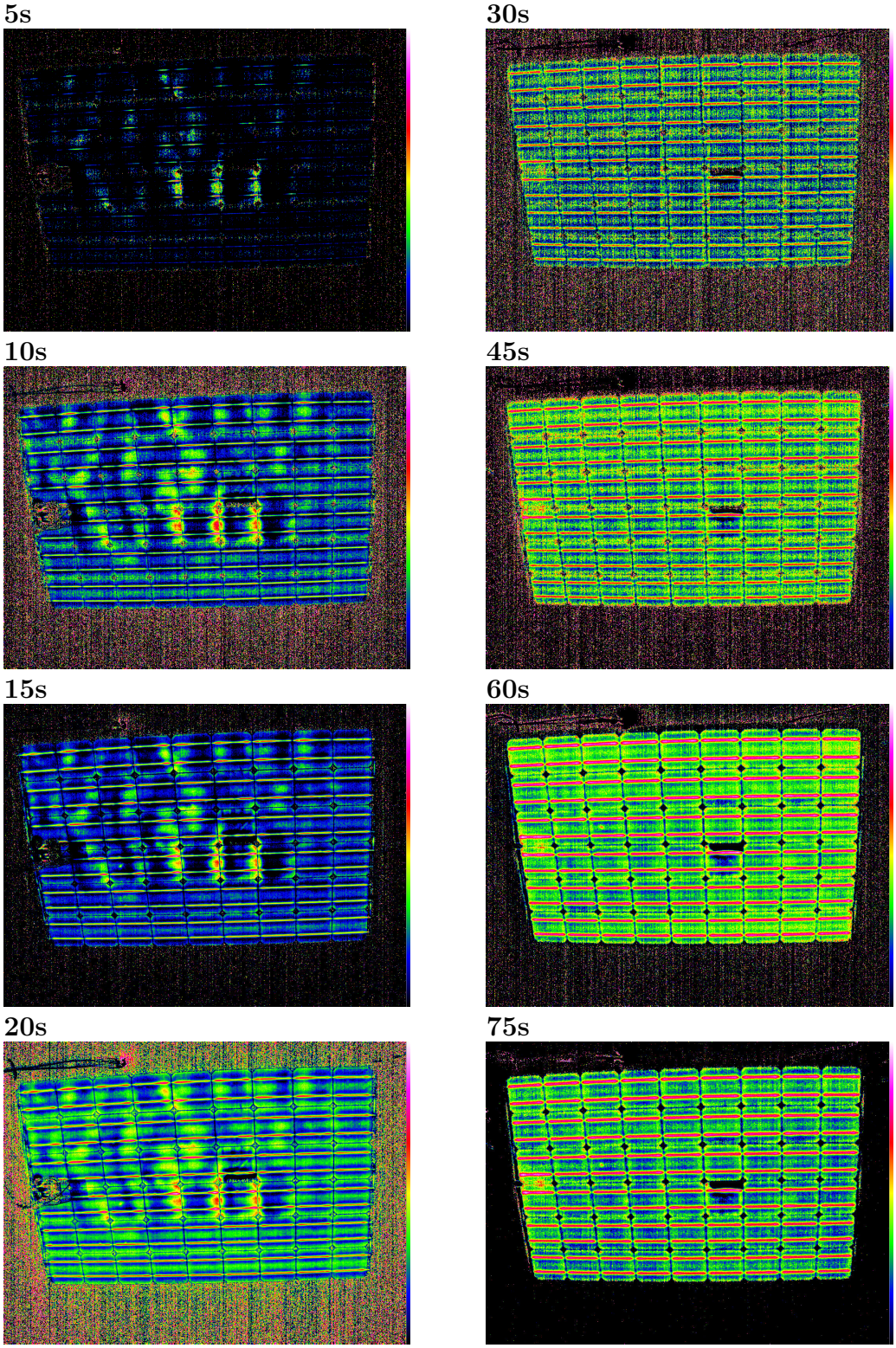

Fig. 3.24: All phase images are scaled from 0 to $\pi/4$ delay of the first phase upon the module - all values below are black. The images on the left show the back side measurement, right shows front side measurements. The 5 s back side measurement is too dark, due to a too short period length.

back side		front side	
$T_{\text{Lock-in}}$ [s]	$\Delta\varphi$ [rad]	$T_{\text{Lock-in}}$ [s]	$\Delta\varphi$ [rad]
5	0.99	30	1.91
10	0.80	45	1.70
15	0.65	60	1.63
20	0.54	75	1.46

Tab. 3.1: Back and front side measurements are compared according to the phase delay relative to the reference emitter. This calculation is based on the pixel with the first phase upon the reference emitter and the pixel with the first phase upon the module. As the delay decreases with rising Lock-in period length, and the backsheet has a smaller diffusion length (see Fig. 2.5), the backsheet is obviously thinner than the glass.

pixel	A	B	C	S1	S2	S3	S4
σ [mK]	53	45	44	53	55	54	62

Tab. 3.2: The pixel noise of three pixels upon the module (A,B and C, see text) and the standard deviation of four pixels of the (S1 - S2) surrounding was evaluated for 22 periods. The mean of the evaluated camera pixel noise is at 56 mK, close to temperature resolution (see section 3.1). The pixel noise is slightly below the camera pixel noise, therefore showing a good fit of the Fourier series to the time series of pixel data.

agreement with the definition of the diffusion length (2.16).

3.3.4 Comparison for different amount of frames

Data from the measurement of a CdTe module at 45 s Lock-in period length is taken for comparing the amount of periods analysed, in noise and resulting images. This comparison can clarify how long a measurement needs to last, as up to now for all measurements 10,000 frames were chosen.

All compared evaluations start at the first frame and last for 1, 2, 4, 8, 16 or 22 periods, using the time line import with time correction (see section 3.3.2). Using same data for all evaluations guarantees same conditions.

Tab. 3.2 shows the pixel noise according to section 2.3.7 for a pixel right at a point source (A), for a pixel within an extended heat source at a point source (B) and for a pixel in an inconspicuous area upon the module (C). Only the basic harmonic was evaluated.

Furthermore, four pixels (S1 - S4) in the surrounding of the module (which should have same temperature for the whole measurement) were chosen to evaluate the camera pixel noise σ_{cam}. For these simply the standard deviation was calculated.

The amplitude images are shown in Fig. 3.25. The corresponding evaluation of image noise according to section 2.3.7 is presented in Fig. 3.26. An amplitude image comparison reveals, that the images SNR increases with rising amount of frames. Further a quite good result can be achieved for at least eight periods.

The phase images are shown in Fig. 3.27. first and second image were to noisy to show any result. Four periods shows all point sources, but is still quite noisy. Also for the phase image at least eight periods are suggested. The image noise for the phase

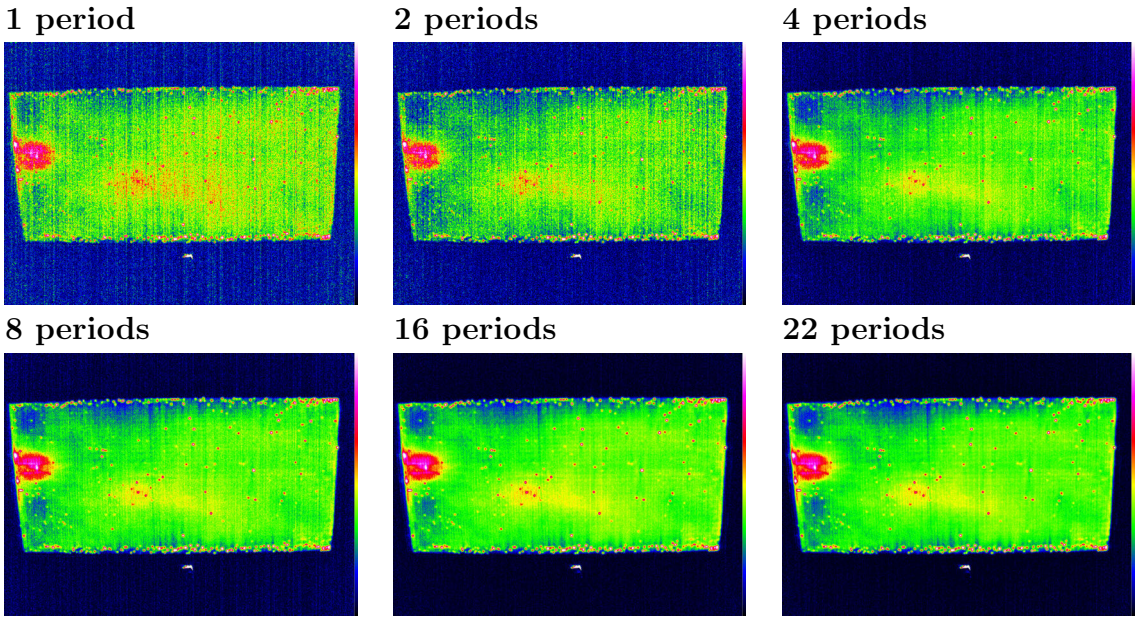

Fig. 3.25: The amplitude images were evaluated for different period length for one measurement. All are scaled to 50% of the module maximum. Same data, from a 45 s Lock-in period and 10 FPS measurement, was used for all images.

images is presented in Fig. 3.28. All phase images where shifted to avoid overflows, the first and second image were chosen to have as less phase overflows as possible upon the module.

An evaluation of phase image noise is difficult, as phases are always scaled in a range of 2π, and its periodicity leads to phase overflows in the image. In Fig. 3.28 the noise reduction is clearly visible, contrary to Fig. 3.26, which shows only a reduction from the one period image to the others.

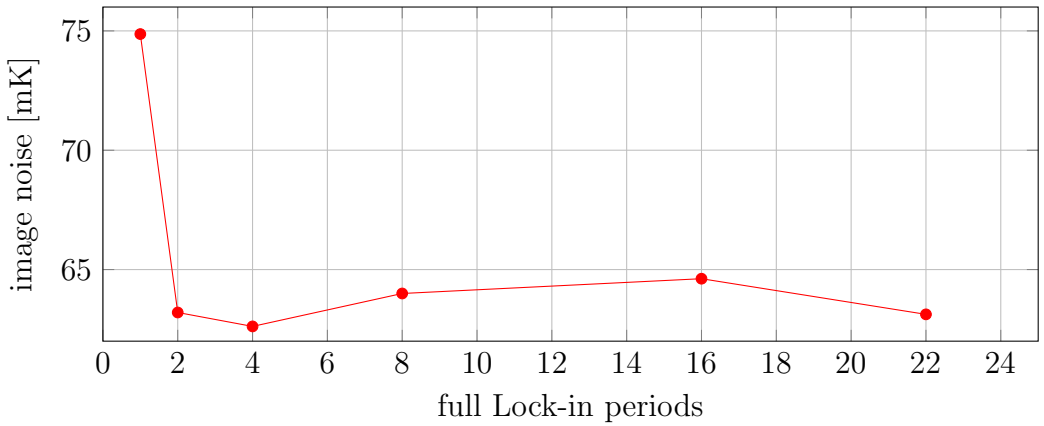

Fig. 3.26: The image noise was calculated for the amplitude images in Fig. 3.25 according to section 2.3.7. The chosen rectangular evaluation area extended from 40;170 to 920;560 and covered nearly the complete module, without the surrounding.

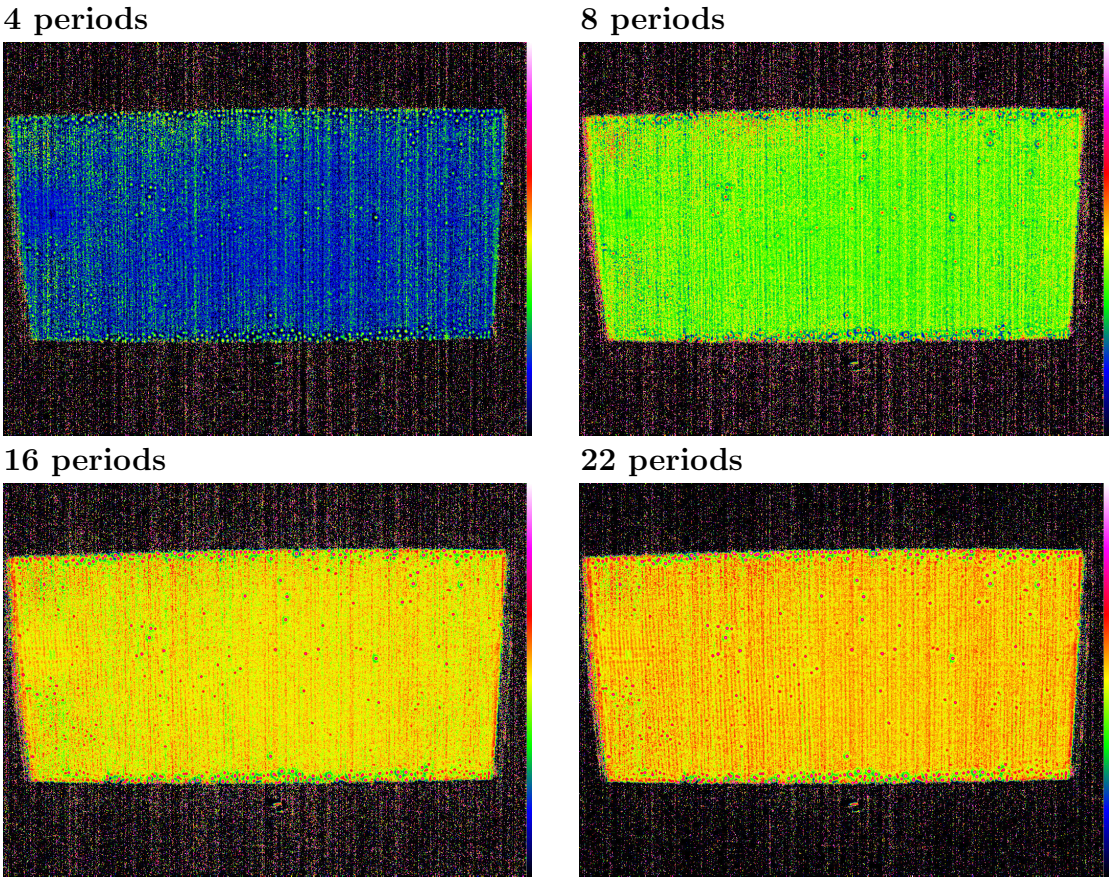

Fig. 3.27: The phase images were evaluated for different period length for one measurement. All images are scaled from the first phase upon the module to 2/5 π delay. Phase images for one and two periods are omitted, as they were to noisy - even the 4 periods image is still quite noisy.

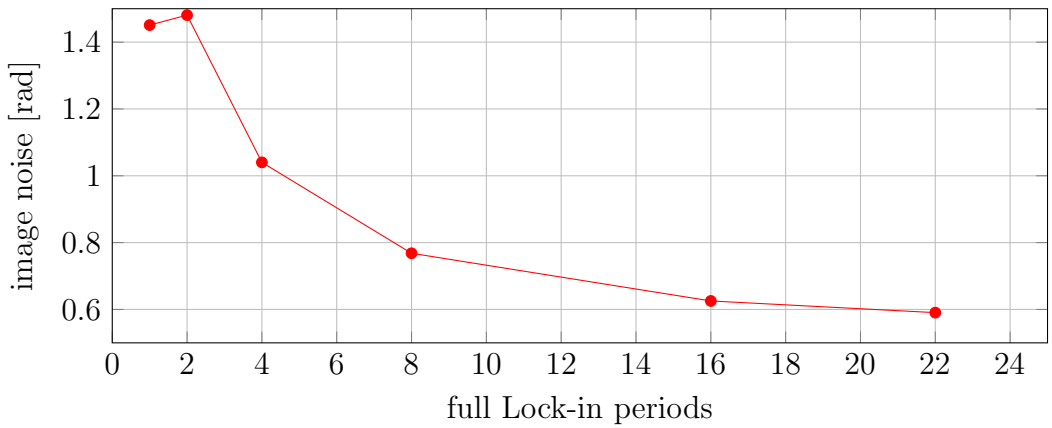

Fig. 3.28: The image noise was calculated for the phase images in Fig. 3.27. The chosen rectangular evaluation area covered nearly the complete module without the surrounding. Here, in contrary to the other evaluations the image noise is compatible with the subjective image noise impression.

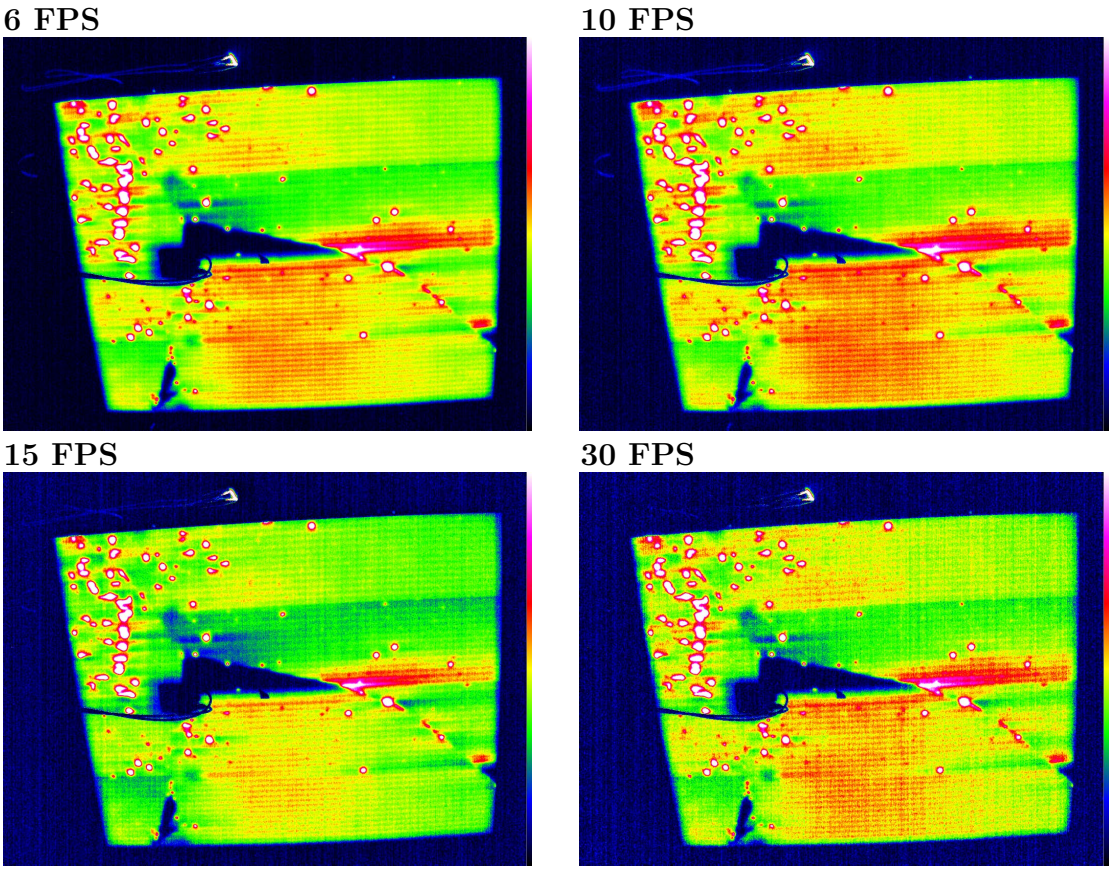

Fig. 3.29: These phase images were measured at different FPS. All images are scaled to 15% of the maximum amplitude upon the module, for higher contrast.

3.3.5 Comparison for different frames per period

The last section indicated that the images get less noisy the more frames are evaluated in agreement with (2.74). In addition it shall be investigated, if for a constant Lock-in period and 10,000 frames there is a difference in measuring with different sample rates.

The amorphous silicon (aSi) module was measured at 15 s Lock-in period at 6, 10, 15 and 30 FPS. Fig. 3.29 shows the four amplitude images, while Fig. 3.30 shows the four phase images.

There is not much difference between the four amplitude images. Only if compared very closely one might see more noise in the 30 FPS image, while the 30 FPS phase image shows clearly more noise than the others. Fig. 3.31 shows the phase image noise, where the 30 FPS image has the same noise as the 6 FPS, which does not fit to the qualitative impression of the images. 30 FPS are fair enough for a fast measurement, but for smooth images, the measurement should not be done, with more than 15 FPS.

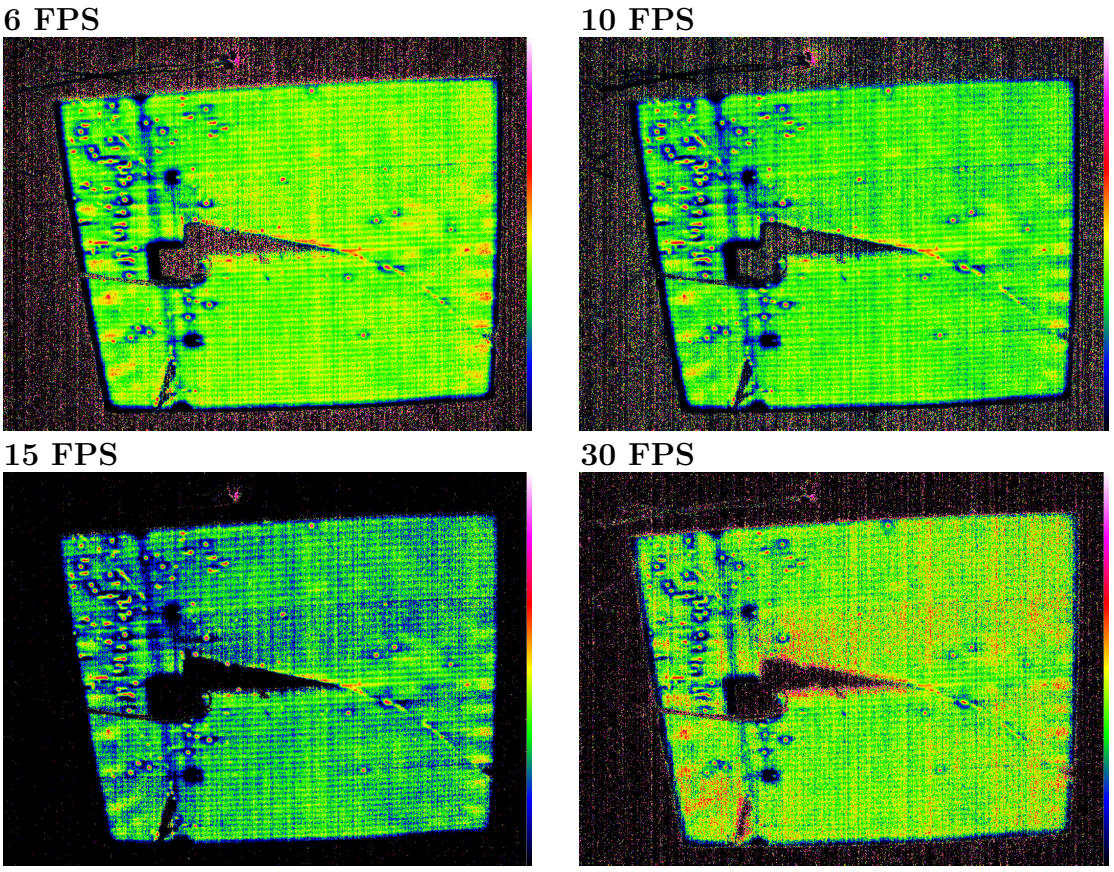

Fig. 3.30: These phase images were measured at different FPS. All images are scaled from the first phase upon the module to $\pi/4$ delay. The 30 FPS image is quite noisy.

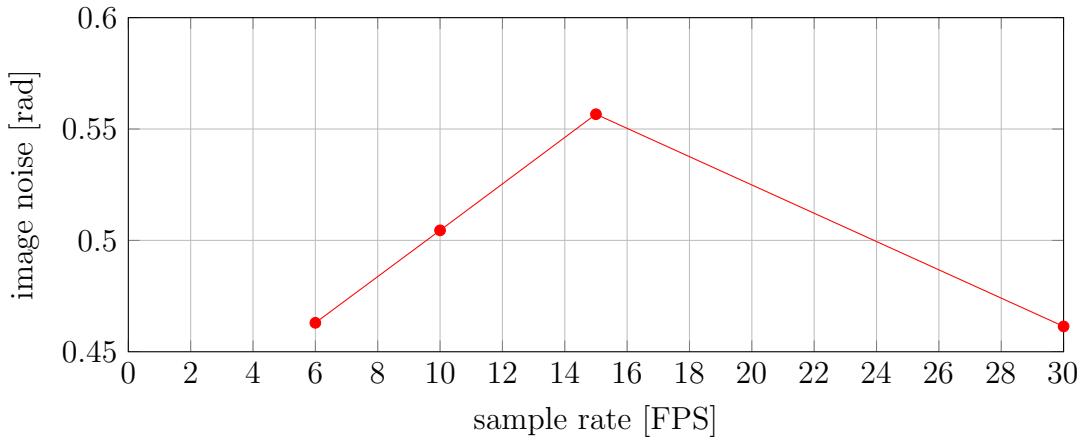

Fig. 3.31: The image noise was calculated for the phase images in Fig. 3.30 according to section 2.3.7. The chosen rectangular evaluation area extended from (550;100) to (950;380) in the upper right of the images to avoid the cracks. While the 30 FPS image seems to be most noisy, it has about the same image noise value as the 6 FPS image.

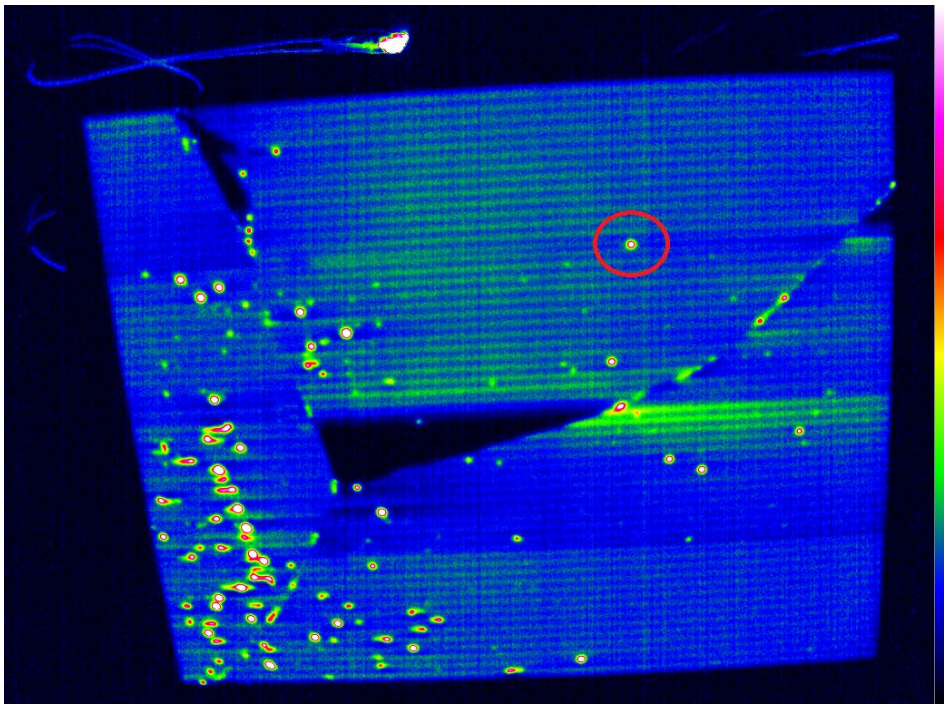

Fig. 3.32: The circle shows the point source (690;262), picked for being characterized in section 3.3.6 within an amplitude image of a 45 s Lock-in period measurement.

3.3.6 Characterization of a point source

Point sources are quite interesting in Lock-in thermography investigations of PV modules. Therefore this section will use the 45 s measurement from section 3.3.1 to depict one point source. The chosen point source in Fig. 3.32 is isolated and thus not superposed by other point sources.

This section will compare the point source in amplitude, phase, $\mathcal{C}$ (in-phase) and $\mathcal{S}$ (quadrature) images for the measured thermally thick module. First a 3D impression of a 20x20 matrix around the point source is plotted in Fig. 3.33.

The 3D graphics visualize the difference between the 4 images in terms of the chosen point source. As discussed in section 2.3.8 the quadrature image has the most broaden representation of the point source, while the in-phase signal has a lightly better resolution than the amplitude one. This can be seen better in Fig. 3.34. Further this cross section shows that the phase's maximum is one pixel apart from the other image type's maximum. The expected linear decrease in the phase image according to section 2.3.8, can be not found. A reason might be that this heat source broadens too much, resulting in a Gaussian shape. The 2D graph further shows the always positive in-phase signal, as expected for thermally thick samples, contrary to thermally thin ones. 2D and 3D graph show the pronounced halo around the point source in the quadrature image.

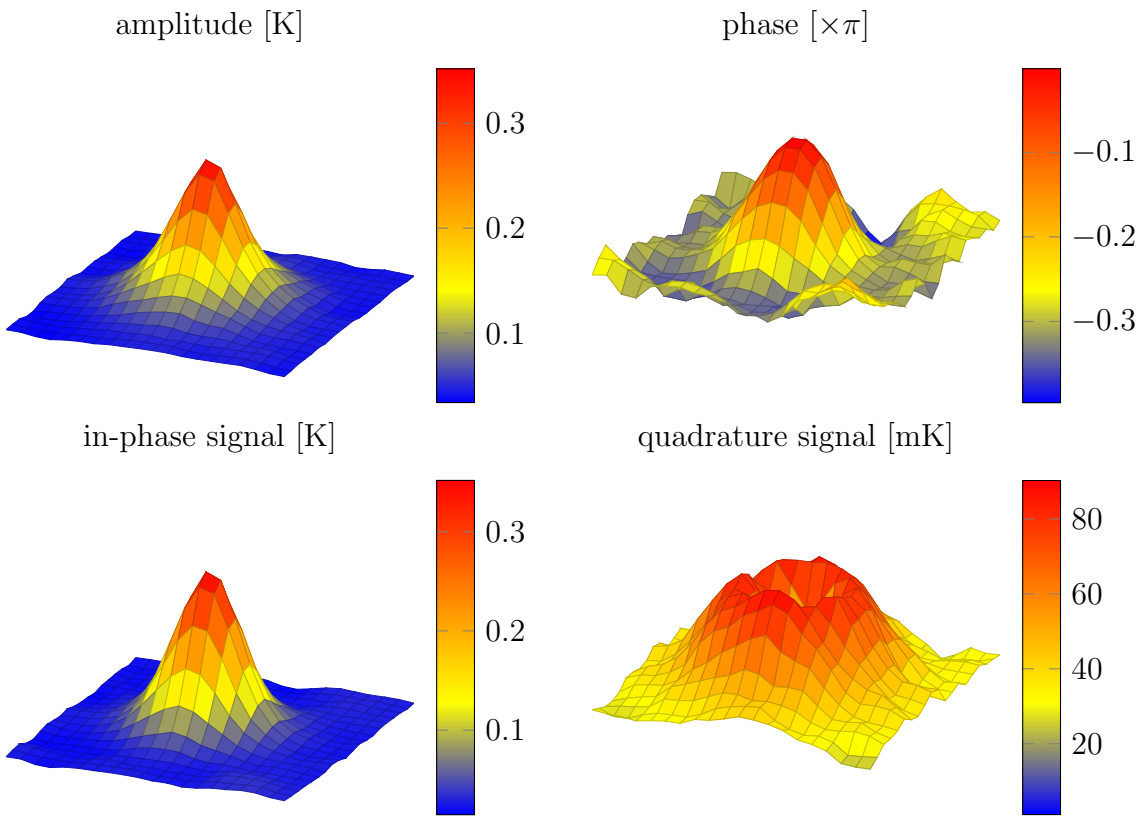

Fig. 3.33: The point source from Fig. 3.32 is plotted within an area of 20x20 pixels. As discussed in section 2.3.8, the quadratur image has the broadenst representation of the point source, while the in-phase signal has the best resolution.

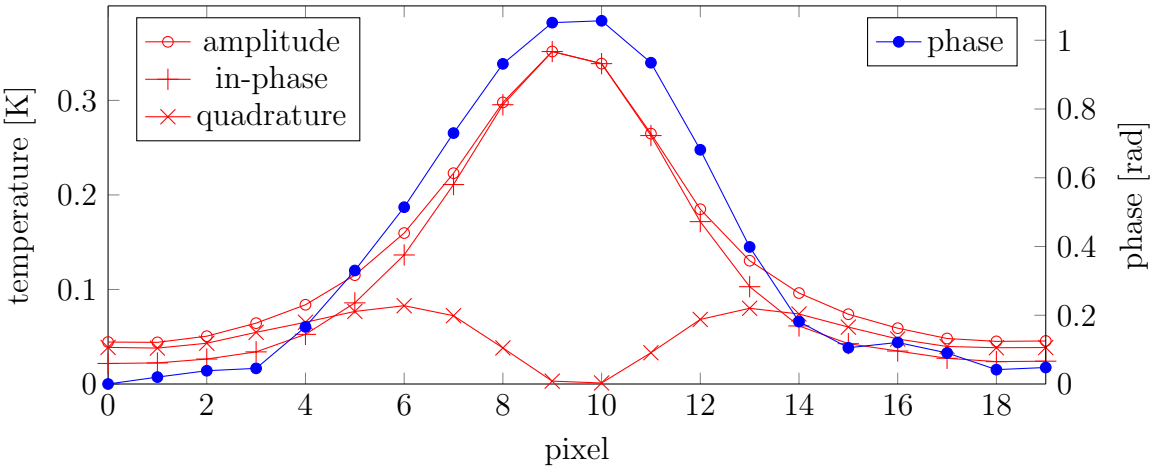

Fig. 3.34: The amplitude, in-phase ($\mathcal{C}$) and quadrature ($\mathcal{S}$) image are denoted as temperature, the phase is shifted by the value of pixel 0.

Fig. 3.35: The CdTe module is shown from the front side. Each cell has a width of about 1 cm.

3.4 Results and discussion

Measurements have been applied to six cadmium telluride (CdTe), three copper indium diselenide (CIS), one amorphous silicon (a-Si), two mono crystalline silicon (mono c-Si) and three poly crystalline silicon (poly c-Si) modules. In the following sections different characterization methods will be compared to Lock-in thermography for each module technology. The power supply's current limit in each measurement was set to the short circuit current of each module.

The compared characterization methods were measured from the front side for all measurements. If putting in direct comparison with Lock-in measurements from the back, those images were mirrored. The dark thermographies were measured after about 20 min with the same current and voltage as used for the Lock-in measurements, but without the modulation. Electroluminescence (EL) were typically measured at both low and high current. All images were rectified and lens corrected.

For PV modules, the prior described point heat sources are typically *shunts* in the cell material, called *hot spots* as well. These are localized areas of far less resistivity than their surrounding, drawing current from neighbouring areals. This can happen, at defect rich parts of the crystal lattice (e.g. grain boundaries in poly c-Si cells) or if the cell structure is damaged, leading to a connection between front and back contact. As nearby regions of the same cell carry less current they show a lower amplitude in Lock-in measurements.

3.4.1 CdTe

CdTe modules have been measured at 1 A, for which a voltage of 150 V developed. All six CdTe modules were covered with glass on both sides. Thus, the Lock-in measurements were performed from the front side.

A photograph of the module is shown in Fig. 3.35. The module has a width of about 117 cm, a height of 57 cm and consists of 117 cells in series.

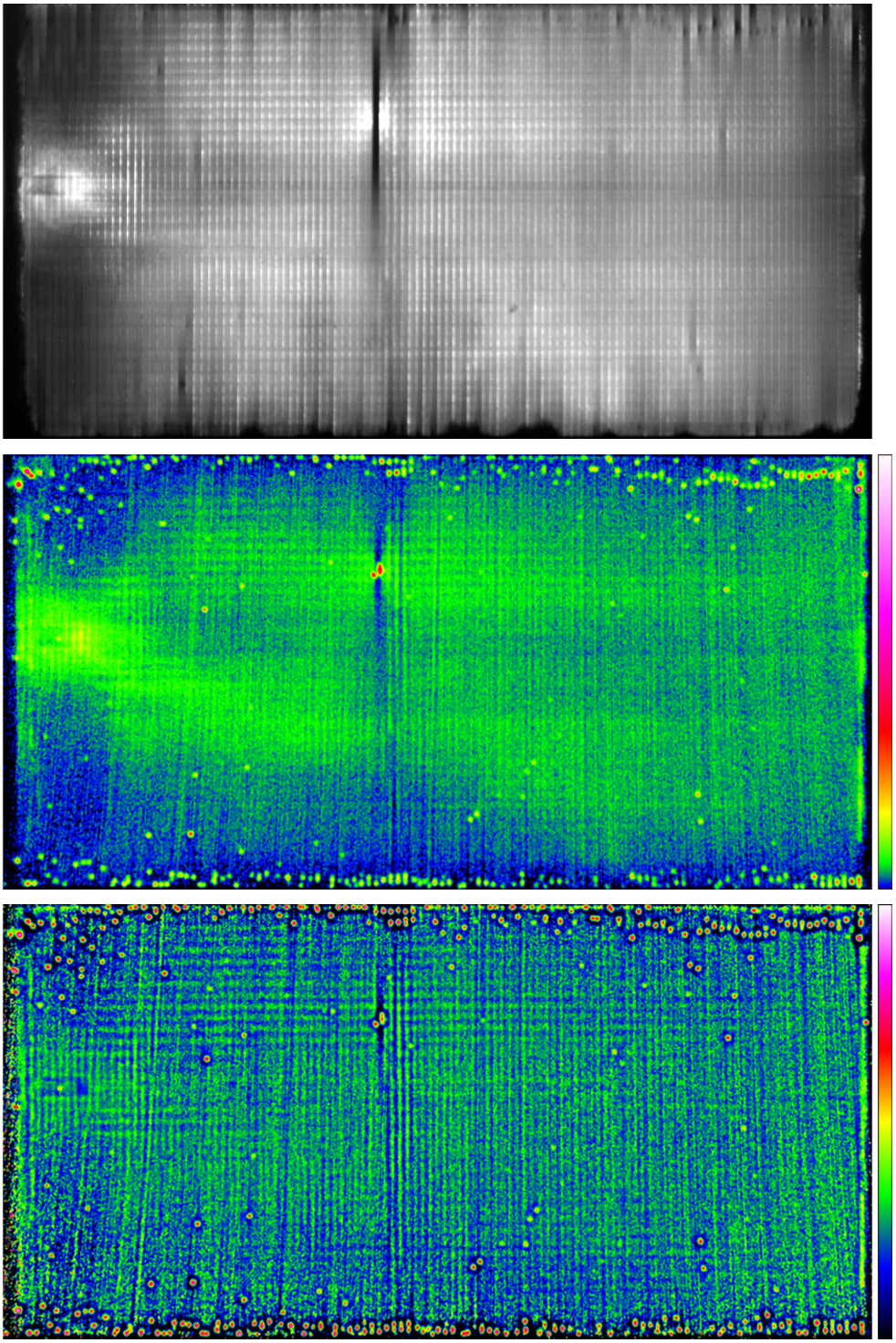

Fig. 3.36: From top to bottom: The low current EL at 0.3 A, the $\mathcal{C}$ image at 15 s period, with the maximum at 0.261 K, and a phase image at 45 s, scaled from in-phase to $\pi/4$ delay are shown for the CdTe module. The non-linear scaling of the $\mathcal{C}$ image, increases contrast.

The module was measured at 15, 45 and 150 s, each with 450 constant FPP and 10,000 frames. The 15 s $\mathcal{C}$ and the 45 s phase image are shown together with the EL in Fig. 3.36. The $\mathcal{C}$ image shows high resolution, but its phase image was too noisy, the 45 s image is smoother. The greatest hot spots are on the upper right and upper left.

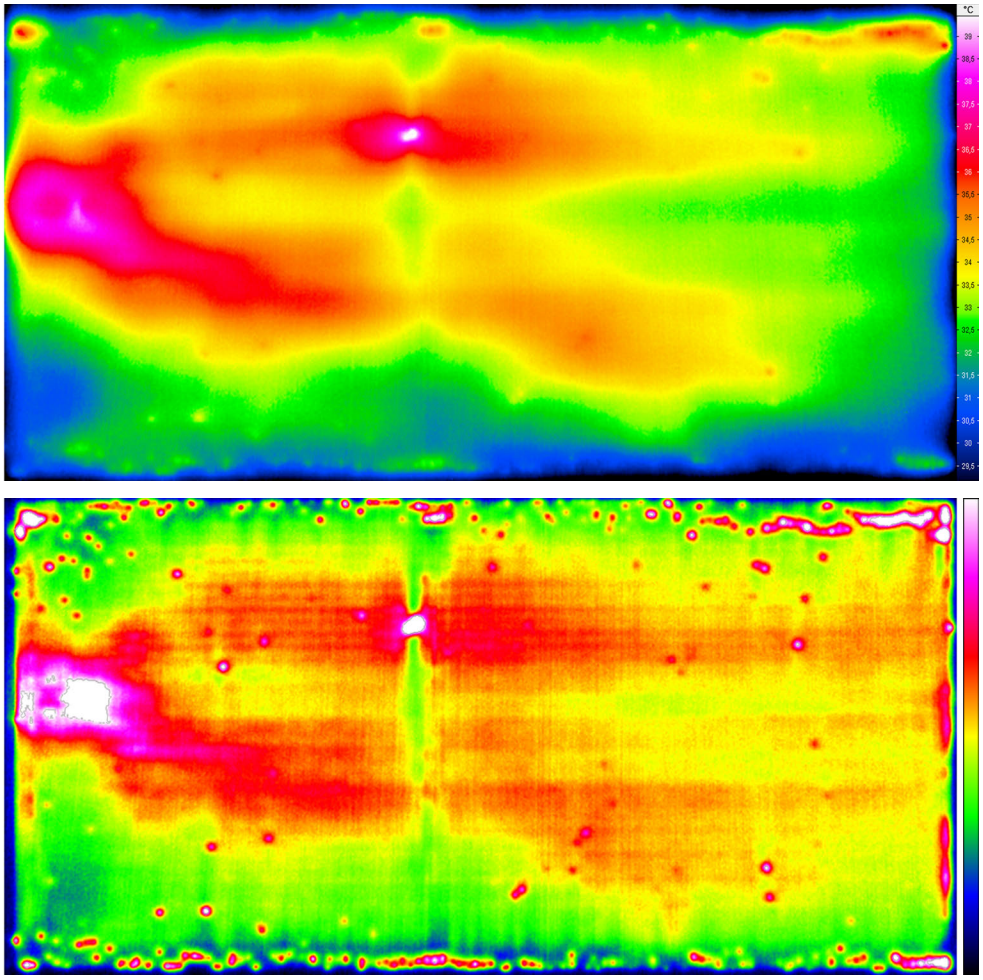

Fig. 3.37: The upper thermography of the CdTe module is scaled from 29 °C to 39.5 °C. The lower 150 s long period Lock-in amplitude image with scaling to 30% percent of the maximum module amplitude (1.388 K) illustrates the resolution of the extended heat sources.

A lot of hot spots are at the edges of the module. Thus the EL is not shaped well at the edges. This great amount of hot spots at the boundary of the module could be caused by process faults in manufacturing.

Fig. 3.37 shows the thermography and long period Lock-in amplitude image at 150 s. To increase the contrast, the Lock-in image was scaled down to 30% of its maximum.

The left shows an extended heat source (see Fig. 3.38) at the junction box on the back side, which is bright in the EL as well. Further extended heat sources are on the left and right side of the shunt in the middle (see Fig. 3.39), which obviously shortens one cell, as this cell is dark in the EL, and colder in all three presented Lock-in images. In the thermography the shunted cell is quite difficult to see. Further there is a separation between another two extended heat sources (see Fig. 3.40), below the discussed hot spot, without a visible shunt in between. Therefore here the separation may be caused by cooler cell part below the top shunt.

A lot of hot spots on the edges are not visible or outshone by other heat sources in the thermography and are better localized in the long time amplitude image, which does not even have the best resolution, compared to the phase and short time $\mathcal{C}$ image.

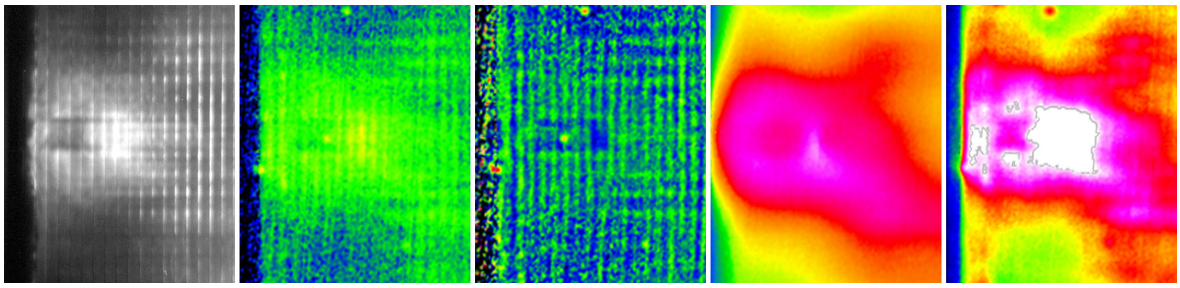

Fig. 3.38: The left extended heat source is shown from left to right in EL, $\mathcal{C}$, phase, thermography and amplitude of the CdTe module.

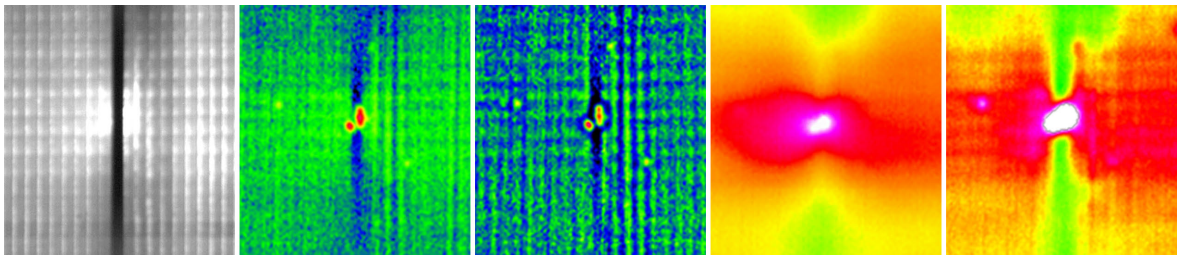

Fig. 3.39: The top middle shunt with nearby extended heat sources is shown from left to right in EL, $\mathcal{C}$, phase, thermography and amplitude of the CdTe module.

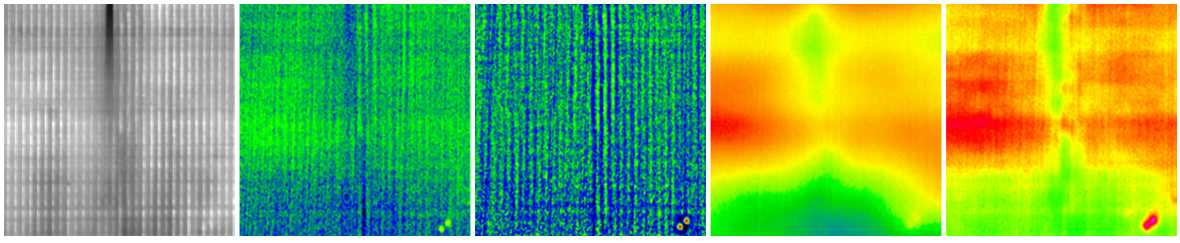

Fig. 3.40: The separation of the lower extended heat sources is shown from left to right in EL, $\mathcal{C}$, phase, thermography and amplitude of the CdTe module.

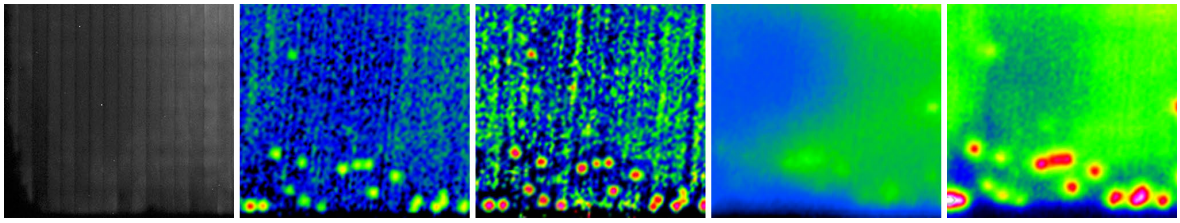

Fig. 3.41: A few weaker hot spots are shown from left to right in EL, $\mathcal{C}$, phase, thermography and amplitude of the CdTe module. There is a hot spot in the upper left, only visible in $\mathcal{C}$ and phase and amplitude image.

Fig. 3.42: The CIS module is shown from the front side. Each cell has a width of about 4 mm.

Especially some weak hot spots within the extended heat sources are not visible in the thermography (see Fig. 3.41).

3.4.2 CIS

For the CIS modules the power supply's current limit was set to 2.2 A. A voltage of 60 V developed. As the CdTe modules, all CIS modules were glass-glass modules and Lock-in measurements were only done from the front side.

A photograph of the evaluated CIS module is shown in Fig. 3.42. It consists of two separated parts with each having a width of about 27.4 cm and consisting of 67 cells. One cell has a length of 115.5 cm and extends across the longitude.

The Lock-in measurements were performed at 15, 45, 150 and 225 s, showing high noise at 15 s and too low amplitude for extended heat sources at 150 s, avoiding a good contrast. Therefore 45 s was chosen as low Lock-in period and 225 s as long Lock-in period. Both were done with 450 constant FPP and 10,000 frames. As the phase image of the 45 s measurement was still to noisy, the 150 s phase image is shown with the EL and 45 s $\mathcal{C}$ image in Fig. 3.43. The long time Lock-in image is shown together with the thermography image in Fig. 3.44.

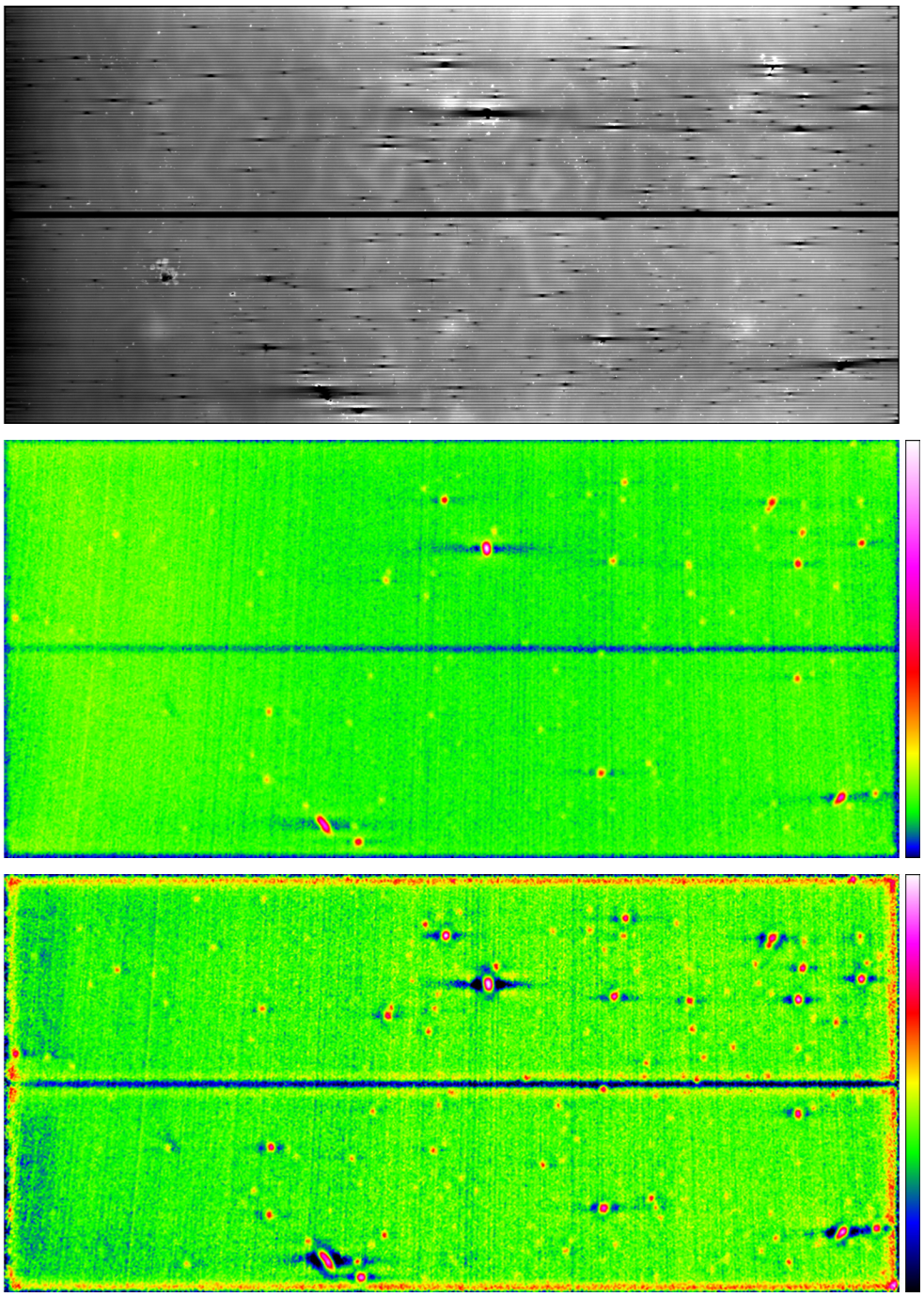

Fig. 3.43: From top to bottom: The high current EL at 2 A, the $\mathcal{C}$ image at 45 s period, with the maximum at 0.185 K, and a phase image at 150 s, scaled from in-phase to $\pi/4$ delay are shown for the CIS module. The non-linear scaling of the $\mathcal{C}$ image, increases contrast.

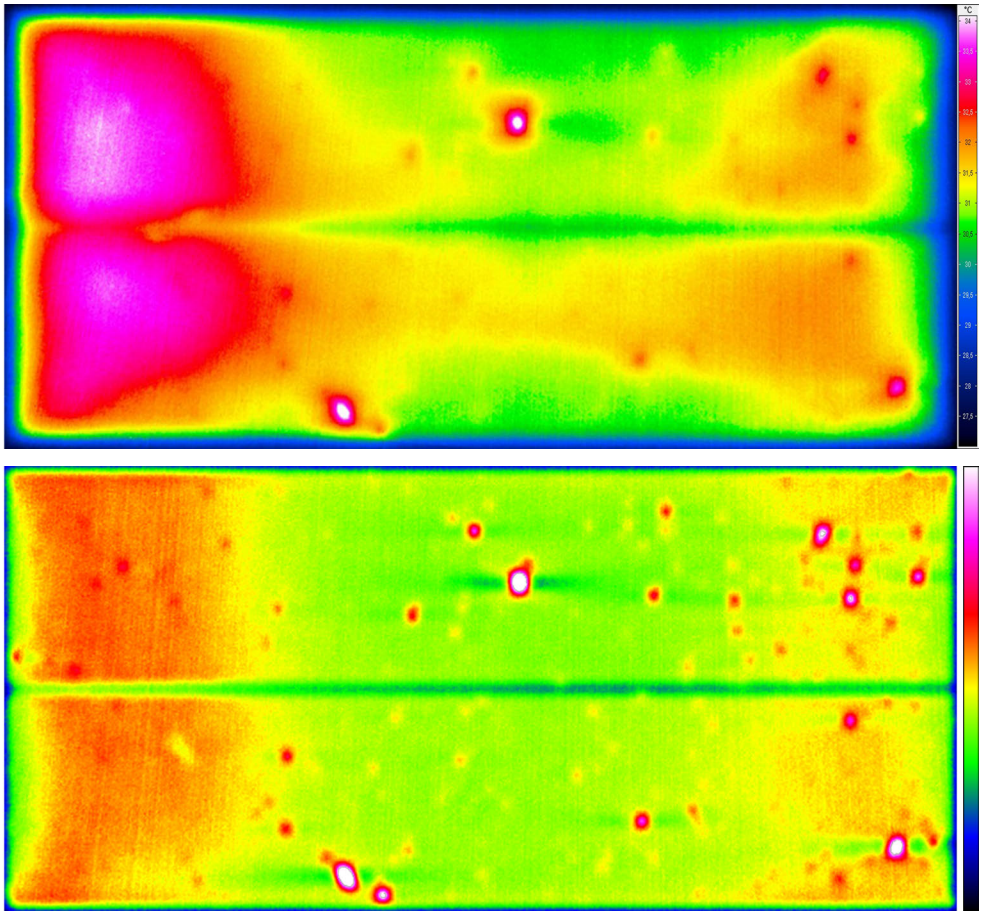

Fig. 3.44: The upper thermography of the CIS module is scaled from 27 °C to 34 °C. The lower 225 s long period Lock-in amplitude image with scaling to 50% percent of the maximum module amplitude (0.856 K) illustrates the resolution of the extended heat sources.

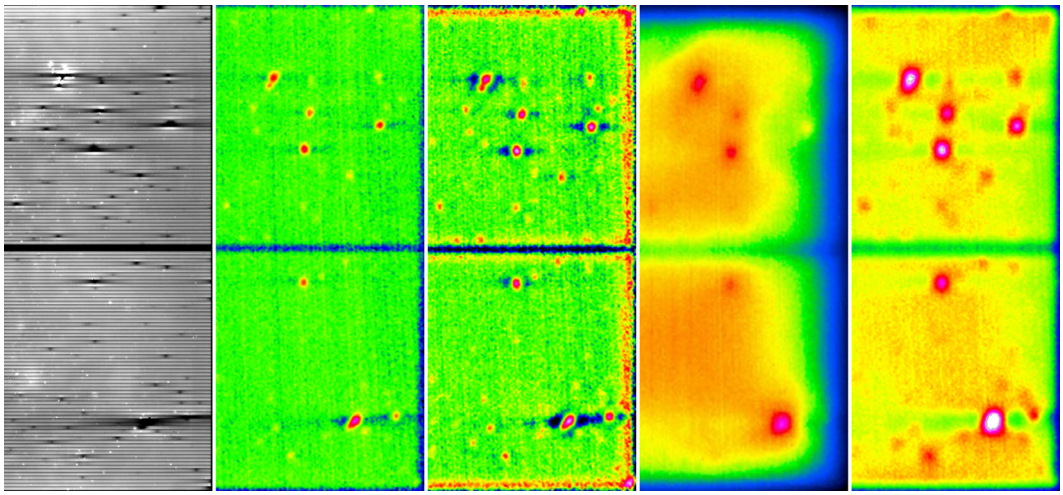

Fig. 3.45: One end of the CIS module is shown from left to right in EL, $\mathcal{C}$, phase, thermography and amplitude.

The thermography image does show some of the shunts as well and the extended heat sources blur too much. Compared to the long time Lock-in amplitude image,

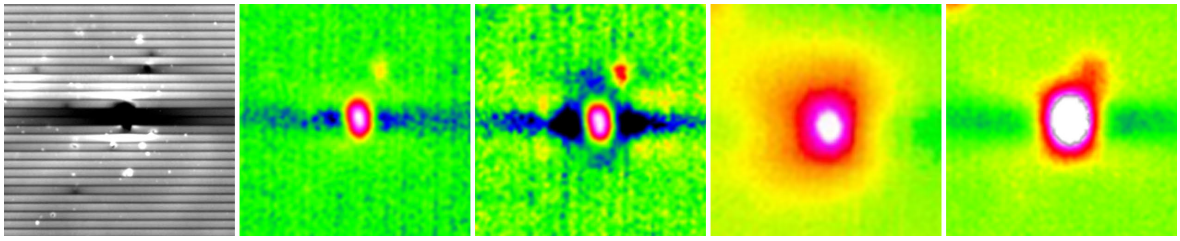

Fig. 3.46: The center main hot spot is shown from left to right in EL, $\mathcal{C}$, phase, thermography and amplitude of the CIS module.

Fig. 3.47: The a-Si module is shown from the front side and therefore mirrored vertically to match the back side measurements. Each cell has a width of 19 mm.

the resolution of the three strong hot spots is better, but the Lock-in shows better shapes of the extended heat source on the left, and it shows some further on the right (see Fig. 3.45). The right ones may come from increased current flow, as they are surrounded by shunted cells.

The in-phase image shows the best resolution of the three main hot spots (see Fig. 3.46), but it does not exhibit any smaller ones. The phase image has more blur on the big hot spots, but shows all the little ones too. Together, both Lock-in images show all the shunts, explaining the dark areas in the EL.

3.4.3 A-Si

The amorphous silicon module, already shown in some comparisons in the last section, was measured at power supply's current limit of 6.2 A with a developed voltage of 40 V. Because of the existing backsheet, measurements were done from the back.

The photograph of the module in Fig. 3.47 shows three big cracks in the glass, originating at the center. The lower left shows a lot of small cracks and a piece which is broken out. The module has nearly quadratic measures. Each cell has a length of 127 cm, with a total width of all cells of about 107 cm. The 51 cells are grouped in four blocks, each with thirteen cells. They extend from left to right on the photograph.

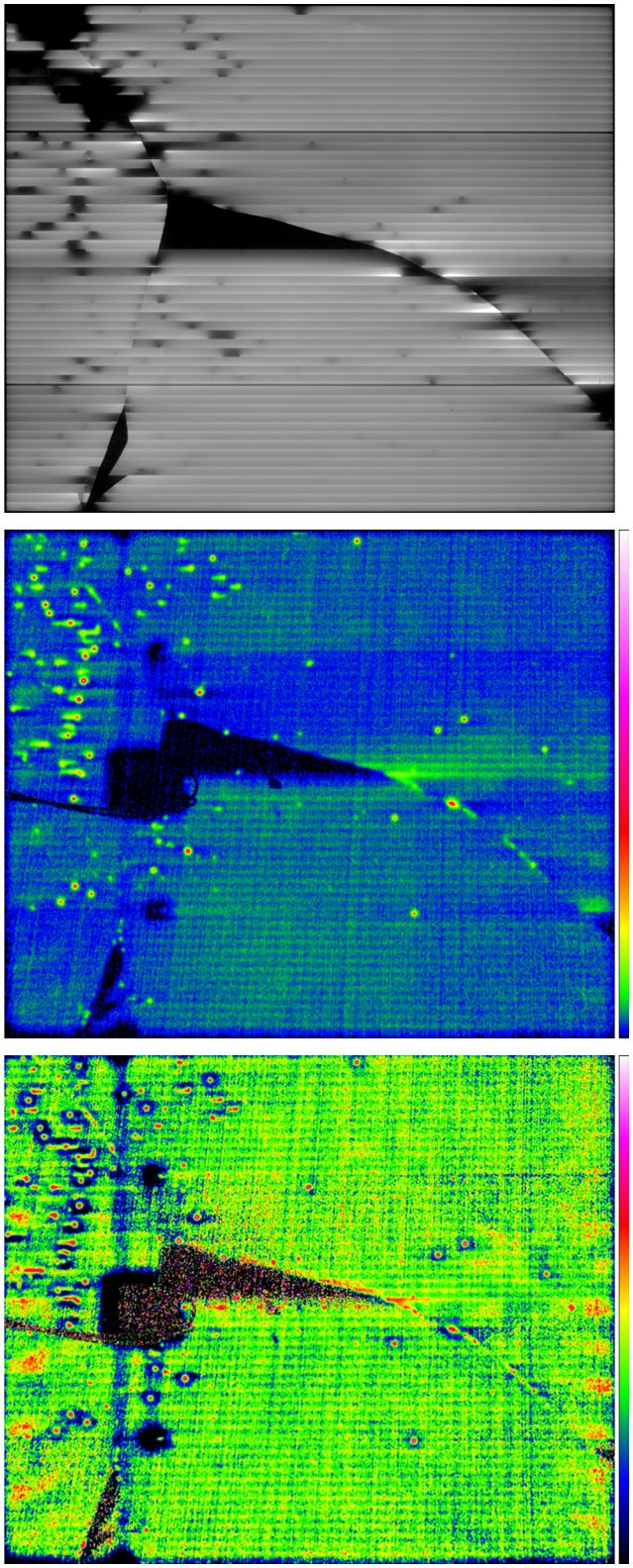

Fig. 3.48: From top to bottom: The high current EL at 6 A - mirrored vertically to be comparable, the $\mathcal{C}$ image at 5 s period, with the maximum at 0.221 K, and a phase image at 10 s period, scaled from in-phase to $\pi/4$ delay are shown for the a-Si module. The non-linear scaling of the $\mathcal{C}$ image, increases contrast.

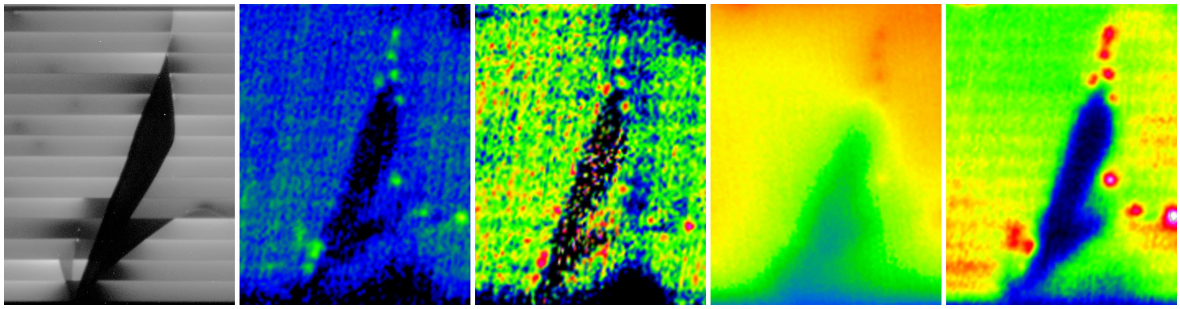

Fig. 3.49: The bottom broken out piece is shown from left to right in EL, $\mathcal{C}$, phase, thermography and amplitude of the a-Si module. At this piece is not heated, the phase image shows just noise in this area.

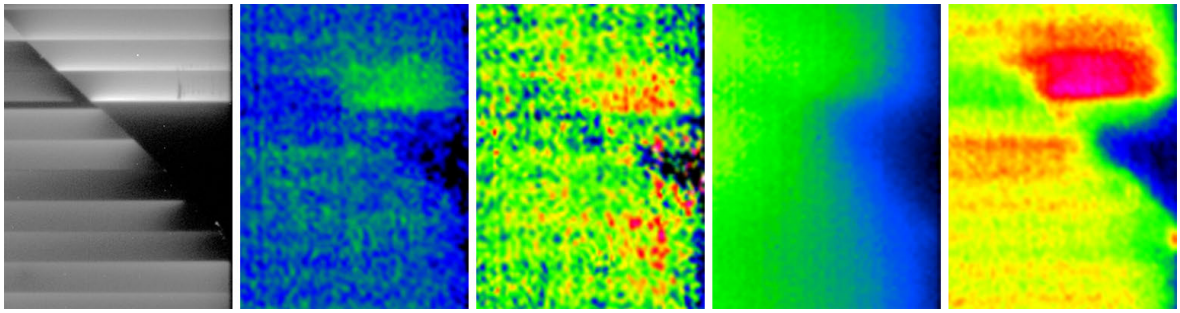

Fig. 3.50: The right triangular contact issue is shown from left to right in EL, $\mathcal{C}$, phase, thermography and amplitude of the a-Si module.

The module was measured at 5, 10, 15, 20 and 25 s, each with 150 FPP constant and 10,000 frames. The 5 s $\mathcal{C}$, 10 s phase image and the EL are shown in Fig. 3.48. Comparing these with the photograph in Fig. 3.47 shows interesting effects due to the cracks.

The broken out piece in the lower left (see Fig. 3.49) was already visible in the photograph. EL and Lock-in show, that it has really no contact to the surrounding cells. The triangular areas in the middle and the lower right (see Fig. 3.50) have both a sharp border, but no shunts. This is due to a thin block separator and a thick one in the middle. For the lower left, the last cells broke and the a part got disconnected. The first cell of the next block is then connected again, which shows a sharp border. Same goes for the triangle in the middle, consisting of parts of the first few cells, which have no connection on the top and are therefore isolated and dark.

The long time Lock-in amplitude image with 25 s and the thermography in Fig. 3.51 reveal the top and the two bottom blocks to be hotter than the second block from the top, while the Lock-in has better resolution. The Lock-in amplitude agrees with the the conclusions drawn by the EL comparison and it shows the separation into four blocks, while the EL shows the two thin separators dark and the thick separator in the middle bright.

In the EL, the top left corner contains a lot of dark regions, which might be broken out too, but being all in close vicinity. The Lock-in images and the thermography exhibit that they are shunted (see Fig. 3.52).

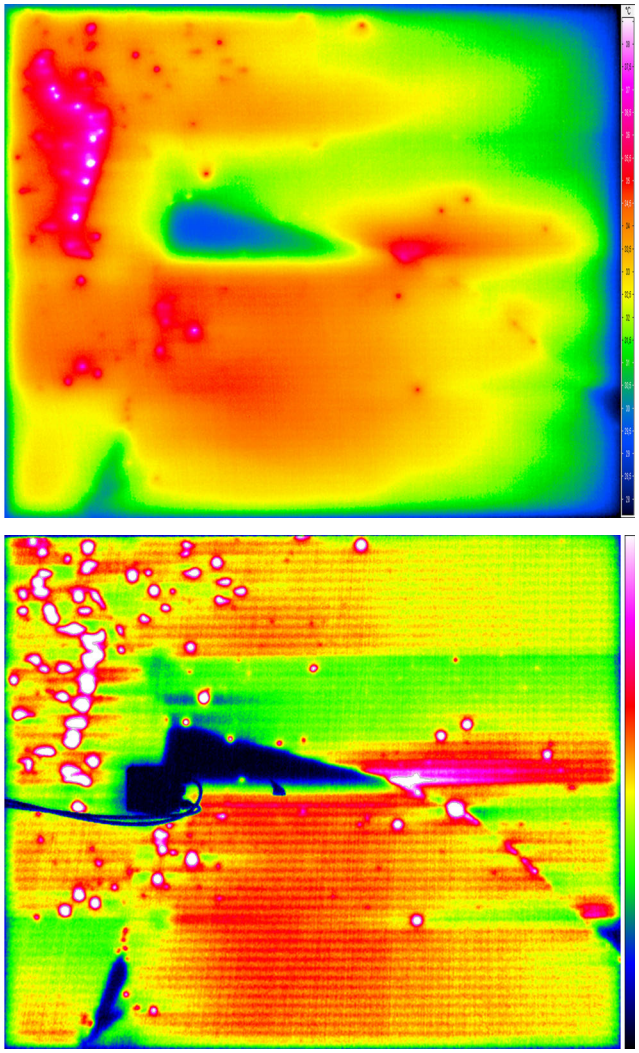

Fig. 3.51: The upper thermography of the a-Si module, scaled from 27.5 °C to 38.5 °C, is mirrored vertically to be comparable. The lower 25 s long period Lock-in amplitude image with scaling to 15% percent of the maximum module amplitude (0.741 K) illustrates the resolution of the heating of the four blocks.

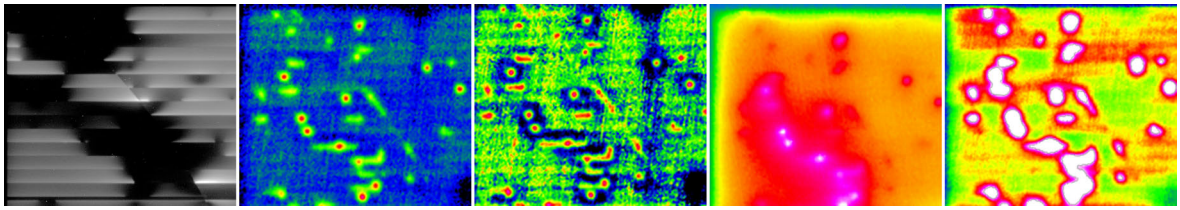

Fig. 3.52: the upper left corner of the a-Si module is shown from left to right in EL, $\mathcal{C}$, phase, thermography and amplitude.

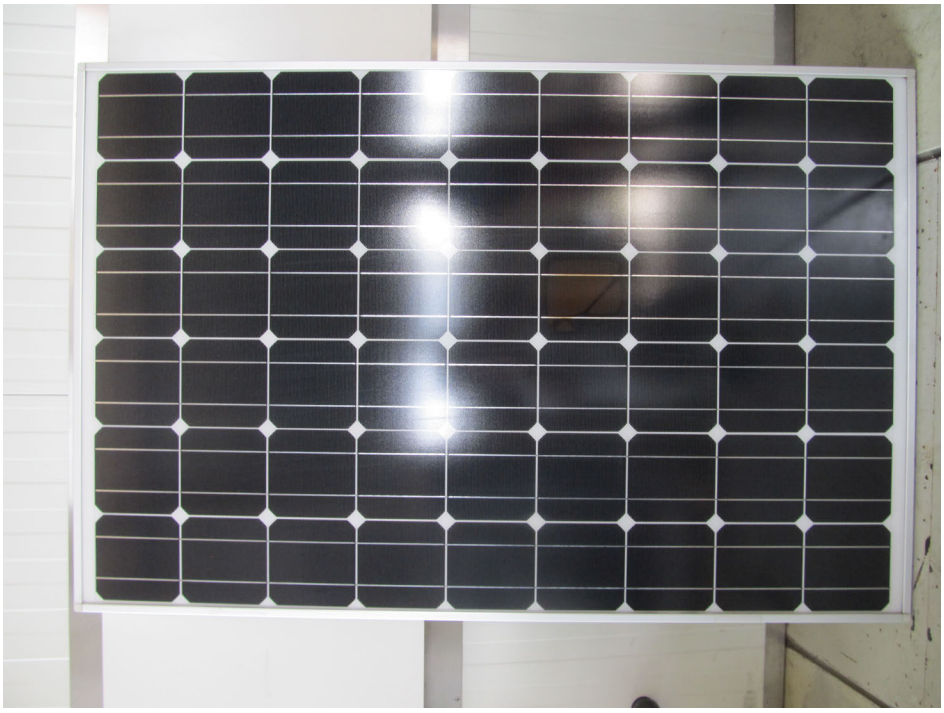

Fig. 3.53: The mono c-Si module is shown from the front side and therefore mirrored vertically to match the back side measurements. There is visible browning of a central cell.

3.4.4 Mono c-Si

The power supply's current limit was set to 8.2 A and a voltage of 60 V developed. The backsheet allowed measurement from the back side, therefore the Lock-in evaluations are carried from the back (see section 3.3.3).

Fig. 3.53 shows a photograph of the mono c-Si module. It has a length of 142 cm and a width of 95 cm and consists of 54 cells in three strings. Each cell being 15.6 × 15.6 cm in size with rounded edges due to the wafer shape. The busbars have a width of 2.5 mm.

This module was measured at 5, 10, 15 and 20 s, each with 150 constant FPP and 10,000 frames. Fig. 3.54 shows the EL, 5 s $\mathcal{C}$ and the 10 s phase image, as the 5 s phase image was again to noisy.

The EL reveals one broken cell (see Fig. 3.55) and a black spot in a center left cell (see Fig. 3.56). The separated area is dark, as the fingers are not connected anymore. In the photograph this cell looks brownish upon the remaining cell.

The $\mathcal{C}$ image shows busbars contact issues. Busbars not well contacted to the fingers, have a higher resistance and therefore appear with higher temperature. In the phase image, the busbars are also visible, as is the dot from the EL in the middle of cell third horizontal, fourth vertical from the upper left. Further, it shows areal inhomogenities, related to the ill contacted busbars shown in the $\mathcal{C}$ image.

The amplitude image is shown together with the thermography image in Fig. 3.57. The broken part is visible very well in the 20 s long period Lock-in amplitude image, as well as the dot from the EL. Further, all busbars are blurred in both images, but the ones with contact issues are more spread. Due to the longer Lock-in period

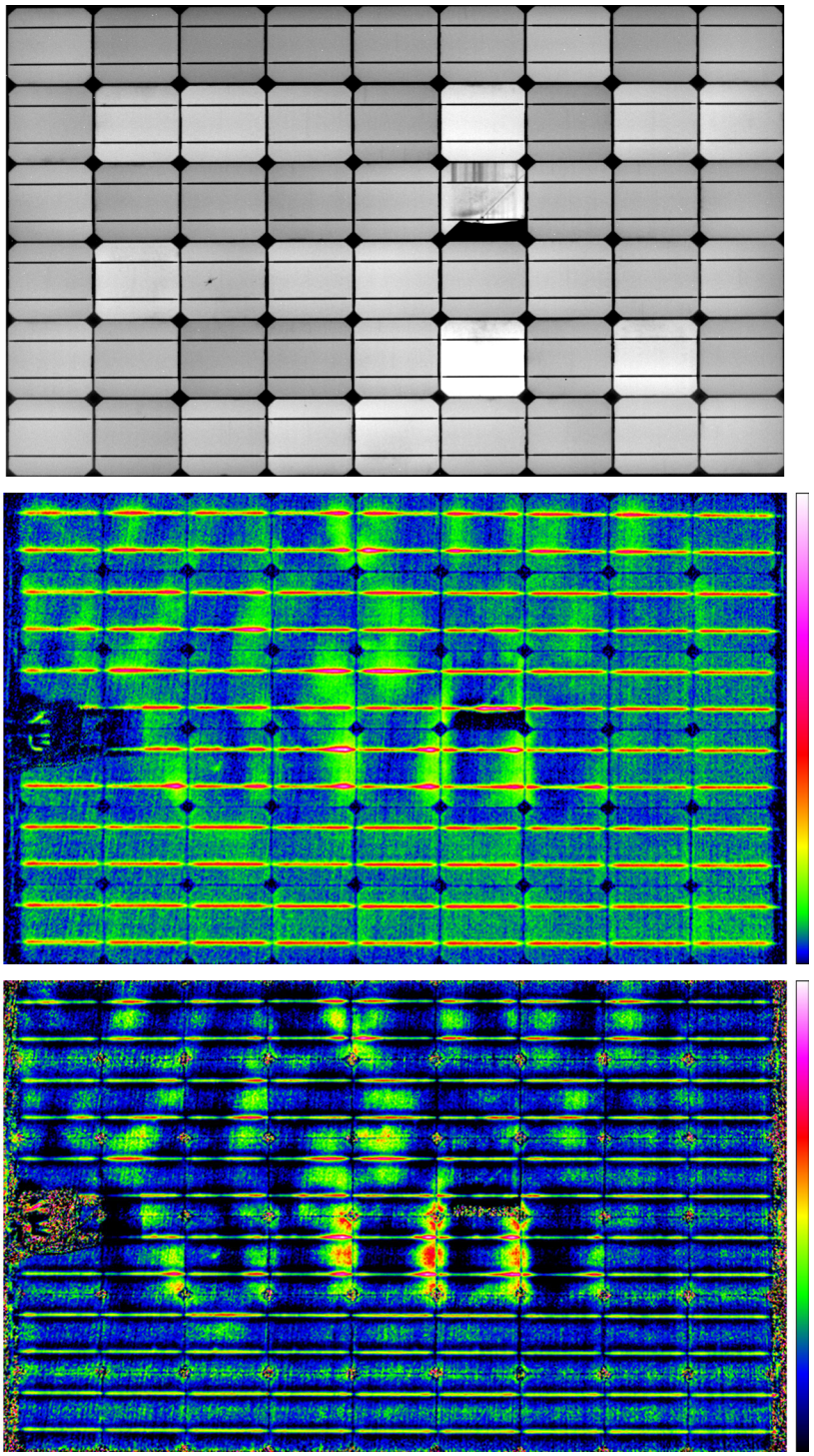

Fig. 3.54: From top to bottom: The low current EL at 0.8 A - mirrored vertically to be comparable, the $\mathcal{C}$ image at 5 s period, with the maximum at 0.094 K, and a phase image at 10 s period, scaled from in-phase to $\pi/4$ delay are shown for the mono c-Si module. The non-linear scaling of the $\mathcal{C}$ image, increases contrast.

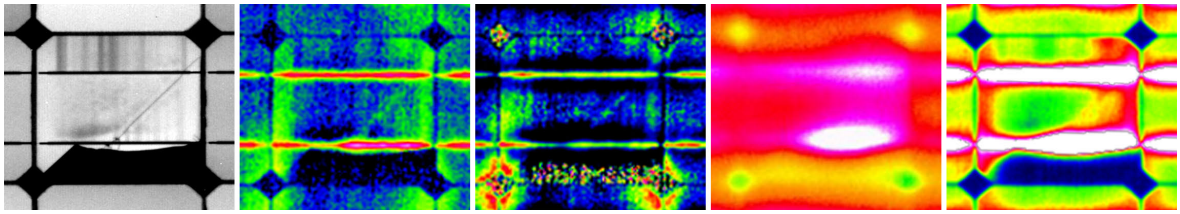

Fig. 3.55: The broken cell is shown from left to right in EL, $\mathcal{C}$, phase, thermography and amplitude of the mono c-Si module.

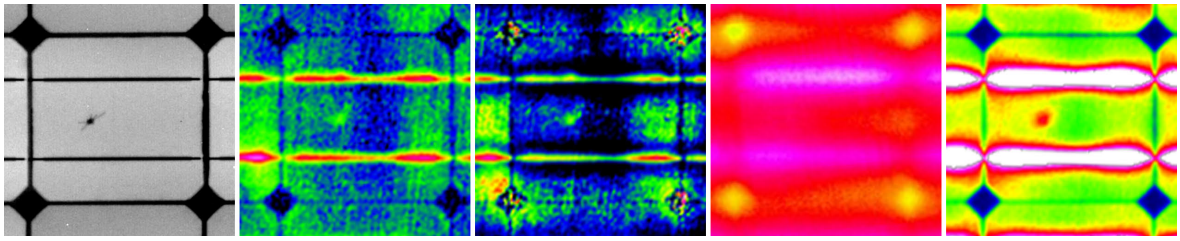

Fig. 3.56: The spot on the left of the mono c-Si module is shown from left to right in EL, $\mathcal{C}$, phase, thermography and amplitude.

length, surface heat distributions between the ill connected busbars are visible in red in Fig. 3.57 as well. This Lock-in image also show the string interconnects left and right of the module. The thermography image shows only the bright heated busbar above the crack. Also a temperature gradient can be seen, as the module was mounted with the left side up. The Lock-in images are not influenced by this constant temperature mismatch.

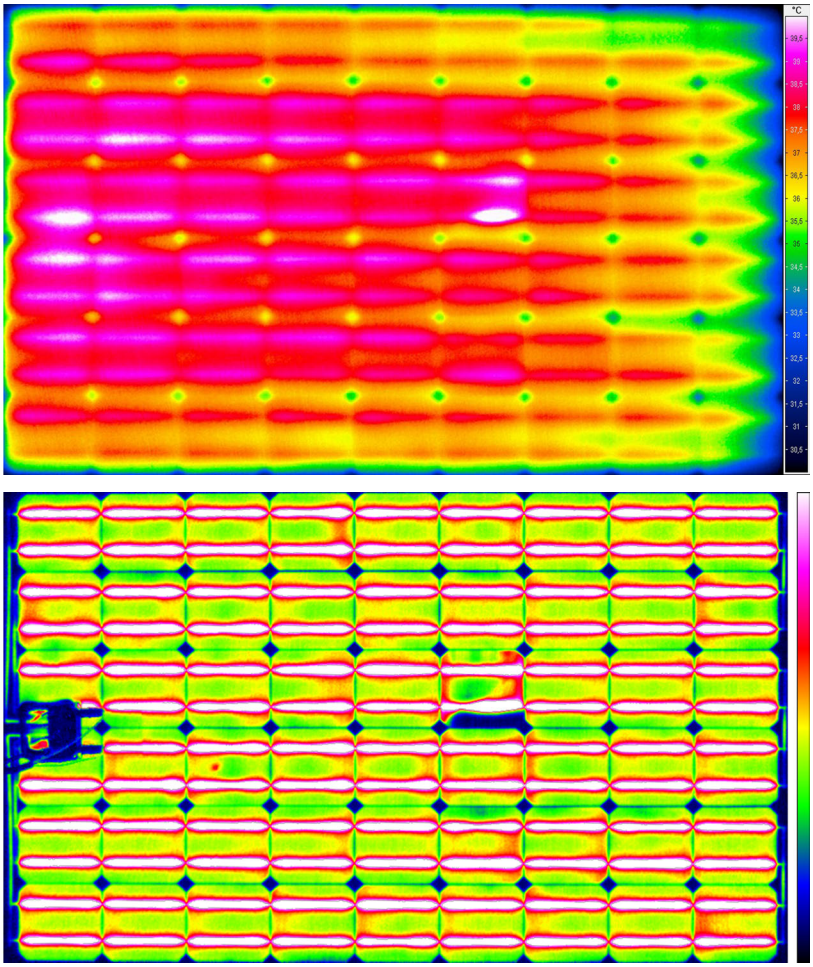

Fig. 3.57: The upper thermography of the mono c-Si module, scaled from 30 °C to 40 °C, is mirrored vertically to be comparable. The lower 20 s long period Lock-in amplitude image with scaling to 20% percent of the maximum module amplitude (0.55 K) illustrates the resolution of the extended heat sources.

Fig. 3.58: The poly c-Si module is shown from the front side and therefore mirrored vertically to match the back side measurements.

3.4.5 Poly c-Si

Power supply's limit was set to 8.2 A, for which a voltage of 60 V developed, as for mono c-Si modules. The investigated polycristalline modules were fabricated with a backsheet as well, thus Lock-in measurements are also done from the back.

As the mono c-Si module, the poly c-Si module has a size of about 142 × 95 cm with 54 quadratic cells in the size of 15.5 × 15.5 cm. This module's cells are arranged in three strings as well, see Fig. 3.58.

This module was measured at 5, 10, 15 and 20 s, each with 150 constant FPP and 10,000 frames. In Fig. 3.59 the EL, the 5 s short period $\mathcal{C}$ image and the phase image from the 10 s measurement is shown.

The cell fourth horizontal, first vertical from the bottom right has a disconnected part (see Fig. 3.60). This shows up in the EL and all Lock-in images. Looking closely at the photograph shows the remaining cell to be brownish, as for the mono c-Si module. The EL and the Lock-in image appear more inhomogenous than for the mono c-Si module. Many shapes can be found to match in the visual, EL and IR range because of the poly crystalline structure of this module.

The Lock-in images have the advantage of showing some connection faults for the busbars for all point and line sources on busbars, but there are also high temperature areas aside of the busbars. Consider the cell 4×2 from the upper left (see Fig. 3.61): Comparing these heat sources to the EL, they match the crystalline shape and seem to be defect rich places in the crystal lattice, decreasing the resistance of the lattice.

Cells second and third horizontal, first vertical from top left (see Fig. 3.62) show a point heat source on the left of the lower busbar. In contrary to the mono c-Si module

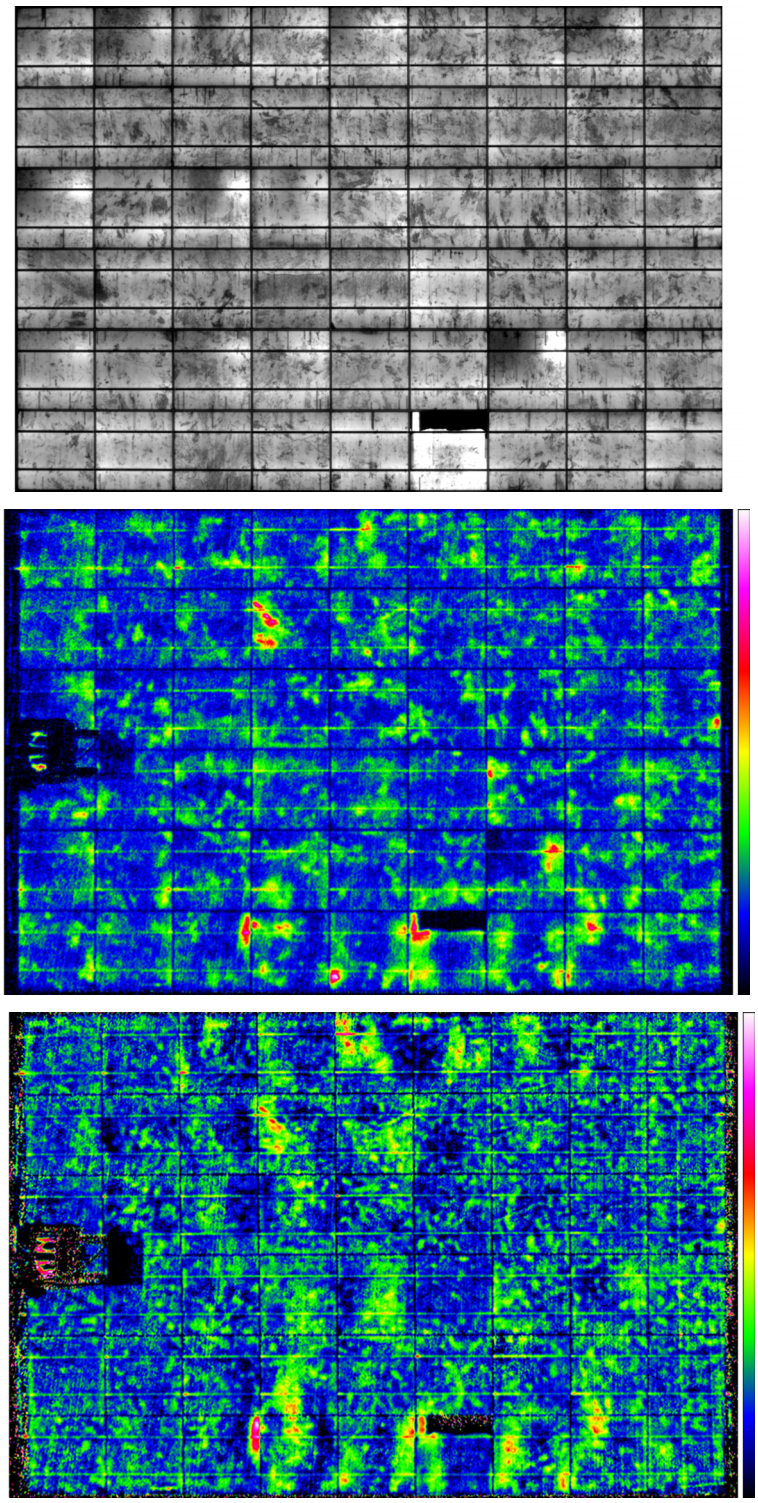

Fig. 3.59: From top to bottom: The high current EL at 8.2 A - mirrored vertically to be comparable, the $\mathcal{C}$ image at 5 s period, with the maximum at 0.054 K, and a phase image at 10 s period, scaled from in-phase to $\pi/4$ delay are shown for the poly c-Si module.

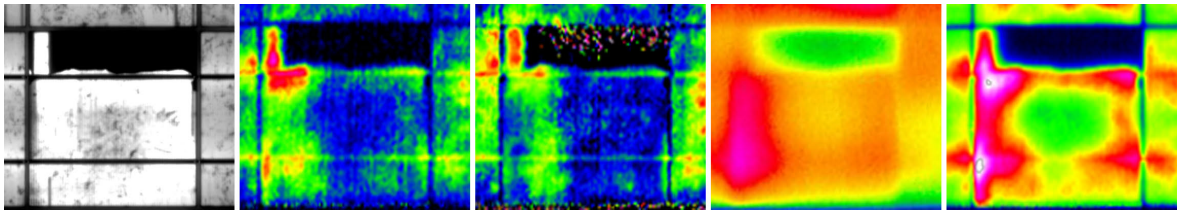

Fig. 3.60: The broken cell is shown from left to right in EL, $\mathcal{C}$, phase, thermography and amplitude of the poly c-Si module.

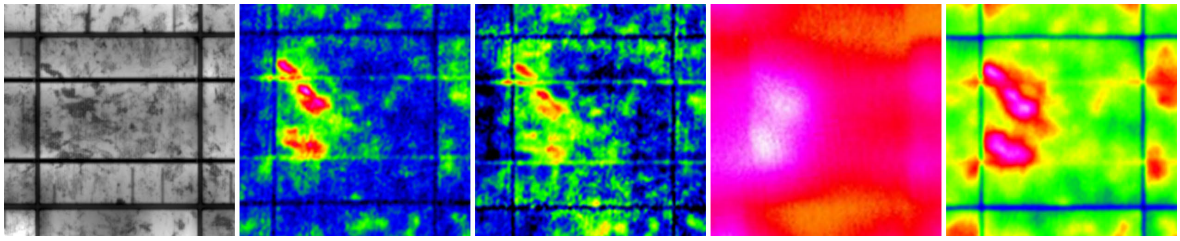

Fig. 3.61: The defect induced heat source is shown from left to right in EL, $\mathcal{C}$, phase, thermography and amplitude of the poly c-Si module.

above, busbar faults are more localized for the poly c-Si module.

Near the broken cell, there is a bright spot on the busbar in the third horizontal, second vertical cell from the bottom right (see Fig. 3.63). This area shines bright in the Lock-in and the EL image, while the left part of this busbar is dark in the Lock-in and the EL. As the EL shows high cell activity on the right part and the Lock-in shows a high temperature there, the conclusion is that the left part of the busbar has a higher contact resistance. Thus resulting in less cell activity, which is darker in the EL and produces less heat, leading to lower temperatures in the $\mathcal{C}$ Lock-in image.

The long time 20 s amplitude image and the thermography in Fig. 3.64 show the broken cell and the ill-contacted busbar as well. In this case the thermography and the amplitude image agree very well. But again the advantage of the Lock-in amplitude image is the better resolution. This can clearly be seen in the cold-hot contrast, which for the thermography are just bright hot areas. Furthermore the thermography image shows a temperature gradient from left to right, similar to the mono c-Si module.

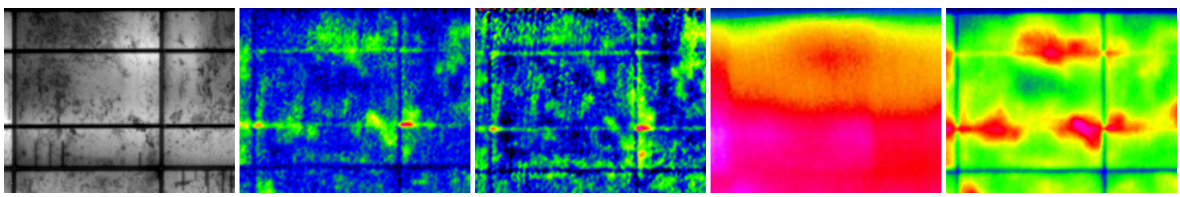

Fig. 3.62: Point sources on the busbar are shown from left to right in EL, $\mathcal{C}$, phase, thermography and amplitude of the poly c-Si module.

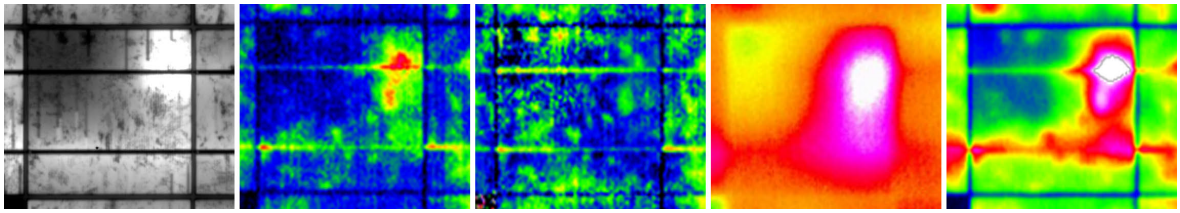

Fig. 3.63: The cell with the ill-contacted busbar is shown from left to right in EL, $\mathcal{C}$, phase, thermography and amplitude of the poly c-Si module.

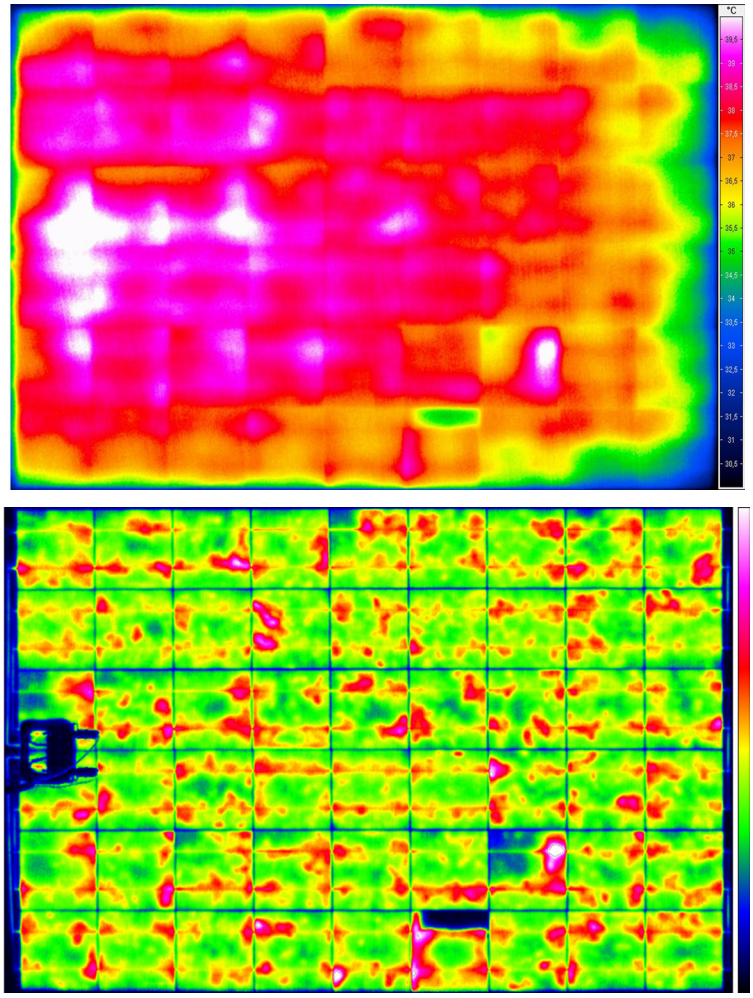

Fig. 3.64: The upper thermography of the poly c-Si module, scaled from 30 °C to 40 °C, is mirrored vertically to be comparable. The lower 20 s long period Lock-in amplitude image with scaling to 80% percent of the maximum module amplitude (0.3 K) illustrates the resolution of the extended heat sources.

3.5 Conclusions and Outlook

A DLIT measurement system was built up including setup and software for measurement analysis. The software is also capable of post processing the resulting images in scale limits and coloration, enabling better visualization.

Different module technologies have been measured and their results were compared to different investigations (EL, thermography). A good agreement was found for effects shown in all investigations. Further, DLIT complements EL measurements in detecting cracks and shunted areas and increases the spatial resolution of thermographies.

The measurements carried out showed that a back side observation can be performed at higher Lock-in frequencies than from the front side, leading to higher spatial resolution. Moreover, the measurements were compared for the amount of frames and sample rate, to possibly reduce measurement time and required storage size. It was found that a maximum sample rate of 15 FPS should only be exceeded for fast investigations, because of high image noise. Comparisons showed that a sample of 4,000 frames is enough, saving 60% of data, compared to the 10,000 frames which were taken for most of the measurements. Thus, a measurement can be performed in about 5 min per Lock-in frequency, after the obligatory heating up of the module.

The heatup phase takes up to 45 min, which is 450% of the time needed to measure one module at two different frequencies. Further improvements of the introduced DLIT setup may consider measuring the heatup phase, by correcting the increase in temperature by the software after the measurement. Another solution may be constant heating for a certain time and starting the measurement after a few periods of introduced modulation. Sufficient duration for this procedure may be shorter than 45 min.

Due to missing synchronization of heating and frame rate, additional noise may be introduced. Further effort on a trigger signal may reduce image noise, and could allow more sensitive measurements. Also, the current algorithm of image noise determination does not correspond to the human impression of noise in an image, as shown in some results. Any automation in the software, needs a better working algorithm in agreement with the image.

At the moment a lot of time is lost in analysing images by hand. Further automation of the software tool, e.g. for phase correction and saving results as well as batch processing multiple measurements at once, will improve the workflow. However it needs to be considered that the human eye may recognize various effects, which might be missed using automation.

Bibliography

[1] Armin G. Aberle. Thin-film solar cells. *Thin Solid Films*, 517:4706–4710, 2009.

[2] Daniel Abou-Ras, Thomas Kirchartz, and Uwe Rau. *Advanced Characterization Techniques for Thin Film Solar Cells*. WILEY-VCH Verlag GmbH & Co. KGaA, 1st edition, 2011.

[3] IEA International Energy Agency. 2014 key world energy statistics. Technical report, OECD/IEA, 2014.

[4] Arduino. Home. `http://www.arduino.cc/`, 2014. [Online; accessed 23-November-2014].

[5] Photovoltaic Austria. PV infos - Daten & Fakten - Grafiken. `http://www.pvaustria.at/daten-fakten/grafiken/`, 2014. [Online; accessed 16-November-2014].

[6] Peter Biermayr, Manuela Eberl, Monika Enigl, Huber Fechner, Christa Kristöfel, Kurt Leonhartsberger, Florian Maringer, Stefan Moidl, Christoph Strasser, Werner Weiss, and Manfred Wörgetter. Innovative Energietechnologien in österreich Marktentwicklung 2013. Technical report, bmvit - Bundesministerium für Verkehr, Innovation und Technologie, 2014.

[7] Otwin Breitenstein, Wilhelm Warta, and Martin Langenkamp. *Lock-in Thermography - Basics and Use for Evaluating Electronic Devices and Materials*. Springer-Verlag Berlin Heidelberg, 2nd edition, 2010.

[8] Ilja N. Bronshtein, Konstantin A. Semendyayev, Gerhard Musiol, and Heiner Muehlig. *Handbook of Mathematics*. Springer-Verlag Berlin Heidelberg, 5th edition, 2007.

[9] Wolfram Alpha LLC—A Wolfram Research Company. `http://www.wolframalpha.com/`, 2014. [Online; accessed 22-November-2014].

[10] Wolfgang Demtröder. *Experimentalphysik 1 - Mechanik und Wärme*. Springer-Verlag Berlin Heidelberg, 5th edition, 2008.

[11] Wolfgang Demtröder. *Experimentalphysik 3 - Atome, Moleküle und Festkörper*. Springer-Verlag Berlin Heidelberg, 4th edition, 2010.

[12] PV education. Solar cell operation - ideality factor. `http://pveducation.org/pvcdrom/solar-cell-operation/ideality-factor`, 2014. [Online; accessed 13-November-2014].

[13] Enerdata. Global energy statistical yearbook 2014. `https://yearbook.enerdata.net/`, 2014. [Online; accessed 16-November-2014].

[14] IHS Engineering. Cid cameras information. `http://www.globalspec.com/learnmore/imaging_video_equipment/video_cameras_accessories/cid_cameras`, 2014. [Online; accessed 20-November-2014].

[15] Gerald B. Folland. *Fourier analysis and its applications*. Brooks/Cole Publishing Company, 1992.

[16] NREL National Center for Photovoltaics. `http://www.nrel.gov/ncpv/`, 2014. [Online; accessed 9-November-2014].

[17] F Forsberg, A C Fischer, N Roxhed, B Samel, P Ericsson, G Stemme, and F Niklaus. Heterogeneous 3d integration of 17 μm pitch si/sige quantum well bolometer arrays for infrared imaging systems. *Journal of Micromechanics and Microengineering*, 23(4):045017, 2013.

[18] Russell M. Geisthardt and James R. Sites. Light-beam-induced-current characterization of cdte solar cells. *IEEE 40th Photovoltaic Specialist Conference (PVSC)*, pages 1848–1851, 2014.

[19] Russell M. Geisthardt and James R. Sites. Nonuniformity characterization of cdte solar cells using lbic. *IEEE Journal of Photovoltaics*, 4:1114–1118, 2014.

[20] Justus-Liebig-Universität Giessen. Photolumineszenz. `http://www.uni-giessen.de/cms/fbz/fb07/fachgebiete/physik/einrichtungen/ipi/ag/ag1/analytik/pl`, 2011. [Online; accessed 19-November-2014].

[21] Adolf Goetzberger and Volker U. Hoffmann. *Photovoltaic Solar Energy Generation*. Springer-Verlag Berlin Heidelberg, 1st edition, 2005.

[22] Adolf Goetzberger, Joachim Knobloch, and Bernhard Voss. *Crystalline Silicon Solar Cells*. John Wiley & Sons Ltd., 1st edition, 1998.

[23] Yoshihiro Hamakawa. *Thin-Film Solar Cells - Next Generation Photovoltaics and Its Applications*. Springer-Verlag Berlin Heidelberg, 1st edition, 2004.

[24] J.F. Hiltner and J.R. Sites. High resolution laser stepping measurements on polycrystalline solar cells. *Proc. 16th Eur. Photovoltaic Sol. Energy Conf.*, pages 650–653, 2000.

[25] Qt Project Hosting. Qt project. `http://qt-project.org/`, 2014. [Online; accessed 26-November-2014].

[26] Infrared-thermography. Emissivity values of common materials. `http://www.infrared-thermography.com/material-1.htm`, 2008. [Online; accessed 20-November-2014].

[27] Infrared-thermography. Emissivity values of common materials. `http://www.thermografie-xtra.de/tipps-tricks/emissionsgrad-tabelle.html`, 2014. [Online; accessed 20-November-2014].

[28] InfraTec GmbH. *VarioCAM HD User Manual*.

[29] Martin Kaltschmitt, Wolfgang Streicher, and Andreas Wiese. *Erneuerbare Energien - Systemtechnik, Wirtschaftlichkeit, Umweltaspekte*. Springer-Verlag Berlin Heidelberg, 4th edition, 2006.

[30] M. Kimata, M. Ueno, H. Yagi, T. Shiraishi, M. Kawai, K. Endo, Y. Kosasayama, T. Sone, T. Ozeki, and N. Tsubouchi. PtSi Schottky-barrier infrared focal plane arrays. *Opto-electronics review*, 6(1):1–10, 1998.

[31] A. Lawerenz, K. Lauer, M. Blech, A. Laades, and M. Zentgraf. Photoluminescence lifetime imaging using led arrays as excitation source. *25th, European photovoltaic solar energy conference*, pages 2486–2489, 2010.

[32] M. D. Lechner, W. Heiland, P. Hertel, S. Jovanovic, J.V. Kratz, B. Markert, E. Nordmeier, H. Rosemeyer, D. Steinmeier, O. Thiemann, and M. Wöhlecke. *Taschenbuch für Chemiker und Physiker - Band I - Physikalisch-chemische Daten*. Springer-Verlag Berlin Heidelberg, 4th edition, 1992.

[33] B.F. Levine. Quantum-well infrared photodetectors. *J. Appl. Phys.*, 74(8):R1–R81, 1993.

[34] Antonio Luque and Steven Hegedus. *Handbook of Photovoltaic Science and Engineering*. John Wiley & Sons, Ltd, 2nd edition, 2011.

[35] John Lester Miller. *Principles of Infrared Technology - A Practical Guide to the State of the Art*. Van Nostrand Reinhold, 1st edition, 1994.

[36] Waldemar Minkina and Sebastian Dudzik. *Infrared Thermography - Errors and Uncertainties*. John Wiley & Sons, Ltd, 1st edition, 2009.

[37] D.W. Palmer. The semiconductors-information - properties of the ii-vi compound semiconductors. `http://www.semiconductors.co.uk/propiivi5410.htm`, 2008. [Online; accessed 21-November-2014].

[38] PJRC. Teensy usb development board. `https://www.pjrc.com/teensy/`, 2014. [Online; accessed 23-November-2014].

[39] Jef Poortmans and Vladimir Arkhipov. *Thin Film Solar Cells - Fabrication, Characterization and Applications*. John Wiley & Sons Ltd., 1st edition, 2006.

[40] Volker Quaschning. *Regenerative Energiesysteme*. Hanser Verlag München, 7th edition, 2011.

[41] P.L. Richards. Bolometers for infrared and millimeter waves. *J. Appl. Phys.*, 76(1):1–24, 1994.

[42] Norbert Schuster and Valentin G. Kolobrodov. *Infrarotthermographie*. WILEY-VCH Verlag GmbH & Co. KGaA, Weinheim, 2nd edition, 2004.

[43] American Physical Society. Energy units. `http://www.aps.org/policy/reports/popa-reports/energy/units.cfm`, 2014. [Online; accessed 18-November-2014].

[44] S P T. The bolometer. *Nature*, 25(627):14–16, 1881.

[45] Frank Thuselt. *Physik der Halbleiterbauelemente - Einführendes Lehrbuch für Ingenieure und Physiker*. Springer-Verlag Berlin Heidelberg, 2nd edition, 2011.

[46] V.V. Tyagi, Nuru A. A. Rahim, N.A. Rahim, and Jeyraj A./L. Selvaraj. Progress in solar PV technology: Research and achievement. *Renewable and Sustainable Energy Reviews*, 20:443–461, 2013.

[47] Peter Würfel. *Physics of Solar Cells - From Basic Principles to Advanced Concepts*. WILEY-VCH Verlag GmbH & Co. KGaA, Weinheim, 2nd edition, 2009.

List of Figures

List of Tables